Relationships between climate and geophysical processes: what climate histories can be inferred from glaciers, lakes, and ice streams?

Kathleen Huybers

A dissertation
submitted in partial fulfillment of the
requirements for the degree of

Doctor of Philosophy

University of Washington

2014

Reading Committee:

Gerard Roe, Chair

Howard Conway

Summer Rupper

Program Authorized to Offer Degree:
University of Washington
Department of Earth and Space Sciences

University of Washington

Abstract

Relationships between climate and geophysical processes:
what climate histories can be inferred from glaciers, lakes, and ice streams?

Kathleen Huybers

Chair of the Supervisory Committee:
Professor Gerard Roe
Earth and Space Sciences

This dissertation aims to characterize the present and future variability of the Earth's climate by putting it in the context of past variations in climate. Herein I explore how the spatial and temporal fluctuations of climate variables such as temperature, precipitation, evaporation, and sea level are filtered and integrated by the geophysical systems that they influence. I use relatively simple models to explore the scale over which a paleoclimate proxy record is relevant, the physics and parameters to which the system is most sensitive, and how one can distinguish a climate signal from noise.

The three geophysical systems explored in this work are detailed below:

1. **Glaciers:** Glaciers integrate interannual variations in precipitation and temperature and respond with kilometer-scale, multi-decadal terminus fluctuations [Oerlemans, 2000, Reichert et al., 2002, Roe and O'Neal, 2009]. My work extends these studies, and uses reanalysis data and correlation analysis to establish how patterns in precipitation, temperature, and glacier geometry give rise to patterns in glacier advance and retreat. Using a linearized glacier model, I also derive analytic expressions to calculate the expected coherence of regional

glacier advance and retreat, and to assess the sensitivity of these glaciers to temperature and precipitation changes. By focusing on how climatic and geometric heterogeneity affect patterns of regional glacier length variations, I isolate the parameters that exert the most influence on the timing and magnitude of glacier response to temporal variations in the climate.

2. **Lakes:** Like mountain glaciers, lakes integrate year-to-year climate fluctuations to produce large, persistent surface fluctuations on timescales of decades or longer. Using the Great Salt Lake as a case study, I model lake-level variability in response to perturbations in evaporation and precipitation. Though there already exists a body of work that has characterized persistence in observed lake-level variations [Mason et al., 1994, Lall and Mann, 1995, Abarbanel and Lall, 1996, Mohammed and Tarboton, 2011], my research shows that this persistence not only reflects any autocorrelation in the climate, but is also intrinsic to the dynamics of the lake system. My work also shows how the geometry of the lake influences the magnitude and persistence of lake level fluctuations. These results develop a null hypothesis in expected lake-level variability which can be compared to the magnitude and frequency of paleo lake-level variations.

3. **Ice streams:** Previous studies have used flowline models to understand the behavior of ice streams on idealized bed geometries [Schoof, 2007, Docquier et al., 2011]. This work applies the flowline model approach to a realistic basal topography beneath the West Antarctic Ice Sheet (WAIS), and evaluates changes in grounding line positions and upstream ice profiles in response to changes in model physics and environmental factors.

These sensitivity studies demonstrate that the present positions of many Wed-

dell Sea-sector grounding lines lie within an asymmetric trench, implying a strong stability to retreat, but also creating the potential for significant advance due to either sea-level lowering on the order of tens of meters, or conceivably, from precipitation increases of less than 10%. My evaluation reaffirms that the greatest concerns for WAIS retreat or collapse are locations of reverse slopes, muted basal topography, and limited lateral support.

This dissertation uses models of low complexity, allowing for a complete understanding of the system, and providing a deeper and richer understanding of the temporal and spatial patterns of Earth's limitless complexity.

TABLE OF CONTENTS

LIST OF FIGURES

LIST OF TABLES

ACKNOWLEDGMENTS

This work would not have been possible without the many people who have supported me during my studies and research.

Gerard Roe has been an incredible mentor. He is my greatest ally, and has pushed me further than I thought possible. I am forever grateful for his insights, patience, encouragement, friendship, and brilliance. I also deeply appreciate the tremendous support of my committee: Howard Conway, Summer Rupper, Ed Waddington, Claire Todd, and Greg Balco. I have learned how to learn from this team.

Several other faculty members at the University of Washington have also been instrumental to my growth as a scientist and as a person. Many thanks are owed to Steve Warren, Eric Steig, Dargan Frierson, Cecilia Bitz, David Battisti, Abby Swann, Al Rasmussen, and LuAnne Thompson.

My community of graduate students in the department of Earth and Space Sciences and the Program on Climate Change is incredible, and I am honored to have worked with and among them. Michelle Koutnik, Emily Newsom, Mike Town, Shelley Kunaseck, Perry Spector, Joe MacGregor, Julia Jarvis, Lora Koenig, Nicole Feldl, Nick Siler, Kevin Wood, Steve Po-Chedley, Adam Campbell, Stu Evans, Clement Miege, Peter Neff, Jessica Lundin, and the Graduate Climate Conference 6 organizing committee are among the most incredible scientists and friends I could imagine.

I am grateful for my communities in Seattle, Cambridge, and elsewhere, including Lisa Ciecko, Brendan O'Donnell, Jodi Wellman, the BAD co-op, my friends from USF, and my Friday group. My ice community has taught me so much about humanity and humility and I am forever changed by my experiences in Greenland and Antarctica: thank you especially to Jake Speed, Kathy Blumm, Kathy Young, Andrea Isgro James, Ken Jessen, and Sandy Starkweather.

I want to thank my family for their incredible and unwavering love and support. Mom, Dad, Pete, Downing, Pax, and Kai have inspired me, cheered for me, and have been with me all the way. I admire each member of my family greatly, and am humbled to be among their lot.

And finally to Matt Smith – words cannot express my love, gratitude, and admiration.

DEDICATION

I dedicate this work to my partner, Matt Smith,
and to my family: Mom, Dad, Pete, Downing, Pax, and Kai.

Chapter 1

INTRODUCTION

Paleoclimate proxies provide a wealth of information about Earth's history, far beyond what is available from the instrumental record. However, proxies are not equivalent to instruments – the nature of *what* and *how* a proxy is deposited must be understood before any meaningful climate information is extracted. In most instances the proxy record is not a direct history of climate, but rather of some other geophysical sub-system (i.e., a tree, a lake, a glacier, an ice sheet, or a soil), that itself has a dynamical response to climate. The size, shape, local climatology, internal dynamics, and non-climatic external forcings of the system all determine the time that it takes to respond to a climatic forcing and the magnitude of that response. Further, the proxy record left by the geophysical system may represent a spatial integration of climatic effects.

This delayed, smoothed, and integrated response to a climate signal is a hallmark of many geophysical systems with memory such as the ocean's mixed layer [Hasselmann, 1976, Frankignoul and Hasselmann, 1977], glaciers [e.g. Oerlemans, 2000, Roe, 2011], lakes [e.g. Mason et al., 1994], ice sheets [e.g MacAyeal, 1992, Huybrechts and de Wolde, 1999], and permafrost soils [e.g. Romanovsky et al., 2007] (see Appendix A). Both the spatial and temporal integration of the climatic forcings can complicate the interpretation of a proxy record giving rise to several questions:

1. What climatic variables, represented by the climate proxy, are well preserved

by the geophysical system?

2. On what timescale is climatic information well preserved?

3. Over what spatial scale does the proxy represent relevant information?

4. How can one distinguish a climatic signal from noise in the proxy record?

5. What physics and parameters is the system most sensitive to?

This dissertation explores three geophysical systems from which paleoclimate proxy records are often derived:

- **Glaciers**, whose length variations are influenced by patterns of accumulation and ablation.

- **Lakes**, whose extent and surface elevation vary in response to evaporation and precipitation.

- **Ice streams**, whose shape and extent are sensitive to changes in sea level, accumulation, and ice-shelf buttressing.

These geophysical systems are studied by applying climatic forcings to relatively simple models that capture the systems' behavior. Despite the models' simplicity, they retain the most essential behaviors of the systems that are being studied. Though the models do not capture all of the nuances of the systems' behavior, their simplicity is also their strength: a thorough understanding of the behavior of the governing equations leads to physical understanding of the system in nature. To some degree, each chapter in this dissertation addresses each of the five questions posed above, though

the emphasis varies for each of the three systems.

1.1 Glaciers

Mountain glaciers are key indicators of regional and global climate change and variability, responding sensitively to changes in precipitation and temperature. However, internal dynamics cause glaciers to integrate variations in precipitation and temperature over timescales longer than a year. The timescale and magnitude of a glacier's response to climate perturbations are functions of both the geometric and climatic setting of the glacier. It is therefore difficult to diagnose whether discrepancies in glacier behavior are due to geometric or climatic heterogeneity.

Glaciers respond to variations in the climate through changes in both the profile and length of the glacier. Because the length of the glacier is relatively simple to diagnose, through terminal moraine deposits or aerial photographs, variations in a glacier's length offer the most straightforward way to track its response to variations in the climate. Nye [1960] showed that these terminal variations are driven by not only the direct effects of snowfall and ice melt, but also to the arrival of ice from the upper part of the glacier. Nye estimated that the time it takes to transfer snowfall to the terminus of an alpine glacier is between 3 and 30 years. With this understanding, much work was done to understand what climatic forcings determine the timing and magnitude of variations in glacier length [e.g. Nye, 1961, 1963, Jóhannesson et al., 1989, Oerlemans et al., 1998, Harrison et al., 2001, Weber and Oerlemans, 2003, Roe, 2011, Oerlemans, 2012, Harrison, 2013].

Reichert et al. [2002] and Roe and O'Neal [2009] each recognized that in addition to responding to climatic change, glacier lengths also vary in response to interannual climate variations. Their work determined the expected amplitude of glacier varia-

tion in response to interannual variations in precipitation and temperature. Length variations that exceed the bounds of this range are indicative of a glacier that is responding to a true climatic shift, rather than a short-term variation in precipitation or temperature.

The shape of the underlying bed and the distribution of ice also control the timing and size of a glacier's response to changes or variations in the climate. These geometric effects can be large. For example, Kessler et al. [2006] showed that 97% of the disparity between the lengths of glaciers flanking the east and west side of California's Sierra Nevada range during the most recent glacial period is attributed to the topographic asymmetry of the mountains. Oerlemans et al. [1998] concluded that while there is no straightforward relationship between glacier size and fractional change in ice volume, hypsometry plays an important role in determining the variability of a glacier, and that, in general, smaller glaciers are more likely to lose a higher percentage of their mass. However, the tendency of larger glaciers to have lower slopes can also expose a large fraction of a large glacier to ablation for the same warming (or same ELA rise). This can be a compensating factor.

Given that both the regional climate and the regional mountain topography are non-homogeneous, it is therefore expected that regional glacier advance and retreat should also be non-uniform. Regional correlations in glacier lengths that are apparent in the historical or proxy record reflect the influence of three factors: spatial correlations in precipitation and melt-season temperature; the climatic setting of the glaciers (e.g. a maritime or continental climate); and a similarity between the glaciers' geometric setting and hypsometric distribution. Chapters 2 and 3 explore the influence the factors on setting the patterns of regional glacier advance and retreat.

1.2 Lakes

Many of the same issues that affect the interpretation of glacier-length records also apply to lake-level records. Lakes that do not have efficient drainage outlets integrate year-to-year climate fluctuations to produce large, persistent fluctuations in lake levels on timescales of decades or longer. A lake integrates climatic information over its entire catchment area, reflecting regional climate signals with a rise or fall in the lake's level. Langbein [1961] noted that closed-basin lakes, which lack drainage outlets (i.e. endorheic basins), fluctuate more than open lakes, because changes in the inflow or outflow of the lake can be compensated only by a change in the lake's surface area. Therefore, closed lakes are particularly sensitive to climate fluctuations, and have been the subject of many paleoclimate studies [Street-Perrott and Harrison, 1985].

One such lake that is particularly well-studied is the Great Salt Lake (GSL). It is tempting to attribute decadal-scale variations in the GSL's lake level to decadal-scale climatic forcings. Mann et al. [1995], Lall and Mann [1995], Moon et al. [2008] and Wang et al. [2010] invoke low-frequency climate phenomena to explain the low-frequency response of the GSL, and aim to predict future lake levels from the periodicity of the atmospheric indices.

However, Kite [1989] proposed that the changes and apparent periodicity in the GSL's record are within the range of normal fluctuations and cannot be cited as an indication of climatic change. Mohammed and Tarboton [2011] showed that the timing of increases and decreases in lake level are directly related to the GSL's bathymetry. Because the area of the lake controls the outgoing flux, a shallow lake like the GSL is quickly stabilized and modulated by the available evaporative surface. In related work, they used a model to calculate the sensitivity of the GSL to changes in the historical inflow, precipitation, and air temperature, and use these historical records

to predict possible future lake-level scenarios [Mohammed and Tarboton, 2012].

Mason et al. [1994] derived general solutions to the water-balance equation that characterized the lake-level response to idealized climate forcings, showing how closed-basin lakes act as low-pass climate filters. In Chapter 4, I apply a similar model, putting the historical record of the GSL into context by considering the natural variability of the lake's level, which occurs in response to the year-to-year fluctuations in weather that occur even without any climate change or persistence in the climate. I derive analytic solutions for the standard deviation of lake-level changes, the threshold-crossing frequency of a lake, and the sensitivity to variations in precipitation versus temperature. Chapter 4 also demonstrates the important role of lake bathymetry on integrating natural lake-level variability.

1.3 Ice Streams

Advances in the physical understanding of marine ice sheet stability, coupled with evidence that the West Antarctic Ice Sheet (WAIS) has collapsed in the past [Hillenbrand et al., 2012], have led to recent concerns about the WAIS's future stability. The total potential sea-level contribution from the WAIS is ∼4.3 m [Fretwell et al., 2013], and recent work suggests that Antarctica could contribute 0.15 to 0.62 m to global sea-level rise in the next century [Solomon et al., 2007, Pfeffer et al., 2008, Joughin et al., 2010, Gladstone et al., 2012, Mouginot et al., 2014, Joughin et al., 2014]. Similarly, the distribution of ice on the Antarctic continent during the last glacial period, as well as a comprehensive understanding of its retreat to the present state remains unknown [e.g. Anderson et al., 2002, Clark et al., 2009]. The difficulty in predicting future change, or resolving past change, stems, in part, from the complexity of ice/ocean dynamics [Joughin and Alley, 2011, Nowicki et al., 2013].

However, recent advances in remote sensing offer an unprecedented insight into the present state of the ice sheet, including observations of ice-thickness, basal topography, and surface velocity [Fretwell et al., 2013, Rignot et al., 2008, Le Brocq et al., 2010, Rignot et al., 2011, Fretwell et al., 2013]. These data sources, in combination with advances in the theoretical understanding of ice-sheet-shelf-ocean interactions allow us to gain perspective on the stability of the WAIS, using numerical models [Schoof, 2007, Gagliardini et al., 2010, Drouet et al., 2012].

In an idealized steady state, the flux of ice from the margins of the ice sheet is balanced by the accumulation integrated over the upstream catchment area. In reality, the mass balance of the ice sheet is continuously being modified by changes in the activity of fast-flowing outlet glaciers and ice streams. The volume of ice that is discharged from these outlets is determined by changing conditions at the grounding line, the transitional area between the grounded ice sheet and the floating ice shelf. The grounding line, in turn, is highly sensitive to changes in sea-level and the melting/freezing of buttressing ice shelves [Payne et al., 2004, Joughin et al., 2010, Pritchard et al., 2012, Shepherd et al., 2012]. Schoof [2007] showed that the grounding-line position is determined by the basal topography and is therefore extremely sensitive to changes in the bed beneath and extending outward from the grounded ice.

The position of the grounding line exerts a strong control over the inland ice-elevation profile. Glacial erratics, which are collected from nunataks and dated with cosmogenic nuclide techniques, can offer evidence of past ice-thickness changes [e.g. Balco et al., 2008]. This paleo-evidence, coupled with physical understanding from a model, can inform us how ice streams respond to changes in the grounding line.

In Chapter 5, I use an idealized flowline model to assess the relative importance

of environmental variations and physical parameters on ice-stream thickness profiles. Sub-glacial and sub-marine basal topography, together with the assumed form of the grounding-line flux, controls the grounding-line sensitivity to change. Results emphasize that differences in the basal relief beneath present-day ice streams will cause the Weddell, Amundsen, and Ross Sea sectors of Antarctica to respond with varying sensitivity to similar environmental perturbations.

1.4 Conclusion

I return now to the initial five questions that motivate this work, and detail how each chapter of my dissertation will answer each of these questions:

1. *What climatic variables, represented by the proxy, are well preserved by the geophysical system?*
   I derive linearized formulas for the ratio of sensitivity of glaciers/lakes to changes in accumulation (precipitation) and mass loss (melt/evaporation). The ice-stream chapter uses sensitivity analyses to characterize the potential changes in ice thickness due to changes in accumulation, sea level, and ice shelf buttressing.

2. *On what timescale is climatic information well preserved?*
   Characteristic response times are derived from the linearized glacier and lake level models. The sensitivity of the ice-stream model to physical and environmental factors enhances our understanding of how well ice-stream models can capture the changes observed in exposure-age data.

3. *Over what spatial scale does the proxy represent relevant information?*
   The mountain glacier work expressly answers this question with correlation analysis. Similar work could be done with the lake model, but is not part of

this dissertation. For the ice stream, my results imply that the near-grounding-line elevations will reflect regional ice sheet/shelf condition.

4. *How can one distinguish a climatic signal from noise in the proxy record?*
   Roe and O'Neal [2009] used statistical analysis to estimate the variability of glaciers due to climate variability alone. I have used a similar approach in my work with lakes. For ice streams, I compare the ice-profile response to variations in accumulation, bed slipperiness, and relative sea level. This intra-model comparison can then be compared to the magnitude of ice-thickness changes from the Last Glacial Maximum to the present.

5. *What physics and parameters is the system most sensitive to?*
   All three chapters identify the primary sensitivity of the systems that are addressed. The main advantage to my idealized modeling approach is that the physics and parameters are easily identified and altered, and that comparisons between model configurations are straightforward, allowing for clear interpretations of the modeling results.

Chapter 2

SPATIAL PATTERNS OF GLACIERS IN RESPONSE TO SPATIAL PATTERNS IN REGIONAL CLIMATE

Chapter 2, in full, is a reprint of "Spatial Patterns of Glaciers in Response to Spatial Patterns in Regional Climate" authored by K. Huybers and G. H. Roe. This is the author's version of the work. It is posted here by permission of the American Meteorological Society (AMS) for personal use, not for redistribution. The definitive version was published in Journal of Climate 22.17 in 2009, and AMS holds the copyright. The dissertation author was the primary investigator and author of this paper.

2.1 Introduction

A major goal in current climate research lies in understanding patterns in climate and how they translate to climate proxies. Glaciers are among the most closely studied of these proxies because they respond directly to both snow accumulation and surface energy balance. These, in turn, reflect the precipitation and melt-season temperature of the regional climate [Ohmura et al., 1992]. A glacier's response to this climate is most often characterized by a change in the position of its terminus. Records of terminus advance and retreat are readily available in both the geological and historical record through the formation of moraines, lichenometry, aerial photography, cosmogenic dating, and satellite imagery. Beyond the period of the instrumental record, well-dated glacial deposits often serve as the primary descriptor of the climate history of a region.

Despite the direct nature of a glacier's response to climate, both the current near-global retreat and past glacier variations present complicated pictures. Though there is strong evidence that glaciers worldwide are presently retreating [e.g. Oerlemans, 2005], individual glaciers vary in the magnitude of response. In a few locations, glaciers have even advanced during the past decades, as is the case in Norway and New Zealand [e.g. Nesje, 2005, Chinn et al., 2005]. Moreover, some well-documented retreats like that on Mount Kilimanjaro have complicated causes that are not easily explained [e.g. Mölg and Hardy, 2004]. While there is often local coherence among glacial advances and retreats, it has proven harder to extrapolate these results across continental-scale regions [e.g. Rupper and Roe, 2008].

The difficulty in interpreting terminus advance and retreat is threefold. First, glaciers are not indicators of a single atmospheric variable. They reflect the effect of many atmospheric fields, primarily accumulation and temperature, but also cloudiness, wind, longwave and shortwave radiation balances, the turbulent fluxes of sensible and latent heat, and humidity, among others. Second, each glacier is subject to a particular combination of the bed slope, hypsometry, accumulation area, debris cover, local shading, etc., creating a setting that is unique to each glacier. Finally, glaciers integrate the interannual variability of the climate over many years or even decades; the advance or retreat of a glacier cannot be traced to a single years climate.

Hence, in order to understand how spatial patterns in climate variability translate into spatial patterns of glacial response, we must systematically analyze patterns in regional climate and model a glacier's response to the dominant variables. These patterns of climate variability and glacier response must be understood in order to establish the natural variability of a glacier (i.e., the variability in the absence of an external climate forcing). It is only when observed responses exceed this expected natural variability that glaciers can be said to be recording a true regional, hemi-

spheric, or global climate change [e.g. Reichert et al., 2002, Roe and O'Neal, 2009, hereafter RO].

The goal of this paper is to derive and analyze a model of the expected regional-scale correlations of glacier length variations in response to interannual variability in precipitation and melt-season temperature. We take a first-order approach to this problem, using the simplest model framework capable of representing how glaciers amalgamate different aspects of climate to produce terminus variations. In particular, we address the following questions:

1. What are the spatial patterns of variability in precipitation and melt-season temperature?

2. How do these patterns of intrinsic climate variability translate into patterns of glacier advance and retreat?

3. Over what spatial extent can we expect these intrinsic, natural fluctuations of glaciers to be correlated?

We use a simple linear glacier model that has been shown to adequately capture recent glacier variability [RO; Jóhannesson et al., 1989, Oerlemans, 2005]. The patterns we find in our results are consistent with those of other glacier mass balance studies [Harper, 1993, Bitz and Battisti, 1999]. The advantage of our approach is that it allows us to explore such patterns on a wider, regional scale and to understand in detail the relative importance of the different causes.

Our modeled patterns of glacier advance and retreat are not intended to simulate either the recent or the paleorecord of glacier advance and retreat. First, this is because we have chosen to explore only the interannual variability of climate and have

removed any trend from the data. Second, and more fundamentally, accounting for the processes that build up and deposit moraines on the landscape, and particularly the time scale of their formation, is beyond the scope of our chosen model [e.g. Putkonen and O'Neal, 2006]. We regard our results, therefore, as a means to explore how climate patterns are combined through the dynamical glacier system and as an aid in the interpretation of glacial landscape features.

2.2 Setting and data

Our study area is the Pacific Northwest, covering the northwestern United States, British Columbia, and southern Alaska. This region is ideal because of the large number of well-documented glaciers, the different climatic environments, and the range of glacier sizes that exist in the region. The dominant climate patterns in the area are also well understood. Figure 2.1 maps the locations of all major glaciers in the region.

Our principal climate data set is that of Legates and Willmott [1990a,b, hereafter LW50] which provides 50 years of worldwide temperature and precipitation station data interpolated onto a $0.5^\circ \times 0.5^\circ$grid. We extract from this data set two atmospheric variables that reflect the most important climatic forcing for glaciers. The first variable is the melt-season temperature, which we define as the average surface temperature between June and September (JJAS). For simplicity, we assume that the ablation rate is directly proportional to the melt-season temperature, as suggested by observations [e.g. Paterson, 1994, Ohmura et al., 1992]. The second variable is the mean annual precipitation, which, again for simplicity, we assume reflects the accumulation of snowfall on a putative glacier within any grid point. Approximately 80% of precipitation in this region comes in the fall and wintertime [e.g. Hamlet et al., 2005]. To distinguish in more detail between precipitation and snowfall would require extrapolation onto high-resolution topographic digital elevations models. The data

are linearly detrended in order to identify the internal variability in these climate variables and, so, neglect any recent warming.

These simplifications are appropriate for the first-order approach in this study, its focus on the regional-scale response, and the relatively coarse 0.5°-resolution data that does not reflect detailed small-scale orographic features. We discuss refinements of the model framework in section 5 and the discussion.

2.2.1 Climate in the Pacific Northwest

Figures 2.2A and B depict the mean annual precipitation and the mean melt-season temperature over the region. The Cascade, Olympic, Coast, and St. Elias Mountains are important influences on the regions climate. These mountain ranges partition the setting into a generally wet region on the upwind flank of the mountains and a dry region toward the leeward interior. On a smaller scale, not resolved in Fig. 2, there are distinct patterns in climate over the peaks and valleys in the mountain ranges, giving rise to rich and intricate local weather patterns [e.g. Minder et al., 2008, Anders et al., 2007]. We address the important effect of these small-scale patterns in section 2.5. For mean melt-season temperature, the pattern is characterized by the north-south gradient, though cooler temperatures at higher elevations can also be seen.

The major feature of the regional atmospheric circulation pattern is the Aleutian low pressure system. The effects of the dominant modes of climate variability influencing the region [e.g., El Niño [e.g. Wallace et al., 1998], the Pacific decadal oscillation [e.g. Mantua et al., 1997], and Pacific-North American pattern [e.g. Wallace and Gutzler, 1981])] can all be understood in terms of how they shift the position and intensity of the Aleutian low. These shifts result in a dipole-like pattern, with storms having a tendency to track either north or south, depending on the phase of the mode,

and leaving an anomaly of the opposite sign where the storminess is reduced.

The natural year-to-year variation observed in the region's climate system is well characterized by the standard deviations in annual temperature and precipitation from LW50. Figure 2.2C shows a simple relationship: the interannual variability of precipitation is higher where the mean precipitation is also high. However, for melt-season temperature, the picture is different. Whereas the mean was dominated by the north-south gradient, the variability of melt-season temperature (Fig. 2.2D) is higher inland, reflecting the continentality of the climate.

2.2.2 Glaciers in the Pacific Northwest

The high annual precipitation totals and widespread high-altitude terrain within this area are conducive to the existence of glaciers. The region's glaciers have been extensively mapped, as have their changes over recent geologic history [e.g. Harper, 1993, Hodge et al., 1998, ONeal, 2005, Pelto and Hedlund, 2001, Post, 1971, Porter, 1977, Sapiano et al., 1998, Sidjak, 1999]. The glaciers in the region range from the massive tidewater glaciers in southern Alaska to small ice patches in steep terrain. In this study, we focus on the many temperate alpine glaciers in the area because these are the best suited to reflect a "clean" signature in their response to climate. Even among these temperate glaciers, there is a wide range in size and shape, giving rise to individual variations in advance and retreat.

These advances and retreats cannot be interpreted as responses to long-term climate changes alone. Climate is, by definition, the statistics of weather. In other words, it is the probability density distribution of the full suite of variables that describe the state of the atmosphere over some specified period of interest. (The World Meteorological Organization defines climate as the statistics within any 30-yr period.)

A stationary climate, therefore, has constant statistics with a given mean, standard deviation, and higher-order moments. Glaciers are dynamical systems that integrate this natural year- to-year climate variability. This integrative quality of glaciers means that, even in a constant climate, the length of glaciers will vary on decadal and centennial time scales [e.g. RO; Reichert et al., 2002, Roe, 2009].

2.3 A linear glacier model

A schematic of the linear model employed in this study is shown in Fig. 2.3. The model is from RO, which is based on that of Jóhannesson et al. [1989]. The model neglects ice dynamics and assumes that any imbalance between snow accumulation and ice ablation is immediately expressed as a rate of change of the terminus position. Other aspects of the glacier geometry are specified. The absence of glacier flow dynamics means that the linear model is not damped enough on short time scales (e.g., RO), but on decadal time scales and longer this model, and similar ones are able to reproduce realistic glacier variations for realistic climate forcings [RO; Oerlemans, 2001, Harrison et al., 2001].

Climate is specified by an annual accumulation rate of P (m yr^{-1}) and an average melt-season temperature T. Ablation is assumed to be linearly proportional to T (°C), where the constant of proportionality is given by the melt-rate factor μ. Observations suggest that μ ranges from 0.50 to 0.84 m yr^{-1} $°C^{-1}$, water equivalent [e.g. Paterson, 1994]. The lapse rate Γ is taken to be a constant 6.5 °C km^{-1}.

Let $\bar{L}$ be the equilibrium glacier length that would result from constant T and P, the long-term averages of the melt-season temperature and the precipitation. The model calculates the time evolution of perturbation in glacier length L' that arises from the interannual anomalies in the melt-season temperature, T', and annual pre-

cipitation, P'. From here on, we drop the prime symbol and use L, T, and P to represent the anomalies in length, melt-season temperature, and precipitation.

RO show that perturbations in glacier length L away from the equilibrium glacier length for a given constant climate can be described by the following equation:

$$L_{t+\Delta t} = \left(1 - \frac{\mu\Gamma \tan\phi A_{abl}\Delta t}{wH}\right) L_t - \left(\frac{\mu A_{T>0}\Delta t}{wH}\right) T_t + \left(\frac{A_{tot}\Delta t}{wH}\right) P_t \equiv \gamma L_t - \alpha T_t + \beta P_t. \tag{2.1}$$

The model geometry and parameters are defined in Fig. 2.3, t is time in years, and Δt is the interval between successive time steps, which we take to be one year.

Most of the correlations presented in this paper are calculated with respect to Mount Baker in the Cascade Mountains of Washington state (48.7°N, 121.8°W). Mount Baker is a large stratovolcano, flanked by eight glaciers with a broad range of sizes and shapes. Mount Baker was chosen because the history of its glaciers is well documented [ONeal, 2005], its climatic setting is well understood, and its glaciers generally fit well into the simple geometrical constraints of the model (i.e., no sharp corners). Doing so also complements the analysis in a companion study (RO).

Table 2.1 shows the range in the model parameters and geometry that is reasonable for typical Alpine glaciers in this region, taken from RO. Ablation areas are calculated from the total area, using the accumulation area ratio (AAR), the ratio of $1 - A_{abl}$ to A_{tot}, which has been shown to vary from 0.6 to 0.8 in this region [e.g. Porter, 1977]. For simplicity, we group the parameters for the three terms in eq. (2.1) into the coefficients γ, α, and β, respectively. Here γ ranges between 0.81 and 0.97 (and is unitless), α between 9 and 81 m $^{\circ}C^{-1}$, and β between 85 and 240 yr, depending on the choice of parameters and the size of the glacier. Note that α has the largest

uncertainty owing to the large uncertainties in μ and in the AAR, both of which, in principle, can be observed and therefore constrained much better for any specific glacier. Table 2.1 also shows a standard set of typical parameters, which we use for all calculations from now on, unless otherwise stated.

Equation (2.1) describes a glacier that advances (retreats) if melt-season temperatures are anomalously low (high) or if the accumulation is anomalously high (low). It is the discrete form of a simple first-order ordinary differential equation that has a characteristic response time. In the absence of any climate anomalies the glacier asymptotes exponentially back to its equilibrium length with a characteristic e-folding time scale of:

$$\tau \equiv \frac{\Delta t}{(1-\gamma)} = \frac{wH}{\mu\Gamma \tan\phi A_{abl}}.$$

For Mount Baker glaciers, τ ranges from 5 to 30 yr (Table 2.1), consistent with other estimates for these small mountain glaciers. In the presence of climate forcing, τ represents the decorrelation time scale, or "memory" of the glacier. RO and Roe [2009] demonstrate that, because of this memory, a fundamental property of glaciers is that they will naturally undergo persistent multidecadal and centennial fluctuations, even in the absence of any persistent climate anomalies.

RO also show that this linear model is able to capture typical magnitudes of glacier variations in the Cascade Mountains of Washington State and, so, is adequate to capture the approximate response of glacier length to large-scale patterns of P and T. Caveats and possible improvements to the model are noted in the discussion.

2.4 Results

2.4.1 Glacier correlations

The aim of this study is to explore how patterns of glacier-length variations are driven by patterns of climate. From eq. (2.1) an expression can be derived for the correlation between the length variations of two glaciers located at two different locations (denoted A and B) in terms of the correlations between T and P:

$$L_{A,t+1} = \gamma_A L_{A,t} - \alpha_A T_{A,t} + \beta_A P_{A,t}, \tag{2.2a}$$

$$L_{B,t+1} = \gamma_B L_{B,t} - \alpha_B T_{B,t} + \beta_B P_{B,t}. \tag{2.2b}$$

The expected value (denoted by angle brackets) of the correlation between glaciers A and B is

$$\begin{aligned}\langle L_{A,t+1} L_{B,t+1}\rangle = {} & \gamma_A\gamma_B\langle L_{A,t}L_{B,t}\rangle + \alpha_A\alpha_B\langle T_{A,t}T_{B,t}\rangle \\ & + \beta_A\beta_B\langle P_{A,t}P_{B,t}\rangle - \gamma_A\alpha_B\langle L_{A,t}T_{B,t}\rangle \\ & + \gamma_A\beta_B\langle L_{A,t}P_{B,t}\rangle - \alpha_A\gamma_B\langle T_{A,t}L_{B,t}\rangle \\ & + \beta_A\gamma_B\langle P_{A,t}L_{B,t}\rangle. \end{aligned} \tag{2.3}$$

Cross terms in temperature and precipitation (i.e., $\langle T_{A,t}P_{B,t}\rangle$) have been neglected in eq. (2.3) because calculations show that in this region they are not statistically significant at a 95% confidence level.

Here $\langle L_{A,t}L_{B,t}\rangle$ is the covariance of L_A and L_B, which is in turn equal to the correlation between L_A and L_B ($\equiv r_{L(A,B)}$), our desired answer, multiplied by the standard deviations of L_A and L_B. The covariances $\langle T_{A,t}T_{B,t}\rangle$ and $\langle P_{A,t}P_{B,t}\rangle$ can be calculated from observations. However, the other terms in (3) are in need of additional manipulation. We elaborate below on $\langle L_{A,t}T_{B,t}\rangle$. The other terms can be derived in a similar

fashion.

From the definition of the correlation between T_A and T_B we can write

$$\langle T_{B,t} \rangle = \sigma_{T,B} \left(r_T \frac{\langle T_{A,t} \rangle}{\sigma_{T,A}} + (1 - r_T^2)^{1/2} \nu_t \right) \tag{2.4}$$

where r_T is the correlation of melt-season temperature between points A and B, $\sigma_{T,()}$ is the standard deviation of T at point ( ), and we assume that the residual $\nu_t t$ is a Gaussian-distributed random number of unit variance at time t.

Using the right-hand side of eq. (2.4), the value for $\langle L_{A,t} T_{B,t} \rangle$ can be rewritten as

$$\langle L_{A,t} T_{B,t} \rangle = r_T \frac{\sigma_{T,B}}{\sigma_{T,A}} \langle L_{A,t} T_{A,t} \rangle, \tag{2.5}$$

where we have used the fact that there is no correlation between a random number and $L_{A,t}$. That is, $\langle L_{A,t} \nu_t \rangle = 0$.

So, to find $\langle L_{A,t} T_{B,t} \rangle$ we need $\langle L_{A,t} T_{A,t} \rangle$. First, T_A can be written in terms of its autocorrelation, $\rho_{T,A}$, and the residuals, which we assume are governed by another Gaussian-distributed white noise process, λ_t:

$$T_{A,t} = \rho_{T,A} T_{A,t-1} + (1 - \rho_{T,A}^2)^{1/2} \lambda_t \tag{2.6}$$

Therefore, using eqs. (2.6) and (2.2a) we can write

$$\langle L_{A,t} T_{A,t} \rangle = \gamma_A \rho_{T,A} \langle L_{A,t-1} T_{A,t-1} \rangle - \alpha_A \rho_{T,A} \langle T_{A,t-1}^2 \rangle \tag{2.7}$$

where again we use the fact that $\langle L_{A,t}\lambda_t\rangle = 0$.

Since the expected value of a distribution of numbers is independent of the time step $\langle L_{A,t}T_{A,t}\rangle = \langle L_{A,t-1}T_{A,t-1}\rangle$, we rewrite eq. (2.7) as

$$\langle L_{A,t}T_{A,t}\rangle = \frac{-\alpha_A \rho_{T,A}\sigma^2_{T,A}}{1-\gamma_A\rho_{T,A}} \tag{2.8}$$

Therefore, the expected correlation between L_t and T_t is a function of the magnitude of $T(\sigma_T)$, the autocorrelation of $T(\rho_T)$, and the memory of the glacier (γ_A).

Finally, inserting the right hand side of eq. (2.8) into eq. 2.5) yields

$$\langle L_{A,t}T_{B,t}\rangle = \frac{-\alpha_A r_T \rho_{T,A}\sigma_{T,A}\sigma_{T,B}}{1-\gamma_A\rho_{T,A}}. \tag{2.9}$$

Derivations directly analogous to the above can be used for the remaining terms in eq. (2.3) and yield an equation for the correlation of glacier lengths between A and B:

$$r_{L(A,B)} = \frac{1}{(1-\gamma_A\gamma_B)\sigma_{L,A}\sigma_{L,B}}\left[r_T\alpha_A\alpha_B\sigma_{T,A}\sigma_{T,B}\left(1+\frac{\gamma_A\rho_{T,A}}{1-\gamma_A\rho_{T,A}}+\frac{\gamma_B\rho_{T,B}}{1-\gamma_B\rho_{T,B}}\right)\right.$$
$$\left. + r_P\beta_A\beta_B\sigma_{P,A}\sigma_{P,B}\left(1+\frac{\gamma_A\rho_{P,A}}{1-\gamma_A\rho_{P,A}}+\frac{\gamma_B\rho_{P,B}}{1-\gamma_B\rho_{P,B}}\right)\right] \tag{2.10}$$

The terms relating to climate ($r_T, r_P, \sigma_T, \sigma_P, \rho_T, \rho_P$) can all be calculated from observations.

Equation (2.10) reveals that the correlations between the lengths of glaciers in different places are dependent on both the relationships between climate variables and the geometries of the glaciers in question. The variables and parameters are the correlation of the climate variables (r_T, r_P); the standard deviations of the glacier length (σ_L), precipitation (σ_P), and melt-season temperature (σ_T); the memory of the glacier (γ) and climate (ρ_T, ρ_P); and finally the size and shape of the glacier (α, β). We will now discuss each of these factors in turn and how their respective ranges of uncertainty affect the correlations between glaciers.

2.4.2 The spatial correlation of the climate variables

Spatial correlations between glacier behavior are fundamentally driven by spatial correlations in the climate: eq. (2.10) shows that $r_{L(A,B)}$ is equal to a linear combination of $r_{T(A,B)}$ and $r_{P(A,B)}$. From LW50 we calculate at each grid point the correlations of T and P with their values at Mount Baker (Fig. 2.4). As expected, r_T and r_P are high in areas surrounding Mount Baker. However, the spatial extent of significant r_T is much greater than that of r_P. Variations in T are dependent on the perturbations in the summertime radiation balance, which appear to be fairly uniform over the region.

A striking feature of r_P is the anti-phasing between Washington and southeastern Alaska. The dipole pattern results from the tendency of storms to be more prevalent in one of the two regions, leaving the other relatively dry. The smaller area of significant values of r_P reflects the smaller spatial scale of precipitation patterns.

2.4.3 The relative importance of T and P for a glacier

While the correlations in T and P are the main factors in correlations in L, the relative importance of T or P for glacier length also matters. In what follows, we determine

the ratio of length variations forced only by T (denoted as $\sigma_{L,T}$) to length variations forced only by P (denoted as $\sigma_{L,P}$).

These expressions can be derived from eq. (2.1). Setting $P = 0$, the expected value of a glaciers length forced only by T is

$$\langle L_{t+1}^2 \rangle = \gamma^2 \langle L_t^2 \rangle + \alpha^2 \langle T_t^2 \rangle - 2\gamma\alpha \langle L_t T_t \rangle \tag{2.11}$$

Using our derivation for $\langle L_t T_t \rangle$, from eq. (2.8), the variance of the expected length can be written

$$\sigma_L^2 = \gamma^2 \sigma_L^2 + \alpha^2 \sigma_T^2 + \frac{2\gamma\alpha^2 \rho_T \sigma_T^2}{1 - \gamma\rho_T} \tag{2.12}$$

Rearranging eq. (2.12), the standard deviation for a glacier forced only by T is

$$\sigma_{L,T} = \alpha_T \sigma_T \sqrt{\frac{1}{1-\gamma^2}\left(1 + \frac{2\gamma\rho_T}{1-\gamma\rho_T}\right)} \tag{2.13}$$

Similarly, the expression for a glacier forced only by P is

$$\sigma_{L,P} = \beta_P \sigma_P \sqrt{\frac{1}{1-\gamma^2}\left(1 + \frac{2\gamma\rho_P}{1-\gamma\rho_P}\right)} \tag{2.14}$$

The ratio R between the two is therefore

$$R = \frac{\sigma_{L,T}}{\sigma_{L,P}} = \frac{\alpha}{\beta}\frac{\sigma_T}{\sigma_P}\sqrt{\frac{1 + \frac{2\gamma\rho_T}{1-\gamma\rho_T}}{1 + \frac{2\gamma\rho_P}{1-\gamma\rho_P}}}. \tag{2.15}$$

From eq. (2.1), α/β can be rewritten as $\mu A_{T>0}/A_{tot}$, and the ratio of the glacier length sensitivity to melt-season temperature and precipitation fluctuations can also be written:

$$R = \frac{\sigma_{L,T}}{\sigma_{L,P}} = \frac{A_{T>0}}{A_{tot}}\frac{\mu\sigma_T}{\sigma_P}\sqrt{\frac{1 + \frac{2\gamma\rho_T}{1-\gamma\rho_T}}{1 + \frac{2\gamma\rho_P}{1-\gamma\rho_P}}}. \tag{2.16}$$

The terms $\frac{2\gamma\rho_T}{1-\gamma\rho_T}$ and $\frac{2\gamma\rho_P}{1-\gamma\rho_P}$ in eqs. (2.15) and (2.16) are similar to one another. Because γ is always less than one and calculations (not given) show that values for $\rho_{T,P}$ are typically close to 0.2 - 0.3, the ratio of these terms will be close to one.

To convey a clear sense of the regional coherence of glacier patterns, we present our analyses as if there were a hypothetical glacier at each grid point in the figure. In other words, we imagine that, within each grid point in the LW50, there is a mountain high enough to support glaciers. This is simply a device for clarity of presentation– comparison with real glaciers comes directly from Fig. 2.1.

Figure 2.5A shows R for the standard set of parameters. To convey a sense of the uncertainty in R, we also combine the highest melt rate with the lowest AAR and the lowest melt rate with the highest AAR (Figs. 2.5B and C). Overall, the calculations suggest that over most of the area glaciers are more sensitive to melt-season temperature than to precipitation, except for a narrow coastal band where glaciers are always more sensitive to P because of the high precipitation variability and muted melt-season temperature variability (i.e., Fig. 2.2). However, the extent of T dependence varies greatly depending on the choice of parameters. Glaciers with a high melt factor or a large ablation area are much more likely to be affected by variations in T. In section 2.5 we explore how small-scale patterns of climate, not resolved at this scale, can affect this answer.

2.4.4 Standard deviations

From eq. (2.10) it can be seen that the standard deviation of T or P and the standard deviation of L affect $r_{L(A,B)}$ directly. Because σ_T and σ_P also strongly influence the sensitivity of glacier length changes (section 4c), their magnitudes can greatly increase or decrease the importance of R and σ_L.

We derive a formula for σ_L from the root of the sum of the squares of eqs. (2.13) and (2.14):

$$\sigma_L = \left\{ \frac{1}{1-\gamma^2} \left[\alpha^2 \sigma_T^2 \left(1 + \frac{2\gamma\rho_T}{1-\gamma\rho_T} \right) + \beta^2 \sigma_P^2 \left(1 + \frac{2\gamma\rho_P}{1-\gamma\rho_P} \right) \right] \right\}^{1/2} \tag{2.17}$$

Figure 2.6 shows σ_L for standard parameters; values range from 100 to over 300 m. Along the coasts σ_L is high, and σ_P is also high. Southeast British Columbia also has above-average values in σ_L, corresponding to high values in σ_T.

2.4.5 Correlations between glaciers with the same geometry

We now apply eq. (2.10) to each grid point in LW50 and correlate a hypothetical glacier at that point with a glacier that rests on Mount Baker. We begin by imposing the same γ, α, and β at each point, taking values characteristic for a Mount Baker glacier (Table 2.1), to eliminate differences in correlation due to geometry and thus isolate the effect of spatial patterns in climate. The effect of differences in geometry and choices in parameters will be addressed in the following section.

Figure 2.7 shows the expected correlations between a theoretical glacier at each point and a glacier resting on Mount Baker. The correlations between glaciers are strongest where both T and P are well correlated with Mount Baker. On the southeast coast of Alaska r_L is somewhat negative, where P is most strongly anticorrelated with Mount Baker and the glaciers are most sensitive to P. These results are consistent with those of Bitz and Battisti [1999]. There are also regions where T dominates. For example, the strong sensitivity to T northeast of Mount Baker (Fig. 2.5), where r_T is also high (Fig. 2.4B), gives rise to strong glacier correlations. Little to no correlation can be expected in regions where both the T and P correlations with Mount Baker

are low and the value of R is ambiguously close to one, such as is the case in northern British Columbia and the Yukon Territory of Canada.

Inferences of the spatial extent of past climate changes are often made by comparing the reconstructed dates of relict moraines. Given the point made in this study that regional correlations in glaciers also arise from natural interannual variability alone (i.e., in a constant climate), there is some chance that concurrent advances would be misinterpreted. Furthermore, the statistical significance of a hypothesized change in climate is difficult to establish from the few points that are typically available from even well-dated moraines. The integrative nature of a glacier gives it a memory of previous climate states and means that the number of independent observations is much lower than the number of years in a record. In Appendix B, we show calculations for deriving the appropriate number of degrees of freedom using our model, given the autocorrelation of both the glaciers and the T and P values.

2.4.6 Correlations between glaciers with differing geometries

Assuming that all glaciers have the same geometry is clearly a simplification. We expect the spatial correlation between glaciers to weaken if we compare glaciers of different geometries. Because we cannot present the full range of glacier geometries at every point, we focus on locations that are representative of the range of different climatic correlations with Mount Baker. These locations, shown in Fig. 2.1, were chosen to encompass as large a range as possible for this region of r_P, r_T, and R values and are detailed in Table 2.2.

We consider five combinations of glacier parameters (the five main glaciers of Mount Baker, given in Table 2.1) and three values for the AAR at each of the five points. Then we correlated the terminal advance and retreat with that of a typical

glacier on Mount Baker, with an AAR of 0.7 and μ of 0.67 m yr^{-1} $°C^{-1}$. The values of r_L calculated with respect to Mount Baker, as well as r_T and r_P, are shown in Fig. 2.8.

The correlations are strikingly insensitive to this range of parameter variations. Here r_T and r_P are the main drivers of the correlation between glaciers. Differences in the basic geometry are of secondary importance. To the extent that parameters do matter, the variations in the AAR and μ are of most importance (RO).

2.5 Small-scale patterns

While the LW50 data set has the advantage of a long record, it lacks the small-scale detail of climate patterns due to individual mountain peaks and valleys that strongly influence the behavior of individual glaciers. Since 1997 the fifth-generation Pennsylvania State UniversityNational Center for Atmospheric Research Mesoscale Model (MM5) [Grell et al., 1994] has been run (by the Northwest Regional Modeling Consortium at the University of Washington) at 4-km horizontal resolution over the Pacific Northwest [Mass et al., 2003, Anders et al., 2007, Minder et al., 2008]. Though the short interval of the model output makes statistical confidence lower, it is instructive to evaluate the patterns of temperature and precipitation over the region on such a fine grid and repeat the calculations that we performed using LW50. RO find good correspondence between the MM5 output and snowpack telemetry (SNOTEL) observations in the vicinity of Mount Baker. The performance of the MM5 model in this region, relative to observations, has also been evaluated by Colle et al. [2000].

The patterns in the mean annual precipitation in Washington State (Fig. 2.9A) are dominated by the Olympic and Cascade Mountains. Localized maxima in precipitation near individual volcanic peaks can be identified. The pattern of interannual variability of annual precipitation, measured by the standard deviation, is similar to

the pattern of the mean precipitation. Mean melt-season temperatures in the region (Fig. 2.9B) are dominated by elevation differences, with colder temperatures recorded in the mountains. Interannual variability in the mean melt-season temperature, in contrast with precipitation, is fairly uniform over the region (Fig. 2.9D), but the amplitude is increased somewhat and exceeds 18°C yr^{-1} in places (Fig. 2.9B).

Using eq. (2.15), the spatial pattern in R can be plotted for the standard set of parameters (Fig. 2.10). Owing to the high interannual variability in annual precipitation, the variability of glaciers in the Cascades and Olympic Mountains is predicted to be most sensitive to variability in precipitation. This is confined to the high elevations. Lower elevation points, dominated by temperature variability, are not able to sustain actual glaciers in the modern climate.

The high levels of precipitation variability in the mountains also drive high values of the standard deviation in glacier length, exceeding 1400 m in places (Fig. 2.11). By definition of the standard deviation, the glacier would spend approximately 30% of its time outside of the $\pm 1\sigma$ variations. Thus over the long term, fluctuations of 2 - 3 km in glacier length should be expected, driven solely by the interannual variability inherent to a constant climate (RO). This result highlights the crucial importance of knowing small-scale patterns of climate in mountainous regions in determining the response of glaciers.

On this spatial scale, interannual climate variations from the MM5 model output are very highly correlated in space. This translates into very high spatial correlations in glacier response (not shown).

2.6 Summary and discussion

A simple linear glacier model has been combined with climate data to address how regional-scale patterns in precipitation and melt-season temperature combine to produce regional-scale patterns in glacier response. In our model framework, correlations in the glacier lengths are a linear combination of the spatial correlations in the climate variability. The climate correlations are modified by the relative importance of temperature and precipitation to the glacier response, which in turn is a function of the glacier geometry and mass balance parameters.

In coastal regions high precipitation variability and low melt-season temperature variability mean that the patterns of glacier response are controlled by the patterns of precipitation variation. Conversely, in continental climates patterns of glacier response are most influenced by the patterns in melt-season temperature. Results are quite insensitive to variations in glacier geometry – it is the spatial patterns in T and P that are the key drivers of spatial patterns in glacier variations.

Finally, using seven years of archived output from a high-resolution numerical weather prediction model shows that the increased total precipitation and precipitation variability characteristic on individual coastal mountain peaks will give rise to large variations in glacier advance and retreat.

The correlations calculated in this study are derived using a simple model and a grid size larger than the area of a single glacier and, so, should be regarded as providing insight and not predictions. In exchange for being able to understand and analyze the results of the system, we have neglected many of the complications that exist in true dynamical glacier systems and mountain climates. We feel confident that our choice in LW50 is adequate, as the North American Regional Reanalysis model

and the 40-yr European Centre for Medium-Range Weather Forecasts (ECMWF) Re-Analysis (ERA-40) grid-spaced data set produced very similar results. However, climate data with a resolution of 0.5°cannot capture the full gamut of climatic effects in mountainous terrain. The unresolved details of small-scale precipitation patterns will not change the results regarding the overall contrast between maritime and continental climates or the general northsouth trends due to the inherent spatial scale of the regional climate patterns. It is likeliest to make a difference in the predicted sensitivities of, and spatial correlations among, the coastal Pacific Northwest glaciers. The lesson from the MM5 results about the importance of knowing small-scale orographic precipitation patterns is one of the key findings of this study.

We also opted to present results in terms of the correlation between glaciers. An alternative would have been to calculate empirical orthogonal functions (EOFs) to find the modes that account for the largest proportion of the variance in glacier advance and retreat. Different treatments for the mass balance are also possible: we could have chosen to use a positive degree-day model [e.g. Braithwaite and Zhang, 2000] or a full surface energy balance model [e.g. Rupper, 2007] to calculate glacier mass balance. The assumption that all precipitation is accumulation over the glacier could be relaxed by including a temperature-dependent threshold for snow. We feel that this would be unlikely to make any important difference in our main results.

We have also made significant assumptions regarding glacial processes. Chief among these assumptions is the neglect of glacier dynamics. However, several studies have shown that the linear model is capable of reproducing reasonable variations in glacier length [e.g. RO; Jóhannesson et al., 1989, Oerlemans, 2005] and, so, is adequate for the purposes of the present study. Glacier geometry is also highly simplified in the linear model. Tangborn et al. [1990] concluded that area distribution of each glacier was the main distinguishing characteristic accounting for difference in mass

balance on two adjacent glaciers in the North Cascade Range of Washington State between 1947 and 1961, highlighting the complexities in small-scale geometric and climatic factors relevant to glaciers.

Finally, we have focused on glaciers for which the connection with temperature and precipitation is clear and well understood. Our framework cannot be directly applied to tropical or tidewater glaciers, glaciers with a history of surging, or large ice caps or ice sheets, where the physics of that connection is more complex. Further work should be performed, understanding not only spatial patterns in glacial correlation but temporal patterns as well. The model can also readily be used to evaluate when and where a climatic trend in glacier length can be detected against the background interannual climatic variability.

	Boulder	**Deming**	**Coleman**	**Easton**	**Rainbow**	**"Typical"**
A_{tot} (km^2)	4.30	5.4	2.1	3.6	2.7	4.0
A_{abl} (km^2)	1.3	1.6	0.64	1.1	0.81	1.2
$\tan\phi$	0.47	0.36	0.47	0.34	0.32	0.4
w (m)	550	450	650	550	300	500
H (m)	50	50	39	51	47	50
τ (yr)	10	9	20	17	13	12
γ	0.90	0.89	0.95	0.94	0.92	0.92
α m ($^\circ$C^{-1})	32	48	17	26	39	77
β (yr)	160	240	85	130	190	160

Table 2.1: Values for geometric parameters that are used in eq. (2.1) for five glaciers on Mount Baker, Washington (RO). For the values shown here an accumulation area ratio, AAR = 0.7, was assumed. Here A_{tot} is the total glacier area (m^2) and A_{abl} the area over which there is net ablation (m^2); μ is the melt-rate factor (a standard value of 0.67 and a range of 0.5 to 0.84 m yr m^{-1} $^\circ$C m^{-1} was used), Γ the atmospheric lapse rate (6.5 $^\circ$C km^{-1}), ϕ the slope of the bed, w the average width of the ablation area, H the uniform height (or thickness) of the glacier, and t is the e-folding relaxation time scale (yr); γ (unitless), a (m $^\circ$C^{-1}), and β (yr) are combinations of the above variables, as prescribed in (1). In the last column values are generally representative of the Mount Baker glaciers and are used for the standard calculations, unless otherwise noted in the text.

Point	**Lat (°N)**	**Lon (°W)**	**Nearest Mountain**	r_P	r_P	R
A	47.3	123.7	Olympus	0.85	0.92	0.39
B	49.8	120.2	Girabaldi	0.75	0.82	2.10
C	53.3	116.8	Columbia Ice Field	0.40	0.26	2.00
D	46.3	119.8	Adams	0.19	0.85	2.40
E	60.3	142.7	Wrangell	-0.37	0.22	0.41

Table 2.2: Key points to correlate with Mount Baker over a variety of glacier geometries: the latitude and longitude of each point are listed, as well as the correlations in precipitation (r_P) and temperature (r_T) and the sensitivity ratio (R). See Fig. 2.8.

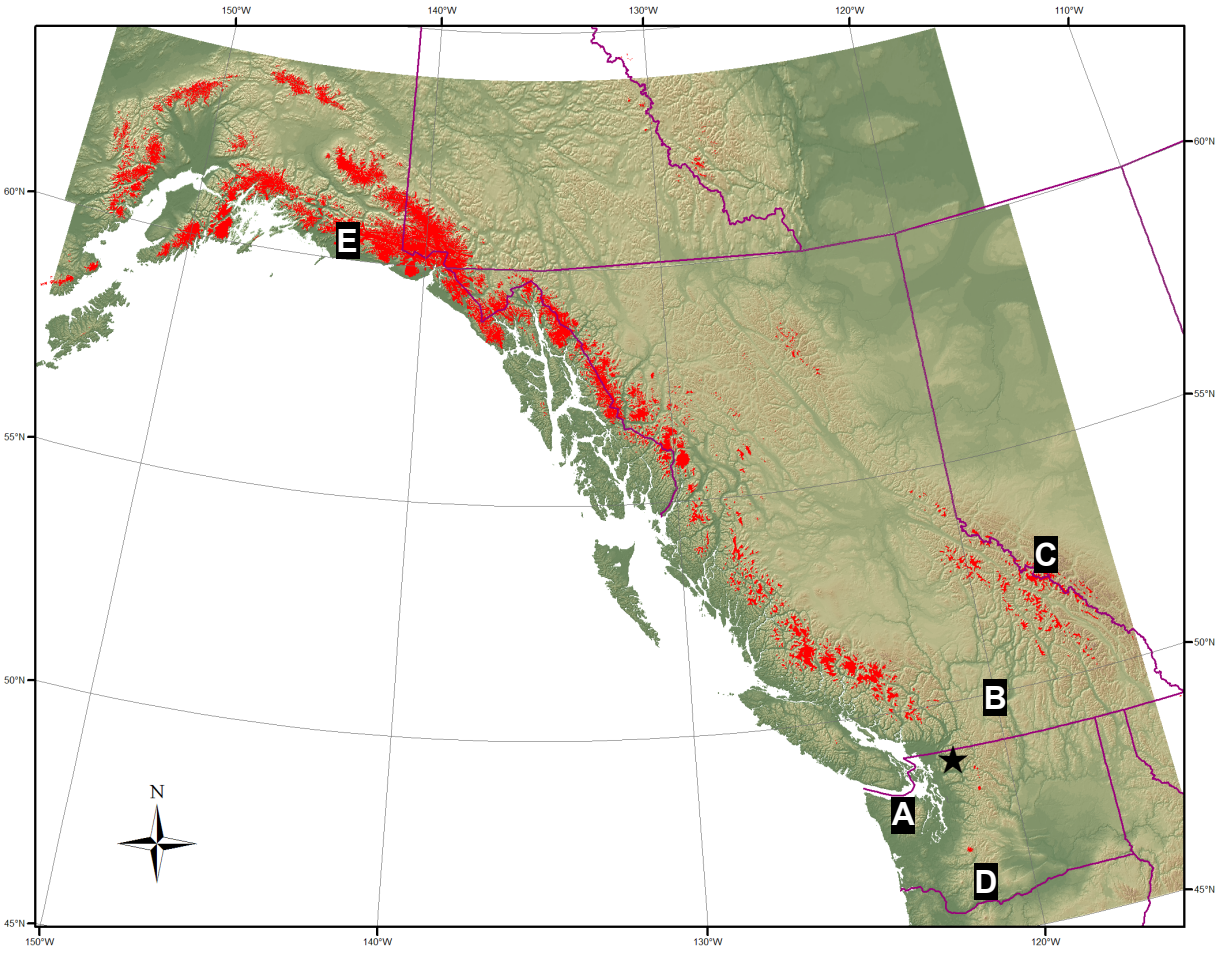

Figure 2.1: Glaciers in the Pacific Northwest, shown in red. Data from the Global Land Ice Monitoring from Space (GLIMS) project (http://www.glims.org/). The location of Mount Baker is denoted with a star. Also indicated in the figure are the locations where glacier model sensitivity is tested. Figure courtesy of Harvey Greenberg.

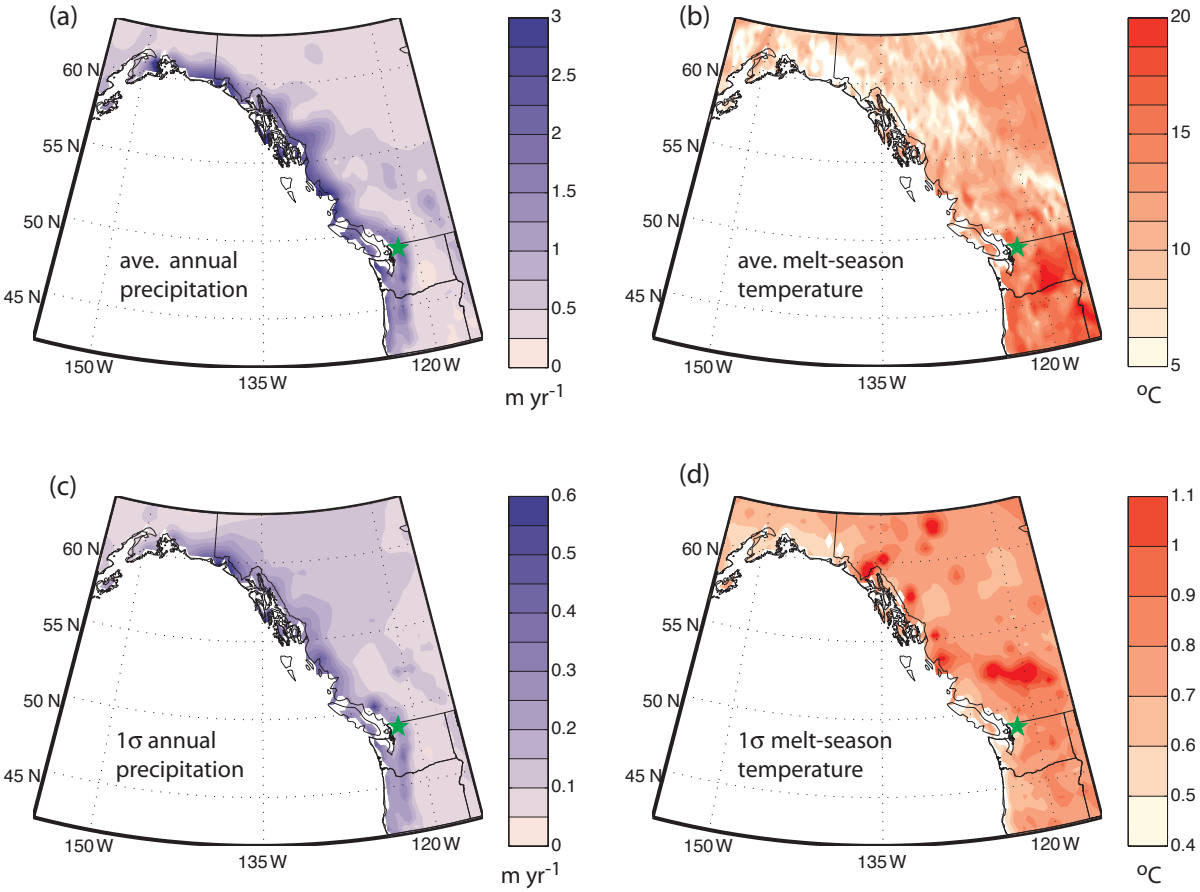

Figure 2.2: Climate mean and variability in the Pacific Northwest from LW50: (a) mean annual precipitation (m yr^{-1}), (b) mean melt-season (JJAS) temperature (°C), and interannual standard deviation of (c) mean annual precipitation (m yr^{-1}), and (d) melt-season temperature, in °C.

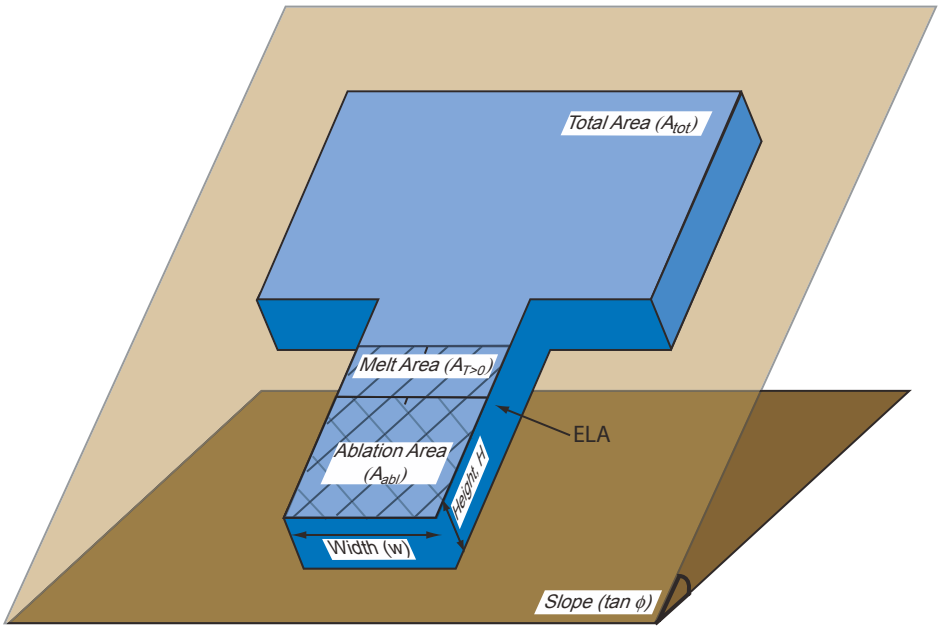

Figure 2.3: Schematic of linear glacier model, based on Jóhannesson et al. [1989]. Precipitation falls over the entire surface of the glacier (A_{tot}). Melt is linearly proportional to the temperature, and a constant lapse rate is assumed. The basal slope is $\tan\phi$. Melt occurs over the lower reaches of the glacier where melt-season temperature exceeds 0 ($A_{T>0}$), and net mass loss occurs over a smaller area where melting exceeds precipitation (A_{abl}). The upper boundary of this latter region is known as the equilibrium line altitude (ELA). The thickness (H) of the glacier and the width of the ablation area (w) remain constant by assumption.

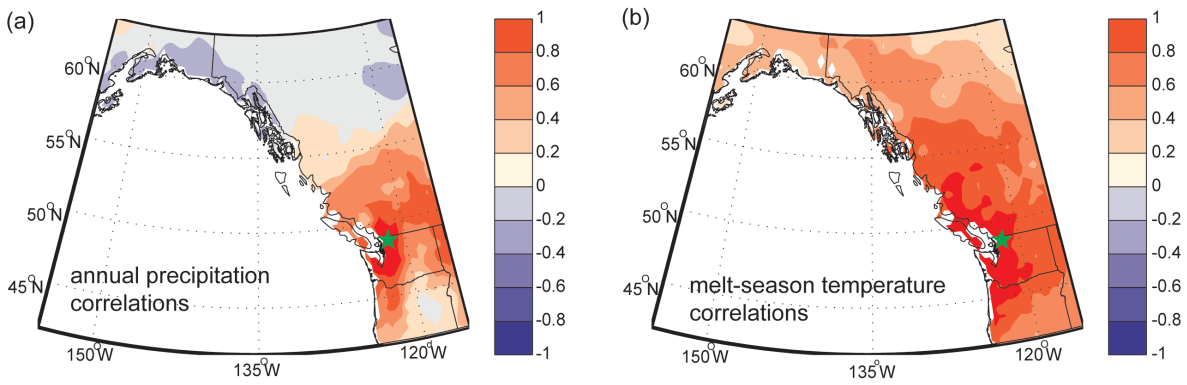

Figure 2.4: Correlation in annual mean precipitation between each grid point and Mount Baker, from LW50 data set; note the dipole of correlations between Alaska and Washington. (b) As in (a), but for the correlation of melt-season temperature; note the widespread correlation of uniform sign over the region. Correlations exceeding about 0.28 would pass a t-test at greater than 95% confidence.

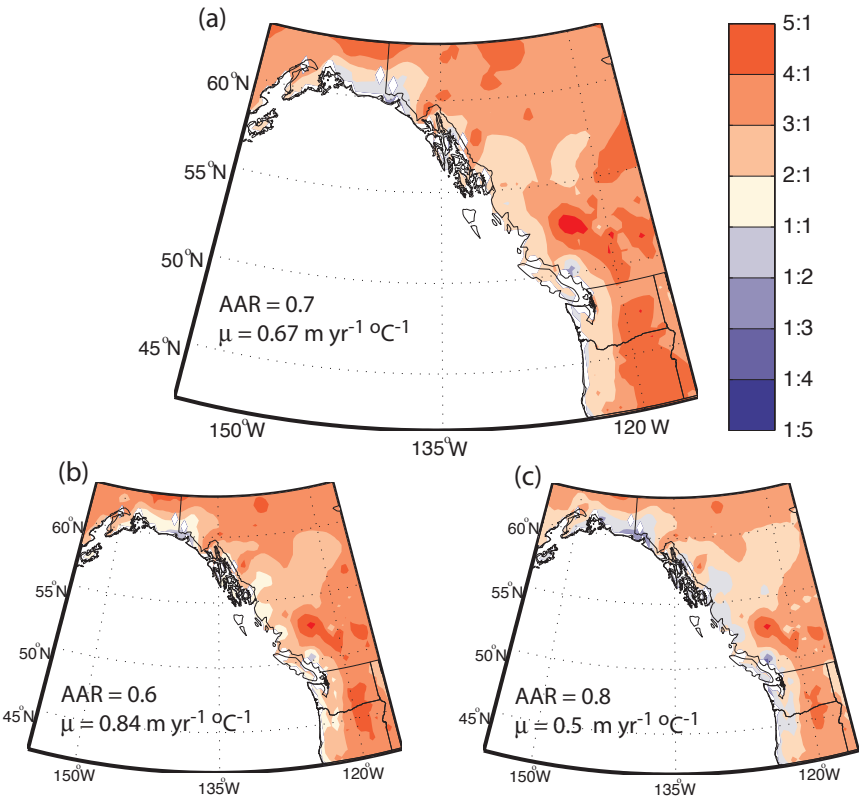

Figure 2.5: Ratio of sensitivities to temperature and precipitation for a typical glacier geometry at each grid point for different choice of model parameters. Warm colors denote temperature sensitivity, while cool colors denote sensitivity to precipitation. (a) The standard parameters, (b) the largest ablation area and melt rate factor, and (c) the smallest values of the ablation area and melt rate factor.

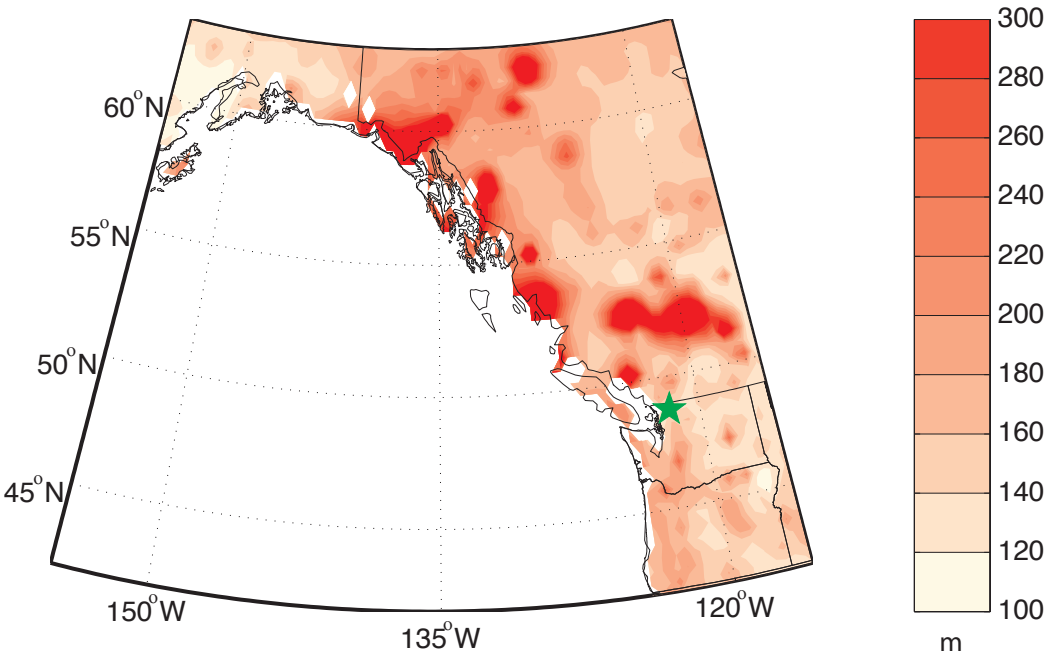

Figure 2.6: Standard deviations of glacier length at each grid point if a typical glacier exists at each grid point, calculated from (17). Large standard deviations in length are driven by large standard deviations in either precipitation or temperature (cf. with Fig. 2.2).

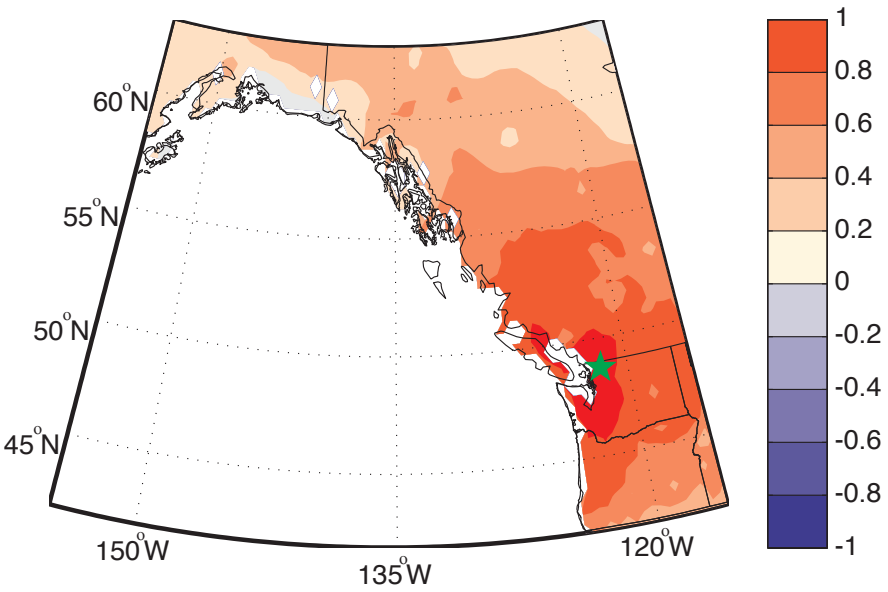

Figure 2.7: Correlations between a typical glacier at each grid point and at Mount Baker, calculated from eq. (2.10) .

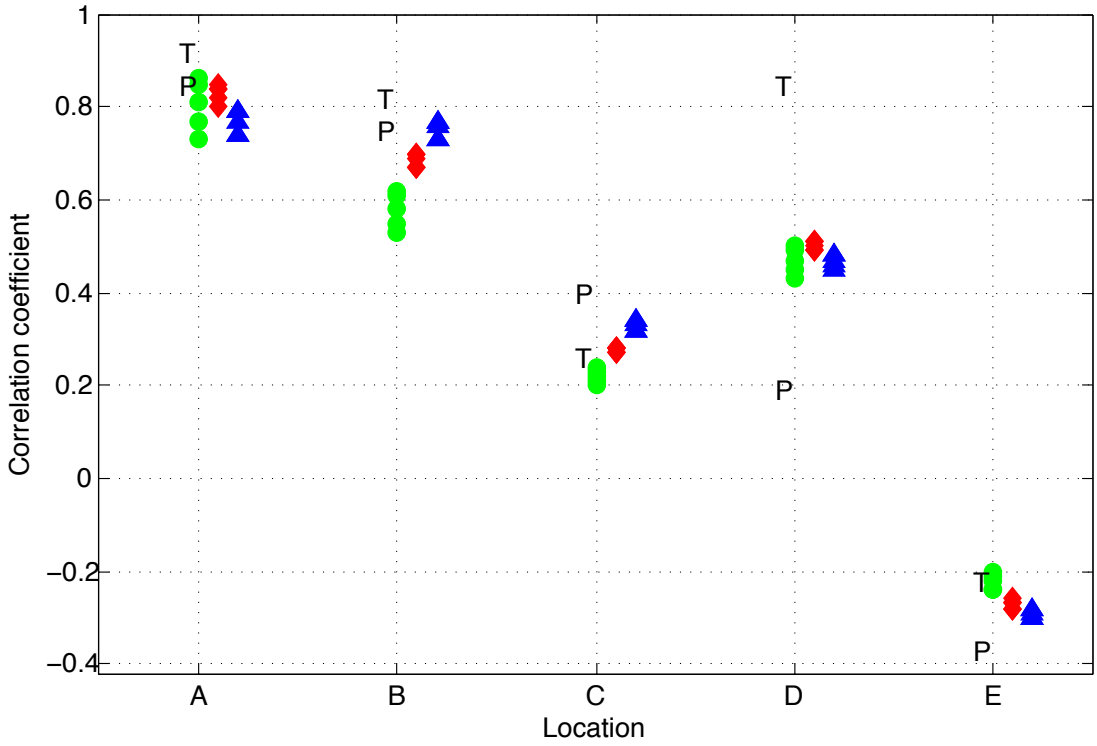

Figure 2.8: Sensitivity test of correlations, at selected locations (see Fig. 1), to varying the glacier geometry and parameters: T and P denote melt-season temperature and annual precipitation correlations between that location point and Mount Baker. Colored symbols represent the correlation of glacier length between that location and Mount Baker, and the range arises from using the five different parameter sets applying to the different Mount Baker glaciers (given in Table 2.1). Finally the different colors mean a different AAR was used: green (AAR = 0.6), red (AAR = 0.7), and blue (AAR = 0.8).

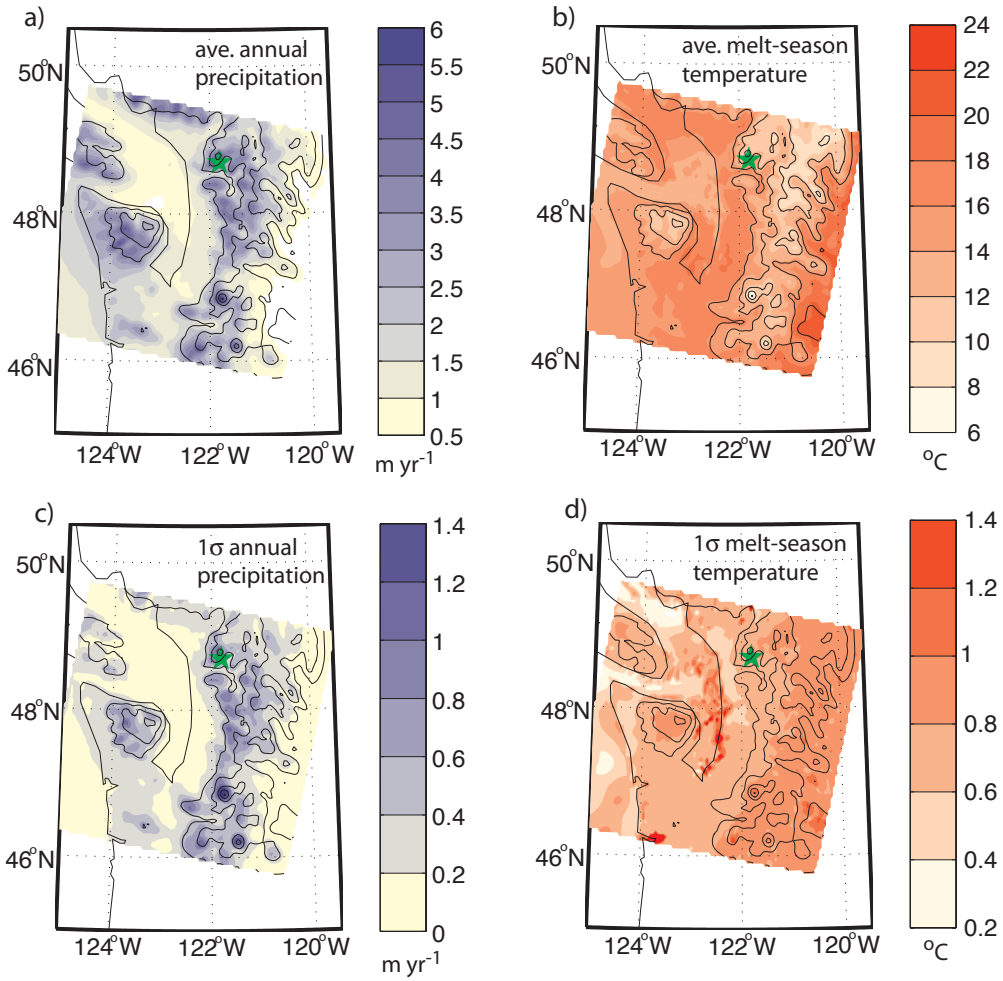

Figure 2.9: Archived output from the MM5 numerical weather prediction for the Pacific Northwest at 4-km scale: (a) mean annual precipitation, (b) mean melt-season temperature, and standard deviation of (c) precipitation and (d) melt-season temperature. Contours of the model surface elevation are also plotted every 500 m; the location of Mount Baker is indicated with a star. Note the small-scale patterns of climate associated with the mountainous terrain, in particular the high rates of orographic precipitation.

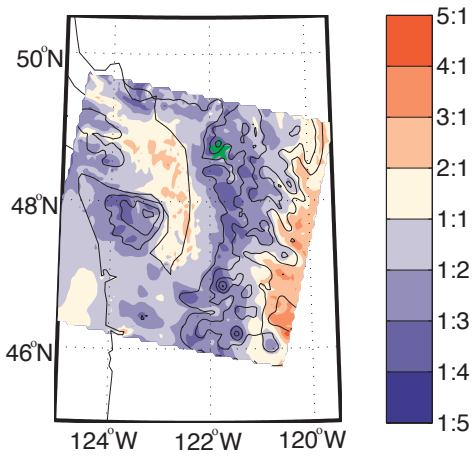

Figure 2.10: Ratio of sensitivities to temperature and precipitation of a glacier length with a typical Mount Bakerlike geometry, calculated at every model grid point from eq. (2.16). Blue indicates a greater sensitivity to precipitation. The mountainous regions of the Olympics and Cascades, where glaciers in the region actually exist, are dominated by sensitivity to variation in the precipitation.

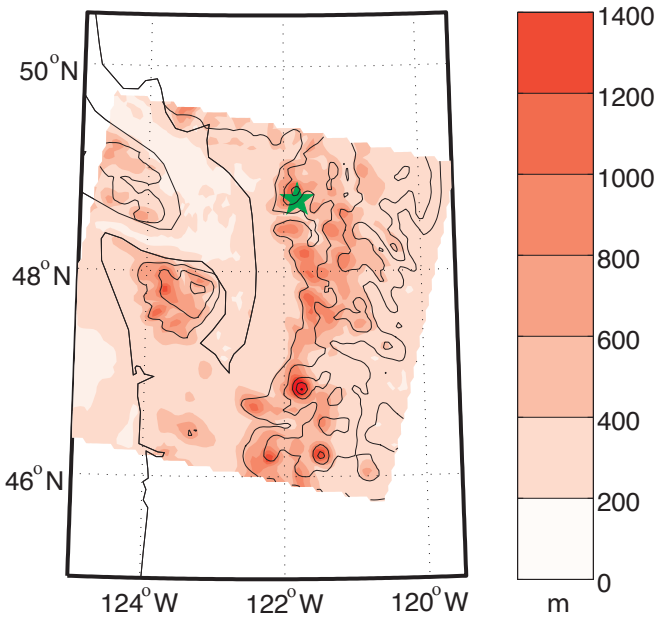

Figure 2.11: The standard deviation of glacier length calculated from eq. (2.17) using the 4-km resolution MM5 output. This fine-resolution scale shows that, in the mountainous regions where glaciers exist, the standard deviation in glacier length is much higher than in lower elevations. The high standard deviations are driven by the high variability in precipitation there.

Chapter 3

GEOMETRIC INFLUENCES ON GLACIER VARIABILITY

3.1 Introduction

As discussed in Chapter 2, mountain glaciers are often cited as indicators of climatic variability and change. They directly integrate changes in snowfall temperature, which drives ice melt. Glaciers dynamically thicken (thin), or advance (retreat) in response to climatic variations. Because evidence for glacier change is often derived from terminal moraine deposition, historical records, or aerial photography, the variations in length are the most straightforward way to track a glacier's health. Nye [1960] described how variations in the lower part of a glacier respond both to the direct effects of snowfall and ice melt, and to the arrival of material from the upper part of the glacier, which can take between 3 and 30 years. Following on this, much work was done to understand what drives the timing and magnitude of variations in glacier length [e.g. Nye, 1961, 1963, Jóhannesson et al., 1989, Oerlemans et al., 1998, Harrison et al., 2001, Weber and Oerlemans, 2003, Roe, 2011, Oerlemans, 2012, Harrison, 2013].

Reichert et al. [2002] and Roe and O'Neal [2009] specifically studied how glacier lengths vary in response to interannual climatic forcing. Their work determined the expected range of glacier variation in response to interannual variations in precipitation and temperature. Variations that exceed the bounds of this range indicate that a glacier is responding to a true climatic shift, rather than a short-term variation in precipitation or temperature. Further, Huybers and Roe [2009] showed that a glacier's latitude and proximity to the ocean correlates with whether these changes

are more sensitive to variations in temperature or precipitation.

Along with the mean state of the climate, the steepness, shape, and makeup of the bed, the size of the catchment area, the width of the tongue, and the elevation of the glacier contribute to determining the mean length and thickness of a glacier. These geometric effects can be large. For example, Kessler et al. [2006] showed that 97% of the disparity between the lengths of glaciers flanking the east and west side of California's Sierra Nevada range during the Last Glacial Maximum is attributed to the topographic asymmetry of the mountains alone. These geometric characteristics will also determine the amplitude and timing of a glacier's response to climatic variations. Oerlemans et al. [1998] concluded that while there is no straightforward relationship between glacier size and fractional change in ice volume, hypsometry plays an important role in determining the variability of a glacier, and that, in general, smaller glaciers fractionally lose more mass. Kuhle [1988] showed that glacier geometry and mass balance both correlate with deviations in the Equilibrium Line Altitude (ELA).

For this work, I use a dynamic flowband model, which incorporates width variations, to compare length variations between glaciers with unique geometric characteristics, as they respond to identical climate forcings. The geometric setting is based on Mount Baker, a glaciated volcanic peak in the Cascade Range of Washington State, USA (Fig. 3.1). The glacier models are forced with randomly generated perturbations in precipitation and temperature, based on the local present-day means and standard deviations. The model is run repeatedly, altering the slope, shape, width, bed roughness, and area for each experiment. The correlation coefficients are calculated for pairs of the resulting glacier-length time series. The main purpose of this work is to determine the geometric parameters that most affect the magnitude of glacier variability and the temporal coherence between pairs of glaciers.

3.2 Mount Baker glaciers

Continuing the work of Roe and O'Neal [2009], Huybers and Roe [2009], and Roe [2011], I have chosen Mount Baker as my study area. Mount Baker is a large stratovolcano, located in the Cascade Mountains of Washington state, U.S.A. (48.7°N, 121.8°W). It is flanked by eight glaciers with a broad range of shapes and sizes, whose history and geometry have been well-documented and studied. The glaciers on Mount Baker have undergone large variations during the Holocene [e.g. Thomas et al., 2000], and a large body of research has been done to understand the general pattern of retreat since the local Little Ice Age [Harper, 1992, 1993, Pelto and Riedel, 2001, Pelto and Hedlund, 2001, ONeal, 2005], and the individual glacier dynamics [e.g. Harrison, 1970].

Harper [1993] discussed the historical variations on Mount Baker. All of the glaciers exhibit a general retreat prior to 1940, an advance after 1940, and a subsequent retreat, though the timing and magnitude of these advance and retreats vary. He observed that Easton and Rainbow Glaciers' responses lag behind the Coleman, and that the total magnitude of Coleman Glacier's response is larger than Easton, and larger than Rainbow with the exception of the initial retreat.

3.2.1 Climate

The present-day climate of the Pacific Northwest is strongly affected by the peaks and valleys of several mountain ranges, giving rise to rich and distinct weather patterns [e.g. Bitz and Battisti, 1999, Minder et al., 2008]. Despite important mountain-scale precipitation patterns, Pelto and Riedel [2001] show that the glacier mass balance throughout the major North Cascadian glaciers is highly correlated, indicating that large-scale climate conditions can explain much of the regional glaciers' mass-balance profiles.

As noted in the previous chapter, the major feature of the region's atmospheric circulation pattern is the Aleutian Low pressure system, which responds to the dominant modes of climate variability in the region (e.g. ENSO [Zhang et al., 1997], the PDO [Mantua and Hare, 2002], and the PNA [Renwick and Wallace, 1996]). Though these modes of variability lend some memory to the climate system, the year-to-year variation in the region is well characterized by the standard deviations from the mean in annual temperature and precipitation. Annual mean precipitation at Diablo Dam near Mount baker is equal to $\mu_P = 1.89$ m yr^{-1}, with a standard deviation of $\sigma_P = 0.36$ m yr^{-1}. The values for temperature are $\mu_T = 16.8$ °C and $\sigma_T = 0.78$ °C. I assume a steady atmospheric lapse rate of -6.5 °C km^{-1}, and relate the annual melt rate to temperature through an empirical melt factor, μ, which is equal to 0.65 m yr^{-1} °C^{-1}.

3.2.2 Geometry

I model three of Mount Baker's glaciers, chosen for their distinct size, shape, and bed slope (see Fig. 3.1 and Table 3.1, from Harper [1992], Roe and O'Neal [2009]). Easton Glacier is mid-sized, with an accumulation area that is only slightly wider than its ablation area, which has a characteristic width[1] of 420 m. It rests on a bed with a slope of ∼18°, with a modern length of ∼4.2 km, and area of 3.3 km^2. Though its bedslope is similar to that of Easton Glacier, Rainbow Glacier is smaller, its area covering ∼ 2.1 km^2 over a length of 3.2 km. Rainbow Glacier's area widens near the middle of its present-day length, and tapers in the ablation zone, where its characteristic width is 315 m. Coleman-Roosevelt Glacier (heretofore referred to as Coleman Glacier) has a similar length to Easton (4.9 km), but has a much wider catchment zone, and therefore a much larger area (10.6 km^2). It rests on a slope of ∼25°, which is steeper

[1] i.e. average width of the ablation area

than either Rainbow or Easton Glacier, and its characteristic ablation width is 630 m.

This work does not aim to capture the true behavior of a specific set of glaciers, but rather to gain insight into the nature of a general glacier's response. I therefore approximate each glacier's footprint as symmetric around a flowline, and assume a linearly sloping bed. When the modeled glaciers grow beyond their present-day position, the ice is directed down a rectangular channel that is a continuation of the present-day glacier tongue.

3.2.3 Altering the glacier geometry

To isolate the geometric factors that have the strongest influence on decorrelating neighboring glaciers, I use the model described in the following section to capture the behavior of Easton, Coleman, and Rainbow Glaciers. I then alter a single geometric parameter for each of these glaciers, and run the new glacier to steady state. The length of the domain, and therefore the baseline $\bar{T}$ at the end of the domain is also changed, so that the altered glacier has the same steady-state length as its original counterpart. The glacier configurations are as follows:

- *Original Glaciers*: Easton (E_{orig}), Rainbow (R_{orig}), and Coleman (C_{orig}), Glaciers are the baseline glacier models, which capture the thickness, and length profile of the present-day glaciers on Mount Baker (Fig. 3.5A, E, and I), using their width distribution. I assume a planar bed, both because bed geometry is not readily available, and for comparative simplicity. The map view of each of these glaciers, from Fig. 3.1 is also shown in Fig. 3.5D, F, and J, for Easton, Rainbow, and Coleman glaciers, respectively.

- *Width*: Each of the glacier's width variations are removed, so the glacier is described by a flowline of uniform width. These experiments are referred to as

E_w, R_w, and C_w, to denote an Easton, Rainbow, and Coleman Glacier with an unchanging width. The bed geometry remains as shown in Fig. 3.5A, E, and I (glacier profiles not shown).

- *Slope*: Easton and Rainbow Glaciers are set to a 25° slope, which is Coleman's original slope (E_{25} and R_{25}, respectively). Coleman glacier, likewise, is set to Rainbow and Easton's 18° slope (C_{18}). The width profile remains as in Fig. 3.5D, F, and J (glacier profiles not shown).

- *Easton Area*: The aspect ratio of Easton Glacier is preserved, but the length is increased or decreased by 50% (E_{large} and E_{small}). See Fig. 3.5, panels G, H, K, and L.

- *Bed Shape*: The cross-sectional shape of Easton Glacier's bed slope is altered to reflect a parabolic divot into the longitudinal valley profile, similar to those seen in nature [Anderson et al., 2006] (E_{curve}, Fig. 3.5B). Bed roughness is added, by imposing a sine wave with an amplitude of 5 m on a linear bed ($E_{5sin(x)}$ (not shown)) and another with an amplitude of 10, and a wider spacing ($E_{10sin(5x)}$, Fig. 3.5C). These profiles have the same width distribution with the original Easton Glacier profile (Fig. 3.5D).

3.3 Glacier model

Glaciers are deformable bodies that can be described by the physical laws of conservation and thermodynamics. Glacier models span many levels of complexity, from analytical steady-state profiles to full 3D Navier-Stokes simulations. For this work, I use a flow-band finite-volume model, which responds to perturbations in melt-season temperature and annual mean precipitation. Leysinger-Vieli and Gudmundsson [2004] compared a two-dimensional numerical model which solve to full equations for velocity and stress fields to a shallow-ice model, and show that there is no significant difference

in advance or retreat rates between the two. Further, they found only a slight change in steady-state lengths. I therefore proceed with using a shallow-ice approximation (SIA) model [Hutter et al., 1981, Hutter, 1983].

The glacier is assumed to have an accumulation area with a fixed size and shape. Any loss or gain of mass is realized either in the thickness profile of the glacier or at the glacier's tongue, advancing down slope through a rectangular channel. The length variations are departures from an equilibrium steady-state value, and the length and profile thickness anomalies are direct responses to anomalies in melt and precipitation alone–the effects of wind, redistribution and refreezing of meltwater, and sublimation are not taken into account.

The model solves the continuity equation using finite-volume methods [Patankar, 1980]. Assuming constant ice density, the glacier's thickness evolution is described using a standard differential equation for conservation of mass:

$$\frac{\partial H}{\partial t} = -\frac{\partial q}{\partial x} + \dot{b}. \tag{3.1}$$

$H(x,t)$ is the thickness of the ice, where t is time, x is the longitudinal distance from the head of the glacier, and $\dot{b}(x,t)$ is the accumulation/ablation rate, written in terms of precipitation (P) and melt, which is a function of temperature (T). The flux of ice ($q(x,t)$) through each control volume in the glacier model is defined by the depth-averaged velocity, $\bar{u}(x,t)$, that the ice flows through a cross-sectional area of the glacier's width times height ($w(x) \times H(x,t)$).

$$q(x,t) = w(x)\bar{u}(x,t)H(x,t). \tag{3.2}$$

The total velocity is the sum of the velocity due to the internal deformation of the ice (u_d), and the sliding velocity (u_s). To determine u_d, the SIA assumes that longitudinal stresses can be ignored, and that all stress is due to basal shearing stress.

The SIA relates the vertical gradient in velocity in the bed-parallel vertical profile to the to the driving shear stress (τ_d) raised to some power n, an empirical value, chosen to be 3, as per convention. The driving stress is a function of both the ice's thickness and the surface slope of the ice profile: $\tau_d = -\rho g H \frac{dh}{dx}$, where ρ is the density of ice, g is the acceleration due to gravity, and $h(x,t)$ is the ice-elevation ($H(x,t)$ plus bed elevation, z_b). The depth-averaged horizontal velocity in the ice is then:

$$\bar{u} = u_s + u_d = u_s + \frac{2}{n+2} A H |\tau_d|^{n-1} \tau_d, \tag{3.3}$$

where A is a function of ice temperature, and describes the ice's softness. For this work A is assumed to be constant.

The sliding speed is derived from a Weertman-style law, where the basal water pressure is assumed to be a function of the ice load above. Following Oerlemans [2001]:

$$u_s = \frac{f_s \tau_d^m}{H}, \tag{3.4}$$

where f_s is a constant, chosen to approximate observed present-day glacier thicknesses. The exponent m, like its deformational counterpart n, is chosen to be 3 [after Oerlemans, 2001].

When Eq. (3.1) is rewritten as a diffusion equation, it can be solved for using finite-volume methods:

$$\frac{dH}{dt} = -\frac{\partial}{\partial x}\left(\Gamma \frac{\partial h}{\partial x}\right) + \dot{b}, \tag{3.5}$$

where $\Gamma = q(x,t)(\frac{\partial h}{\partial x})^{-1}$.

Γ is not a constant, but is itself a function of the ice thickness. Therefore, this model solves for the ice surface elevation implicitly, and the length of the glacier is tracked at each time step.

3.4 Model application and results

Because this work aims to characterize the correlation between glaciers as they experience interannual climate variability, rather than the true history of the glaciers, no trends are applied to the climate forcings. Instead, the glaciers are forced with 1000-year stochastic time series of precipitation and temperature, with standard deviations reflecting those from the historical climate records described above. The variations in the precipitation and temperature time series are shown in Fig. 3.3A & B. The precipitation is assumed to be uniform over the length of the glacier, and all precipitation falls as snow. This is a reasonable approximation, since, as discussed in Chapter 2, about 80% of the Pacific Northwest's regional precipitation occurs during the months of October-March, when high-elevation temperature is below freezing. The temperature profile itself decreases linearly with height, and so varies along the glacier's length and between glaciers.

These forcings are applied to each of the model configurations described in Section 3.2.3, and the modeled length variations are recorded over time. The standard deviation of each glacier terminus position (σ_L), and the correlation coefficient (r) between pairs of glaciers are computed (see Table 3.2).

3.4.1 Original Glaciers

The time series for C_{orig}, E_{orig} and R_{orig} are shown in Fig. 3.3C. Though the glaciers are responding to the same climate forcing, the Coleman Glacier varies with a higher amplitude and with higher frequency than the Easton or Rainbow glaciers ($\sigma_{L,C} = 269$ m; $\sigma_{L,E} = 188$ m; $\sigma_{L,R} = 230$ m). The r-value of the time series of C_{orig} and E_{orig} is 0.79, while E_{orig} and R_{orig} are correlated at 0.87. The time series of C_{orig} and R_{orig} have a correlation coefficient of 0.54.

3.4.2 Width

When the width variations of the glaciers are removed, the correlation coefficients increase: the correlation between C_w and E_w is 0.82, E_w and R_w is 0.97, and C_w and R_w is 0.72. The correlation between each of these uniform-flowband model runs with their corresponding original glacier model runs is above $r = 0.9$, (see the grey lines in Fig. 3.5A, B, and C) although the pair of Rainbow Glacier models has the lowest r, indicating that its irregular hypsometry can strongly effect its pattern of advance and retreat. Without width variations, less snow is fluxed through the system, and so each glacier's standard deviations are all substantially smaller than the standard deviations of the original models ($\sigma_{L,C} = 103$ m $\sigma_{L,E} = 111$ m, $\sigma_{L,R} = 107$ m).

3.4.3 Slope

When Coleman Glacier is set to 18° (C_{18}), the same angle as E_{orig}, the correlation between the two is nearly perfect: $r = 0.99$. The correlation between C_{18} and R_{orig} is also improved, with $r = 0.85$. Likewise, the correlation between C_{orig} and the higher-sloped E_{25} and R_{25} is also very high: $r = 0.99$. Conversely, the correlation between the original glaciers and their new-slope counterparts is relatively low: for Coleman Glacier, $r_{18,orig} = 0.78$; Easton Glacier, $r_{25,orig} = 0.83$; and Rainbow Glacier, $r_{25,orig} = 0.82$ (see the green lines in Fig. 3.5A, B, & C). This indicates that bedslope has a very strong effect on the timing of the glacier advance and retreat. The smallest r, for the Rainbow Glacier pair, is still high compared to the correlation between C_{orig} and R_{orig}. The variations of C_{18} are larger than the original model, and the variations of E_{25} and R_{25} are smaller than the original models. ($\sigma_{L,C} = 310$ m $\sigma_{L,E} = 167$ m, $\sigma_{L,R} = 203$ m).

3.4.4 Easton Area

The time series of E_{orig}, $E_{smaller}$, and E_{larger} are shown in Fig. 3.5D. It is apparent that the amplitude of the variation for all three models is comparable ($\sigma_{L,larger} = 206$ m, $\sigma_{L,smaller} = 160$ m). This may not be intuitive, given that the length of E_{larger} is twice as long and that and ~ 6 times larger in area than E_{orig}, and that $E_{smaller}$ is half the length and ~ 2.5 times smaller in area than E_{orig}. The correlations between the similarly shaped glaciers are comparable to those of the correlations between Easton Glacier and Rainbow or Coleman Glaciers. E_{orig} and E_{small} have a correlation of $r = 0.86$, and E_{orig} and E_{large} have a correlation of $r = 0.87$. The correlation between E_{small} and E_{large} is 0.65. The larger glacier, which accumulates more snow, also loses ice more readily; the converse is true for the smaller glacier. Therefore hypsometrically similar glacier distributions may yield a similar amplitude of variability, but will respond with a different time scale of variability. Further, the fractional variations in length are much larger for the smaller glacier.

3.4.5 Bed Roughness

Introducing Easton Glacier to a parabolic bed (E_{curve}), or a sinusoidally roughened bed ($E_{5sin(x)}$, $E_{10sin(5x)}$) does little to changes the amplitude of the variations ($\sigma_{L,curve} =$ 179m, $\sigma_{L,5sin(x)} = 188$ m, $\sigma_{L,10sin(5x)} = 186$ m). The correlation between each of these glaciers and E_{orig} is $r = 0.99$

3.5 Discussion and summary

The experiments described above explore the sensitivity of glacier response to each of these factors. Bed slope, hypsometry, and the overall size of the glacier all affect the timing of glacier advance and retreat. My model experiments are consistent with the observations of Harper [1993], showing a lagged response of Easton and Rainbow Glaciers behind Coleman Glacier, and a larger magnitude of variability from Coleman

in comparison to the other two glaciers.

For each experiment, larger glaciers respond on shorter timescales than smaller glaciers. The linear formula for τ from Roe and O'Neal [2009], shows that the timescale of response is inversely proportional to the ablation area of the glacier. The Coleman Glacier, and its altered counterparts, indeed have larger ablation areas than the Easton or Rainbow glaciers, allowing warmer temperatures to melt more ice away, and more snowfall to be caught when the precipitation increases. This reasoning also explains why removing width variations increases the glacier correlations – for the non-varying width experiments, only variations in ablation-area *length* affect the net accumulation or melt, whereas in the original experiments, differences in width alter the amount of ice collected or removed from the glacier. Similarly, the largest glaciers, E_{large} and the suite of Coleman-like glaciers, all have high correlation coefficients, even when their values for σ_L differ from one another.

Glaciers with the same bed slope tend to have high correlation coefficients. This is unsurprising, because again, Roe and O'Neal [2009] showed that the timescale is inversely proportional to the tangent of the bed slope. A notable exception to this general rule is the correlation between E_{large} and R_{orig}, which both lie on 18°slopes, but are have an r-value of 0.65. This relatively low correlation shows how the overall size and hypsometry of the glaciers also affect the timescale of response.

There are some r-values that are surprisingly high, because the glaciers being compared appear to have very few common characteristics. For example, R_{25} and C_{18} have a near-perfect correlation. The slope and ablation area appear to balance one another, in this case. Similarly, R_{25} has high correlations with the C_w and E_w, which reinforces the idea that the hypsometry of the Rainbow glacier strongly affects its timescale of response.

To look for evidence of shorter timescale variability, researchers should look to records of glaciers on steeper slopes, or glaciers with large ablation areas. It is important to note that comparable magnitudes of variability is not predictive of the correlation of advance and retreat of the glaciers.

Long records of such detailed temporal or spatial information about glacier length variations are rare. However, this work complements Chapter 2, allowing us to freely explore the effect of geometric differences in glacier length agreement, informing the observations of regional glacier advance and retreat that do exist. When comparing the advance or retreat of glaciers, one must take into account these best-case length correlations before interpreting a regional climatic signal. The temperature or precipitation time series will be uniquely integrated by glaciers with their own array of geometric parameters. Detecting a coherent regional climatic signal requires this preliminary understanding of how the glacier dynamics filter the climate.

	Coleman	**Easton**	**Rainbow**	*units*
A_{total}	10.6	3.3	2.1	km^2
A_{abl}	4.0	1.4	1.1	km^2
L	4.89	4.35	3.0	km
θ	25	18.5	18.5	°C
W_{char}	630	420	315	m
H_{char}	43	49	39	m
τ_{char}	3.5	10	8	yr

Table 3.1: Default geometric inputs to glacier models. Length and area are based on values for the 1990's [Harper, 1992]. The estimates for τ come from the linear formula in Roe and O'Neal [2009].

	$\mathbf{C_{orig}}$	$\mathbf{E_{orig}}$	$\mathbf{R_{orig}}$	$\mathbf{C_{18}}$	$\mathbf{E_{25}}$	$\mathbf{R_{25}}$	$\mathbf{C_w}$	$\mathbf{E_w}$	$\mathbf{R_w}$	$\mathbf{E_{large}}$	$\mathbf{E_{small}}$
$\mathbf{C_{orig}}$	1.0	–	–	–	–	–	–	–	–	–	–
$\mathbf{E_{orig}}$	0.79	1.0	–	–	–	–	–	–	–	–	–
$\mathbf{R_{orig}}$	0.54	0.87	1.0	–	–	–	–	–	–	–	–
$\mathbf{C_{18}}$	0.78	0.99	0.85	1.0	–	–	–	–	–	–	–
$\mathbf{E_{25}}$	0.99	0.83	0.58	0.82	1.0	–	–	–	–	–	–
$\mathbf{R_{25}}$	0.99	0.77	0.82	0.99	0.87	1.0	–	–	–	–	–
$\mathbf{C_w}$	0.97	0.73	0.52	0.71	0.96	0.77	1.0	–	–	–	–
$\mathbf{E_w}$	0.88	0.98	0.81	0.98	0.91	0.99	0.82	1.0	–	–	–
$\mathbf{R_w}$	0.77	0.99	0.91	0.99	0.81	0.98	0.72	0.97	1.0	–	–
$\mathbf{E_{large}}$	0.98	0.87	0.65	0.86	0.99	0.89	0.93	0.85	–	1.0	–
$\mathbf{E_{small}}$	0.55	0.86	0.99	0.84	0.59	0.81	0.53	0.81	0.90	0.65	1.0
σ_L (m)	269	188	230	310	167	203	103	111	107	206	160

Table 3.2: Correlations between glacier lengths. All runs are done with the same random 1000 year precipitation and temperature time series. **C** = Coleman Glacier; **E** = Easton Glacier; **R** = Rainbow Glacier; **orig** = original model configuration; **w** = no width variations; **18** and **25** refer to the altered bed slope; **large** and **small** refer to glaciers that have the same shape as Easton Glacier, but are double and half the length, respectively. σ_L is the standard deviation in glacier length.

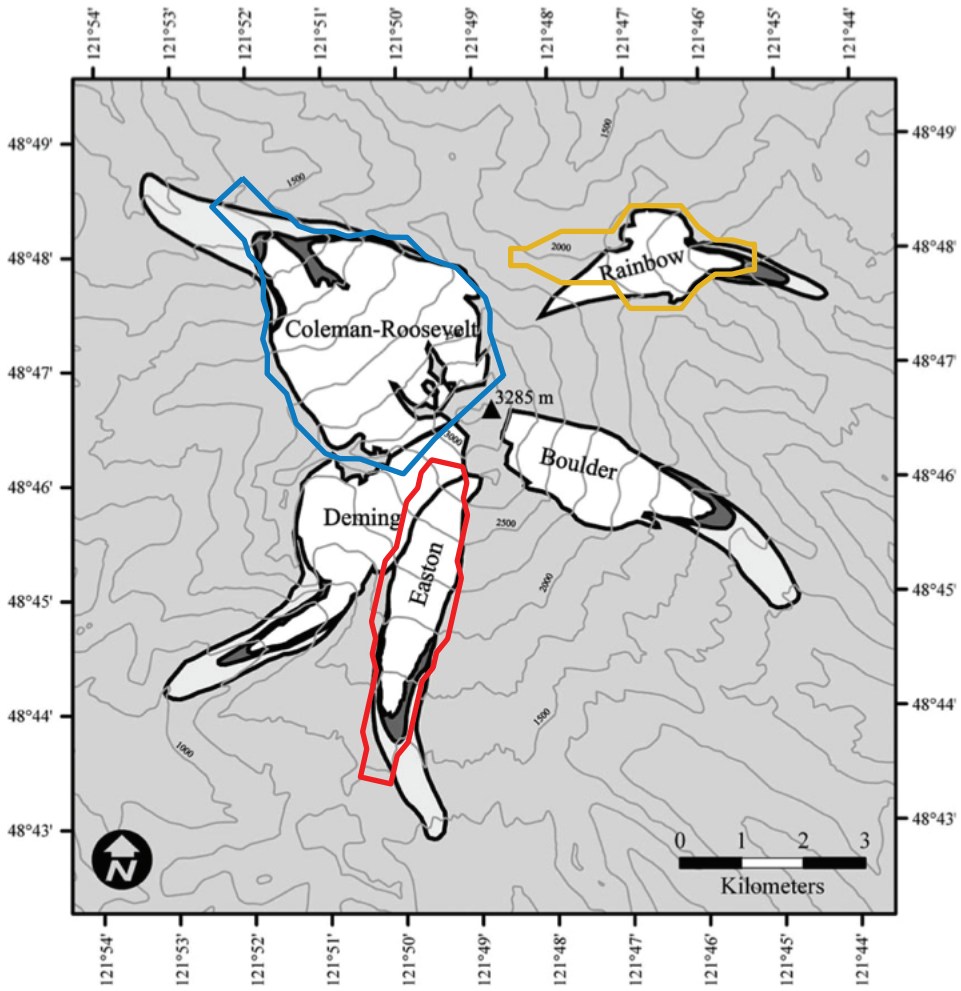

Figure 3.1: Major glaciers of Mount Baker, Washington State, U.S.A. Figure is modified from Roe and O'Neal [2009]. The outlines represent the width variation used in the glacier modelling. Advances beyond the present-day length of the glacier follow a rectangular channel that is equal to the width at the end of the ablation area (referred to in the text as the characteristic width).

Figure 3.2: Glacier and bed profiles, as well as map view widths for several of the model experiments. **A**: Original Easton Glacier. **B**: Easton Glacier with a linear bedslope that has been modified with a sine wave, with amplitude = 10 and phase =5x. **C**: Parabolic bed with Easton Glacier. **D**. Map view of Easton glacier (as in Fig. 3.1, and applied to glaciers in panels A-C. **E**: Original Rainbow Glacier. **F**: Map view of Rainbow glacier (as in Fig. 3.1, and applied to the glacier in panel E. **G** Smaller version of Easton glacier, with half the length, and a proportionally smaller width. **H** Map view of glacier in panel G. **I** Original Coleman Glacier **J** Map view of Coleman glacier (as in Fig. 3.1, and applied to the glacier in panel J. **K** Larger version of Easton glacier, with half the length, and a proportionally larger width. **L** Map view of glacier in panel K.

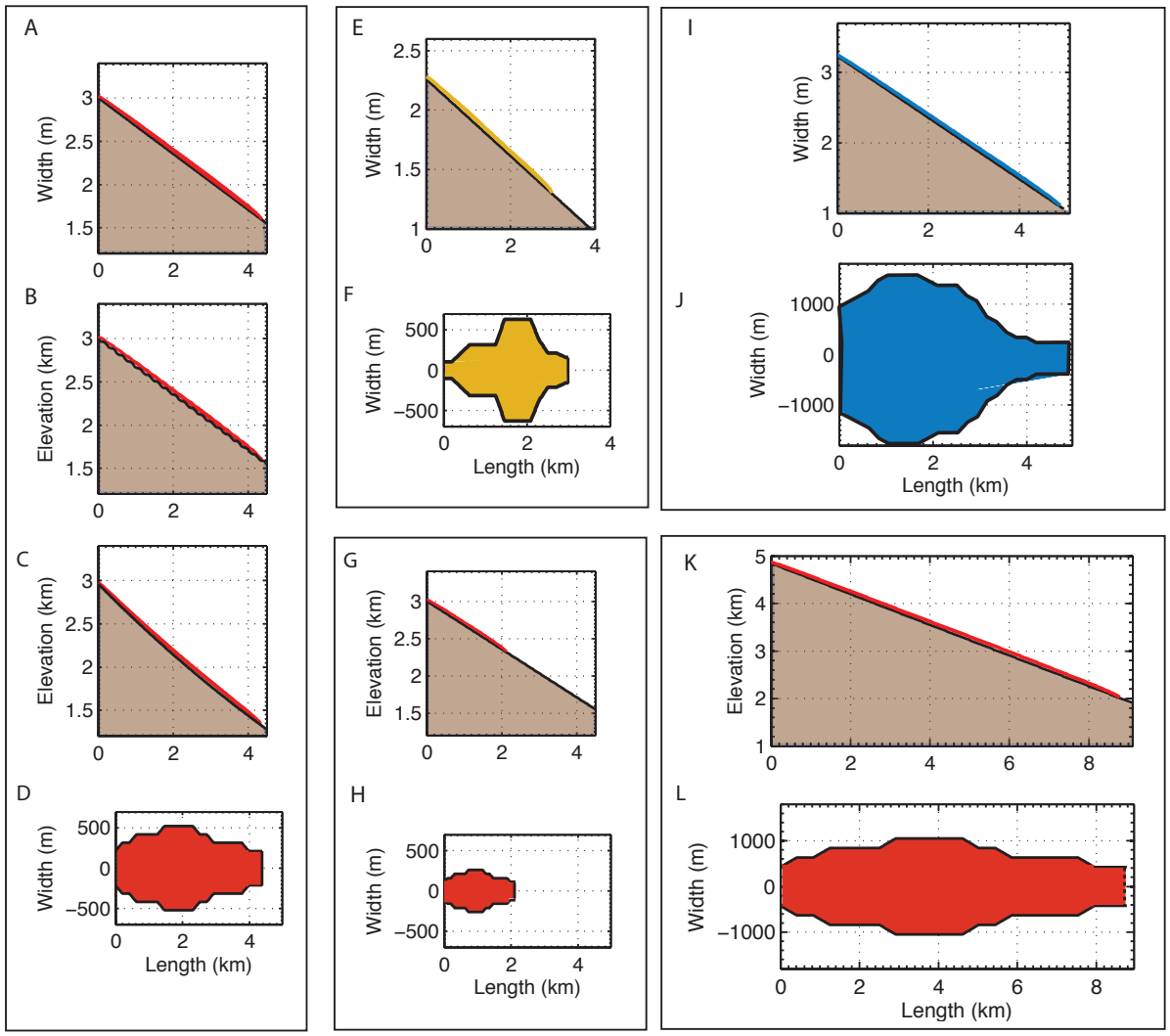
A
Width (m)
B
Elevation (km)
C
Elevation (km)
D
Width (m)
Length (km)
E
Width (m)
F
Width (m)
Length (km)
G
Elevation (km)
H
Width (m)
Length (km)
I
Width (m)
J
Width (m)
Length (km)
K
Elevation (km)
L
Width (m)
Length (km)

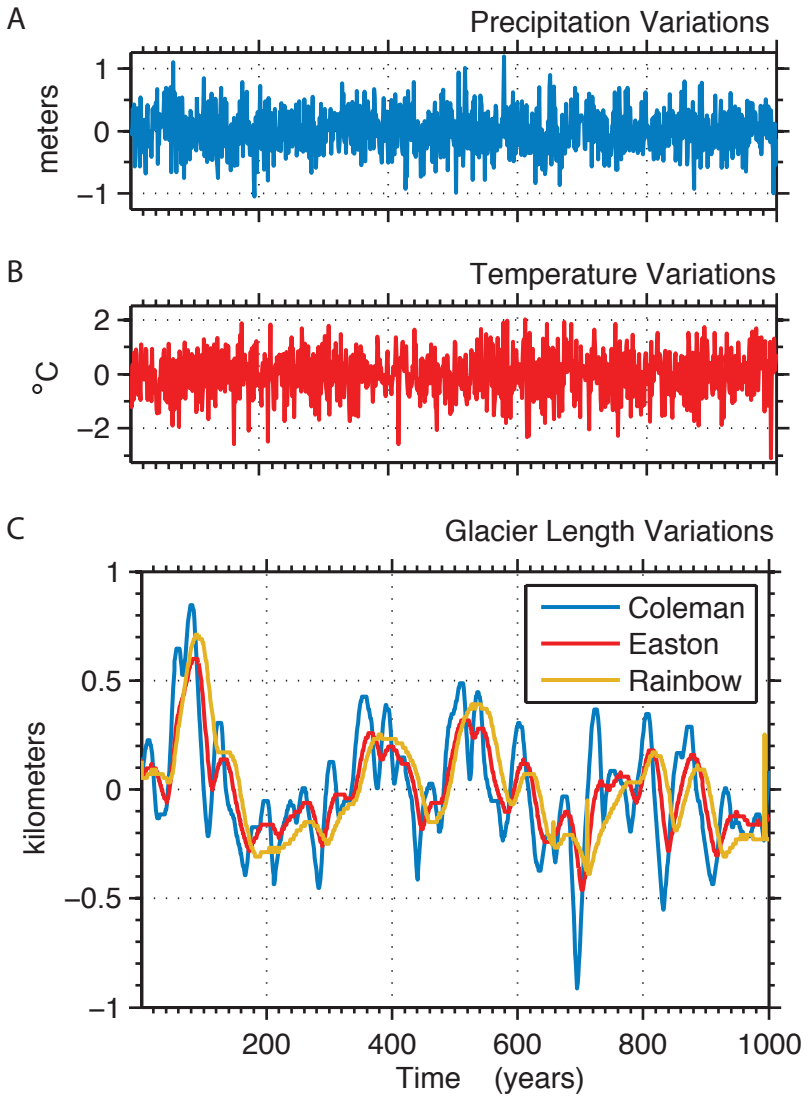

Figure 3.3: The top two panels show 1000 years of random precipitation and temperature variations, applied to the glacier models. $\sigma_P = 0.36$m, $\sigma_T = 0.78$ °C, in agreement with historical records from the nearby Diablo Dam weather station. The bottom panel shows the glaciers' length variations in response to the precipitation and temperature forcings. Note that the frequency of glacier response is much lower than that of the climate forcings.

Figure 3.4: **A, B, C:** The original, altered slope, and uniform-flowband time series of glacier length variability for the Coleman, Easton, and Rainbow Glaciers, respectively. **D**: The glacier length response for the original Easton Glacier, as well as the smaller and larger versions of the glacier.

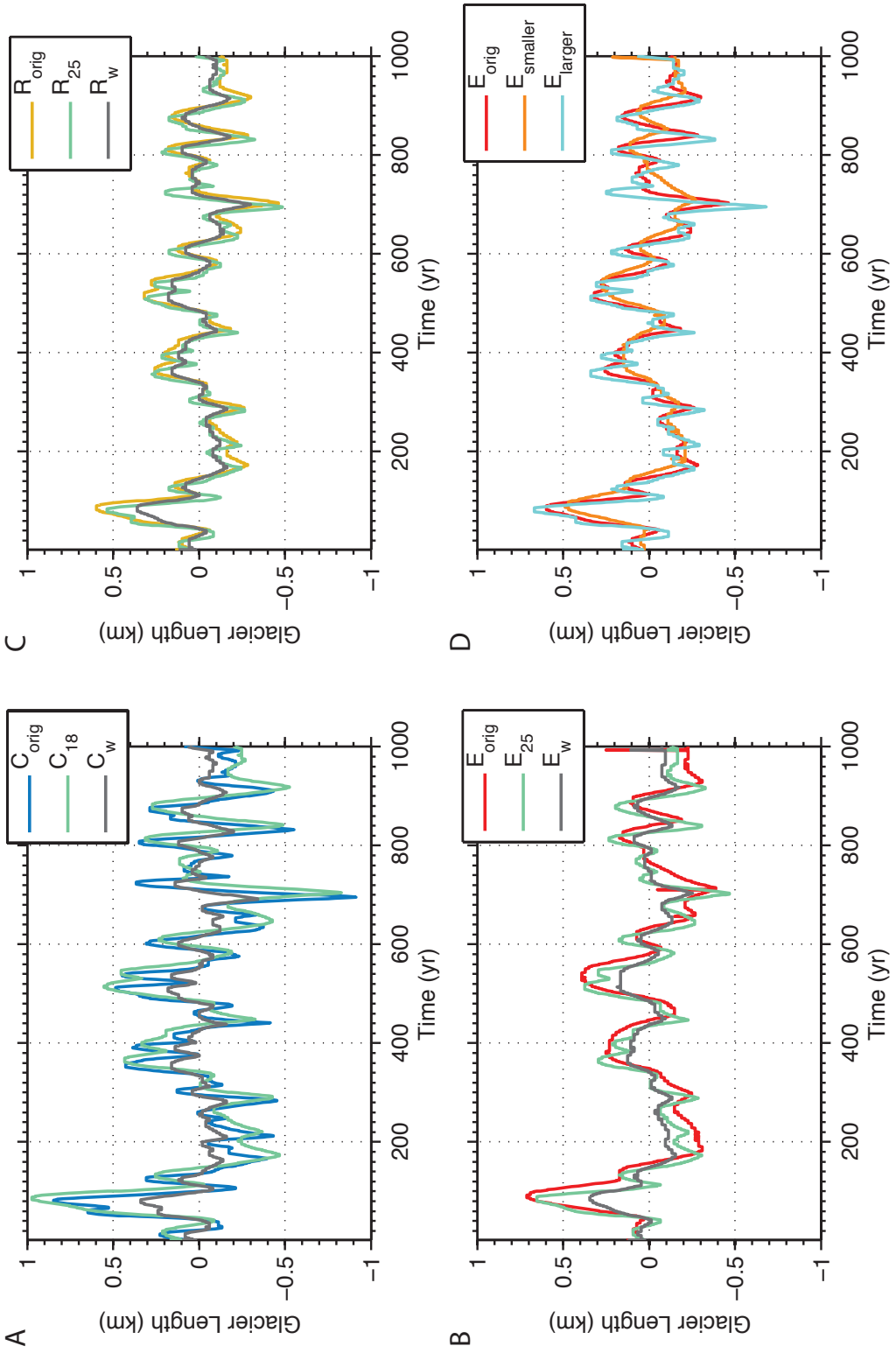
A
B
C
D
Glacier Length (km)
Time (yr)
1
0.5
0
−0.5
−1
200
400
600
800
1000
C_{orig}
C_{18}
C_w
E_{orig}
E_{25}
E_w
R_{orig}
R_{25}
R_w
E_{orig}
$E_{smaller}$
E_{larger}

Chapter 4

LAKE LEVEL CHANGES IN RESPONSE TO INTERANNUAL CLIMATE VARIABILITY

Chapter 4, in full, is currently being prepared for publication as "Lake Level Changes in Response to Interannual Climate Variability" authored by K. Huybers, S. Rupper, and G. H. Roe. The dissertation author was the primary investigator and author of this paper.

4.1 Introduction

Lakes are important archives of climate history, responding sensitively to variations in evaporation and precipitation. A lake integrates climatic information over its entire catchment area, reflecting regional climate signals with a simple volumetric response. Langbein [1961] noted that closed-basin lakes, which are found in semi-arid regions and lack drainage outlets, fluctuate more than open lakes, because variations in the inflow can only be compensated by a change in the lake's surface area. Therefore, closed lakes are particularly sensitive to climate fluctuations, and have been the subject of many paleoclimate studies [Street-Perrott and Harrison, 1985].

The integrative nature of lakes also complicates the interpretation of a region's climatic history. A lake proxy record does not distinguish between an increase in precipitation and a decrease in evaporation. Moreover, lakes act as low-pass temporal filters on the climate. For example, if a lake that is initially in steady state experiences a spike in precipitation, its level rises and spatial extent increases. With a larger surface area, the net evaporation also increases, and the lake gradually low-

ers and returns to its original size. The size and shape of the lake, and the mean climatic state determine the time it takes to return to equilibrium. This delayed and smoothed response to a climate signal is a hallmark of other geophysical systems with memory such as the ocean's mixed layer [Hasselmann, 1976, Frankignoul and Hasselmann, 1977] and glaciers [Oerlemans, 2000, Roe, 2011]. In terms of lakes, both the spatial and temporal integration of evaporation and precipitation can complicate the attribution of a lake-level change to a single climatic event.

In this study we develop a lake-level model to characterize the nature of a lake's response to climate variations, aiming to improve interpretations of lake-level changes in relation to climate, and quantify the integrative nature of lakes. We choose to focus on the closed-basin Great Salt Lake (GSL), because of its long historical lake-level and climate records and detailed bathymetry, though this work can be applied to any other closed-basin lake system. The model is validated against historical measurements. In order to estimate the lake-level response to interannual variability alone, we drive the lake model with a synthetic record of year-to-year fluctuations based on modern instrumental observations of precipitation and evaporation that occur even without a climate change.

Using a mass-conservation model, we calculate the principal metrics of lake variability: the standard deviation and autocorrelation of the lake-level record, and the expected frequency with which a lake exceeds or falls below a given level. We also create a linearized version of the lake-level model, for which analytic expressions for the above metrics can be derived, and which capture much of the behavior of the full model. The differences between the two models highlight the non-linear aspects of the lake's response. We find that the magnitude of the GSL's historical lake-level fluctuations is consistent with a system driven purely by interannual variability.

Finally we emphasize the importance of lake geometry on the integration of climate by contrasting lake-level response to interannual climate variability for three distinctly-shaped closed-basin lakes. Their divergent responses highlight the importance of understanding how a lake's unique geometry and mean climatic state integrates the regional climate history.

4.2 The Great Salt Lake

The GSL is located to the northwest of Salt Lake City, Utah, USA. It is bounded by the West Desert to the west, the Wasatch Range to the east, and is one of the largest terminal lakes in the world, with a surface area averaging 4300 km^2 (including evaporation ponds for mineral recovery) over the past 166 years (see Fig. 4.6A). The GSL is filled predominantly by inflow from surrounding rivers (66%) and direct precipitation (31%), with groundwater accounting for the small balance of the input [Arnow, 1985]. Water is lost primarily through evaporation. Despite its vast area, the lake is quite shallow, with a maximum depth of $\sim$10 meters [e.g. Arnow and Stephens, 1990]. This aspect ratio is summarized in the lake's hypsometry (Fig. 4.6B, taken from Loving et al. [2000]). These dimensions mean that even a small imbalance between inflow and outflow can drive large changes in lake area.

The GSL has a long historical record of lake level (Fig. 4.6A). From 1847-1874, lake levels were estimated by observing the water depth over sandbars in the lake [Arnow and Stephens, 1990]. Since 1875, the United States Geological Survey (USGS) has been collecting water-surface elevation data directly. After linearly detrending the time series of interannual lake level, the standard deviation is 1.14 m. We will characterize lake level by the elevation of the lake surface above sea level (a.s.l.). Over the historical record, the average lake level has been 1280.4 m a.s.l. The record low, in 1963, was 1277.5 m a.s.l., corresponding to a maximum depth of 8 m and a surface

area of $\sim$ 2500 km^2. In contrast, the lake's historical high in 1987 of 1283.8 m a.s.l. corresponds to a depth of 14 m, and a surface area of $\sim$6200 km^2. This high stand required an expensive pumping project to relocate the excess water [Loving et al., 2000]. Thus, lake area has varied by a factor of approximately 2.5 over the historical record.

4.2.1 Climate

Precipitation

The catchment basin of the GSL is large (5.5×10^4 km^2) and topographically varied, so a single rain gauge does not reflect the entire basin's precipitation. Given sparse, and sometimes noncontinuous records, there will be some uncertainty in the precipitation history. For this work, we choose to use the University of Delaware's monthly gridded precipitation product, which provides a continuous record from 1900–2010, based on an interpolation onto a 0.5° by 0.5° latitude/longitude grid [Matsuura and Willmott, 2012]. We sum the monthly totals into an annual record based on the water year, from October to September [Arnow, 1985, Arnow and Stephens, 1990] (Fig. 4.6B). Based on this data set, the mean (μ_P) and standard deviation (σ_P) in precipitation for the GSL are 0.37 m yr^{-1} and 0.08 m yr^{-1}, respectively.

Evaporation

Because it is difficult to directly measure, evaporation data is sparse and unreliable. Overlake evaporation is a function of temperature, wind, relative humidity, and salinity [e.g. Morton, 1986]. Among these variables, only temperature has a long and reliable record. The average yearly summer (JJA) temperature record is shown in Fig. 4.6C (from Willmott et al. [2012]; μ_T = 21.3 °C, σ_T = 0.91 °C). Evaporation

records of the GSL have been derived through mass-balance modeling and a modified Penman-Montieth equation, though each of these has drawbacks [Mohammed and Tarboton, 2012]. The mass balance approach assumes that all other quantities are perfectly known, while the modified Penman equation may not properly apportion the system's available energy, and is more appropriate for timescales on the order of a day.

We follow Waddell and Barton [1980], Arnow [1985], and Arnow and Stephens [1990] in estimating overlake evaporation on the basis of nearby pan-evaporation data. We piece together the temporal variations in evaporation using pan-evaporation records from two sites near the GSL: Saltair (1957-1990) and Logan Farm (1971-2000) [data from Western Regional Climate Center, www.wrcc.dri.edu]. We align these records, setting the mean to μ_E=1 m yr^{-1}, and the standard deviation to $\sigma_E = 0.1$ m yr^{-1}, in agreement with the water-balance model of Mohammed and Tarboton [2012] (Fig. 4.6D). Pan-evaporation records are subject to significant uncertainty, but are reasonable, if imperfect estimates of overlake evaporation, capturing the relative changes over time. We will later show that evaporation is of secondary importance to precipitation in driving the GSL's lake-level changes, and so our analysis is not critically dependent on the evaporation record.

4.2.2 Persistence in the lake and the climate time series

It is clear even visually from Fig. 4.6 that the time series of precipitation, temperature, and evaporation have much less persistence than that of the lake itself. Persistence can be explicitly quantified by calculating the autocorrelation function of a time-series (Fig. 4.3). One simple test of whether there is any significant persistence in a time series is whether the lag-1 autocorrelation exceeds $\frac{2}{\sqrt{N}}$, where N is the number of points in the time series [e.g. Von Storch and Zwiers, 2001]. These threshold levels are shown for their respective time series in Fig. 4.3. Based on this test, we conclude

that no significant persistence exists for temperature and evaporation. Some slight interannual persistence may be indicated for the precipitation record, though its significance is marginal.

Fig. 4.3 demonstrates that the lake-level fluctuations themselves do exhibit significant persistence, and further, that this persistence is characterized by an exponential fit with a characteristic e-folding timescale, or memory, of approximately 8 years. The exponential fit underestimates the autocorrelation at lags less than five years, a discrepancy which we explore later in this chapter. Because there is little to no persistence in the climate variables, the lake's memory must arise from the dynamics of lake adjustment rather than being intrinsic to the climate. The main point of the present study is that the lake exhibits memory that is not present in the climate. Analysis of the lake models that we develop below explain much of this behavior.

4.2.3 Previous research

Prior research has characterized the GSL as a low-order dynamical system, and suggests that the lake's volume anomalies slightly lag the regional precipitation and temperature anomalies [Abarbanel and Lall, 1996, Abarbanel et al., 1996, Sangoyomi et al., 1996, Lall et al., 1996]. Related research invokes low-frequency climate phenomena to explain the low-frequency response of the GSL [Mann et al., 1995, Lall and Mann, 1995, Moon et al., 2008, Wang et al., 2010]. These studies aim to use some combination of atmospheric indices to predict the GSL lake levels. In this study we aim to put these explanations into context by considering the natural variability of lake level that occurs in response to white noise – the stochastic year-to-year fluctuations in weather that occur even without any climate change or persistence in the climate.

Other studies have considered the inherent lake dynamics of GSL. Kite [1989] proposed that the changes and apparent periodicity in the GSL's record are within the range of normal fluctuations and are not ascribed to climatic change. Mohammed and Tarboton [2011] refer to the lake's bathymetry to explain the large and long excursions of the lake record. They note that the area of the lake controls the outgoing flux, and therefore a shallow lake like the GSL is quickly stabilized and modulated by the available evaporative surface. In subsequent work, Mohammed and Tarboton [2012] use a simple lake model to calculate the sensitivity of the GSL to changes in inflow, precipitation, and air temperature, and use variations of historical climate input to predict possible future lake-level scenarios.

Our work is similar in spirit to that of Mohammed and Tarboton [2011, 2012], but rather than being predictive, our goal is to understand the natural lake variability in order to put past and anticipated future fluctuations in context. We also extend this work by considering the role of lake alternate bathymetries on natural lake-level variability.

4.3 Model

In the following section, the full and linearized models are described. The full model is similar to that of Mason et al. [1994], who derive general and comprehensive time-dependent solutions to a lake's water balance. They explore the response of lake level and area to step changes, single brief excursions, and sinusoidal variations in the climate. In contrast, our focus here is on the lake's response to the continuous random perturbations in forcing that occur even in a constant climate.

4.3.1 Full model

The rate of volumetric change for a closed-basin lake such as the GSL is determined by the balance of inflow into and evaporation out from the lake, illustrated in Fig. 4.4. The mass budget can be described by a straightforward differential equation:

$$\frac{dV}{dt} = PA_L + I - EA_L, \tag{4.1}$$

where $V_L(t)$ is the lake's volume, $A_L(t)$ is the lake's surface area, $P(t)$ is the annual regional precipitation rate, $I(t)$ is the total annual river inflow from the surrounding basin, and $E(t)$ is the annual evaporation rate over the lake, all functions of time, t.

Eq. (4.1) can be rewritten in terms of lake-level variations. The volume of water is a unique function of lake level: $V = V(h)$, which can also be written as $V(h) = \int_0^h A_L(z)dz$. Hence

$$\frac{dV}{dt} = \frac{dV}{dh}\frac{dh}{dt} = A_L(h,t)\frac{dh}{dt}. \tag{4.2}$$

Substituting eq. (4.2) into eq. (4.1) yields:

$$\frac{dh}{dt} = \frac{1}{A_L}\left(PA_L + I - EA_L\right). \tag{4.3}$$

We assume that the long-term mean of the inflow, $\bar{I}$, is proportional to the product of the long-term mean of the annual regional precipitation rate, $\bar{P}$, and the area over which runoff is collected (i.e., the area of the catchment basin, excluding the direct precipitation over the lake):

$$\bar{I} = \alpha\bar{P}(A_B - \bar{A_L}), \tag{4.4}$$

where A_B is the entire catchment area of the lake. The parameter α reflects the fact that much of the precipitation that falls into the basin is lost to evapotranspiration or groundwater percolation. Some of the uncertainty in regional precipitation

may also be subsumed into α. We set α so that the lake level matches its long-term mean. For the GSL an α of 0.13 yields an $\bar{I}$ of 2.5 km^3 yr^{-1}, which is close to the values estimated from stream gauges by Arnow and Stephens [1990] (2.3 km^3 yr^{-1}) and Mohammed and Tarboton [2012] (2.8 km^3 yr^{-1}).

The fluctuations in inflow, I' are parametrized as

$$I' = \gamma P'(A_B - A_L), \tag{4.5}$$

where P' denotes the variations away from $\bar{P}$. We have introduced a tunable parameter, γ, which ensures that the interannual fluctuations in inflow are the same as observed. We find we need $\gamma = 0.40$ in order to emulate the observed standard deviation of inflow which is $\sim$1.5 km^3 yr^{-1} [Mohammed and Tarboton, 2012]. That we require different values for α and γ suggests that there is some slow-timescale process in the region's groundwater that is neglected in our model. For the purposes of our study here, our goal is to drive the lake model with interannual variability in inflow whose magnitude is consistent with observations. Our use of γ allows us to do that.

We use the time series of P and E shown in Fig. 4.6B & D to force eq. (4.3), using the parameter values shown in Table 4.1, starting in 1901 with the initial condition of $h = 1280$ m a.s.l., consistent with the observations. This initial lake level corresponds to a volume of 18.4 km^3 and an initial area of 4100 km^2. From 1901-1956, there is no evaporation data, and so for this interval we force the lake with variations in precipitation only, keeping the evaporation rate at its long-term mean of 1 m yr^{-1}. The simulated lake-level history is shown in Fig. 4.6A. Despite its crude treatment of inflow and incomplete evaporation record, the detrended interannual standard deviation of model lake level (1.19 m), agrees well with that of observations (1.14 m). The model time series correlates with observations at $r = 0.85$. The fact the model does a good job in the early part of the record, despite the absence of evaporation variations

suggests that the precipitation is of primary importance in driving lake-level fluctuations, a result we confirm in the next section.

4.3.2 Linear model

In the following section, we develop a linear version of the lake-level model. From it, we derive analytical solutions for the lake's relaxation timescale, the relative importance of P and E, and the variance of the lake level in response to stochastic climate forcing. The analytic expressions allow us to characterize the behavior of the lake without a complete knowledge of lake bathymetry and to clearly understand the parameters that drive the lake-level responses to climate variations.

Eq. (4.3) is linearized by rewriting all time-varying fields using overbars to denote long-term means, and primes to denote anomalies from that mean: $P(t) \equiv \bar{P} + P'(t)$, $E(t) \equiv \bar{E} + E'(t)$, $I(t) \equiv \bar{I} + I'(t)$, $A_L(t) \equiv \bar{A}_l + A'_L(t)$, and $h(t) \equiv \bar{h} + h'(t)$.

Using eq. (4.4) and eq. (4.5) for $\bar{I}$ and I', eq. (4.3) becomes:

$$\begin{aligned}\frac{d(\bar{h}+h')}{dt} = \frac{1}{(\bar{A}_L + A'_L)} [\ &(\bar{P}+P')(\bar{A}_L + A'_L) + (\alpha\bar{P} + \gamma P')(A_B - (\bar{A}_L + A'_L)). \\ &- (\bar{E}+E')(\bar{A}_L + A'_L)\ ]\end{aligned} \tag{4.6}$$

Because A_L is a function of h, we rewrite it using a first-order Taylor Series expansion:

$$A_L(h) = A_L(\bar{h}+h') = A_L(\bar{h}) + \frac{dA_L(\bar{h})}{dh}h' \equiv \bar{A}_L + \frac{d\bar{A}_L}{dh}h'. \tag{4.7}$$

Substituting $\frac{d\bar{A}_l}{dh}h'$ for A'_l, and considering only first-order terms, eq. (4.6) becomes:

$$\frac{dh'}{dt} + \frac{h'}{\tau} = \left[1 - \gamma + \frac{\gamma A_B}{\bar{A}_L}\right] P' - E', \tag{4.8}$$

where

$$\tau = \frac{\bar{A}_L}{\frac{d\bar{A}_L}{dh}(\bar{E} - \bar{P}(1-\alpha))}. \tag{4.9}$$

The value for τ represents the characteristic, e-folding timescale on which perturbations in lake level will relax towards the mean. A large $\bar{A}_L$ implies that τ will also be large, because, all else being equal, for a given h', there is a large anomalous volume, $\bar{A}_L h'$, that must be either filled or evaporated to return to equilibrium. A large value of $^{d\bar{A}}/_{dh}$ is associated with smaller τ, because it means that an increase in h' leads to a large increase in evaporating area, enabling the excess volume of water to be more rapidly removed. Likewise, a decrease in h' significantly decreases the evaporating area, reducing the total evaporation, and allowing the lake to return more rapidly to equilibrium. Finally, a large difference between $\bar{E}$ and $\bar{P}(1-\alpha)$ indicates that the lake is in an arid region, and that the restoring tendency of E is relatively efficient. Aridity, therefore, also tends to shorten the response time of a lake. However as we discuss below, in a given setting these three factors influencing τ cannot be considered independent of each other.

The GSL is a large, shallow lake in an arid environment and so there are trade-offs between the factors that determine τ. For the values shown in Table 4.1, eq. (4.9) predicts that $\tau = 10$ yrs. Our τ falls within the range of 4–17 years cited by Mason et al. [1994], who estimate several equilibrium e-folding response times for different historical levels of the GSL. Further, our value for τ compares quite well with the e-folding time suggested from observations (8 yrs, Fig. 4.3).

From eq. (4.9), we see that τ is a function of the mean lake level (since $\bar{A_L}$ and $\frac{d\bar{A_L}}{dh}$ are functions of h), and the mean climatic setting. τ is therefore a function of a particular mean state of the lake. The black line in Fig. 4.5 shows how τ varies with $\bar{h}$ for the GSL, keeping $\bar{E}$, $\bar{P}$, and α fixed. Over the historical range of GSL lake levels (1277.5 to 1283.8 m a.sl.), τ ranges from as low as 5 years at 1280 m a.s.l., to as long as 26 years at the historical high. The 5-year response time is due to a large value of $^{d\bar{A_L}}/_{dh}$, indicating that the basin area is changing rapidly at these elevations (evident in Fig 4.6B). The 26-year response time corresponds to a large value for $\bar{A_L}$, as well as a relatively small value for $^{dA_L}/_{dh}$. The timescale plummets for elevations above 1284 m a.sl., because $^{dA_L}/_{dh}$ increases, allowing the lake to quickly adjust to anomalies in the water balance.

However, it is not consistent to vary $\bar{h}$ independently, since a long-term lake-level change also requires an accompanying change in $\bar{P}$ or $\bar{E}$ to maintain the new mean lake level. For example, an increase in $\bar{A_L}$ only happens if also accompanied by a decrease in $\bar{E}$ or an increase in $\bar{P}$. These both work in the same direction as an increase in $\bar{A_L}$, acting to increase τ. Thus, it is more realistic to constrain τ through consistent combinations of $\bar{h}$, $\bar{P}$, and $\bar{E}$ that ensure the lake is in equilibrium (i.e. $\frac{dV}{dt} = 0$ for a given $\bar{h}$). Fig. 4.5 shows two examples. For the first (blue line), we vary $\bar{P}$ keeping $\bar{E}$ fixed, so that $\frac{dV}{dt} = 0$ in eq. 4.3. For the second (red line) we vary $\bar{E}$, keeping $\bar{P}$ fixed.

When the parameters covary like this, the basic pattern of the variation of response time with lake level is the same as varying $\bar{h}$ on its own. However, confirming the reasoning given above, the variations in τ are amplified. τ reaches 40 yrs for $\bar{h} = 1284$ m a.sl., when $\bar{h}$ and $\bar{E}$ covary (Fig. 4.5).

Despite the large changes in τ as a function of $\bar{h}$, the linear model (eq. 4.8) does

a remarkably good job of emulating the historical lake level record when it is driven by the historical variations in P' and E' (Fig. 4.6A). The correlation with the observations is 0.83, only slightly smaller than that for the full model. The results lend confidence that we can use the linear model to derive analytical expressions for some useful metrics of the lake response.

Response to step changes in P and E

Let ΔE be a step-change in evaporation rate. From eq. (4.8), and assuming $P' = 0$, the resulting equilibrium change in lake level (i.e., when ${}^{dh}/_{dt} = 0$) is

$$\Delta h_E = -\tau \Delta E. \tag{4.10}$$

Similarly, for a step-change in the precipitation rate, ΔP, the resulting change is

$$\Delta h_P = \left[1 - \gamma + \frac{\gamma A_B}{\bar{A}_L}\right] \tau \Delta P. \tag{4.11}$$

A simple measure of the relative importance of P and E for the lake level is the ratio of Δh_E and Δh_P:

$$R_{\Delta h} = \left|\frac{\Delta h_E}{\Delta h_P}\right| = \left|\frac{-\Delta E}{\left(1 - \gamma + \frac{\gamma A_B}{\bar{A}_L}\right) \Delta P}\right|. \tag{4.12}$$

In other words, $R_{\Delta h}$ is proportional to the ratio of the two climate changes, modified by the lake geometry and evapotranspiration in the catchment basin.

Standard deviation in lake level

As was argued in the introduction, and as was supported by an analysis of the instrumental climate record, a sensible null hypothesis is that interannual climate variability

can be characterized by stochastic, normally-distributed white noise, with standard deviations in P' and E' of σ_P and σ_E respectively.

Analytical solutions for the standard deviation in lake response, σ_L, can be derived for the lake-level response to the stochastic variability from eq. (4.8), and are presented in the Appendix C. For lake-level variability driven by $E'(t)$ alone, we find

$$\sigma_{hE} = \sigma_E \sqrt{\frac{\Delta t \tau}{2}}. \tag{4.13}$$

Lake-level variability driven by $P'(t)$ alone is

$$\sigma_{hP} = \sigma_P \left[1 - \gamma + \frac{\gamma A_B}{\bar{A}_L}\right] \sqrt{\frac{\Delta t \tau}{2}}. \tag{4.14}$$

Combining eqs. (4.13) and (4.14), we get:

$$\sigma_h^2 = \sigma_{hE}^2 + \sigma_{hP}^2. \tag{4.15}$$

For the GSL, $\sigma_{hP} = 1.04$ m, $\sigma_{hE} = 0.24$ m, and $\sigma_h = 1.07$ m, meaning that P' contributes 95% of the variance in fluctuations in h'. This confirms our earlier result (Fig. 4.6A), that lake level fluctuations in the GSL are predominantly driven by precipitation variability. A more comprehensive study of lake geometry and climatic conditions would be needed to establish whether this is generally true, or whether under some conditions evaporation variability dominates. The predominant importance of precipitation and inflow for the GSL is also noted by Mohammed and Tarboton [2012].

4.4 Lake-level statistics

To this point, we have demonstrated that both the full and linear models can capture the general behavior of the GSL's historical lake-level variations. We now turn to

characterizing the lake's behavior beyond the historical record: its variance; power spectrum; lake-level threshold-crossing probabilities; and evaluating the analytical expressions derived from the linear model, when forced with stochastic climate variations. The differences between the models highlight the capacity of the analytic solutions to describe the behavior of the lake, and the degree to which changes in the geometry of the lake basin and bathymetry are important.

We force the full and linear models with long (10^6 yr) realizations of $P'(t)$ and $E'(t)$ generated from normally distributed, white-noise processes that have the same mean and variance as the observations (detailed in Table 4.1). A 300-year snapshot of the resulting lake-level time series is shown in Fig. 4.6A, with the full model in grey, and the linear model in blue. The full time series correlate highly with one another (r =0.89), but there are also notable differences. For example, because the full model resolves changes in $\frac{d\bar{A_L}}{dh}$, which decreases below the present lake level, the full model's response time is longer at lake levels just slightly lower than the mean lake level. Therefore, the full model's lake level is consistently lower than that of the linear.

4.4.1 Standard deviations

For the full model, we find σ_h = 1.1 m, in close agreement with the linear model (also σ_h = 1.1 m). The probability density functions (PDFs) are shown in Fig. 4.6A. The PDF of the lake levels for the linear model is normal by construction, but the actual hypsometry of the GSL introduces a significant degree of skewness in the full model (skewness = -0.4; kurtosis = 3.9). Therefore, the full model is not consistent with a normal distribution (at p = 0.05, based on a Kolmogorov-Smirnov test [e.g. Von Storch and Zwiers, 2001]).

Relative to the mean, the full model's lake-area extremes are skewed towards neg-

ative excursions (Fig. 4.6B). The area that is associated with $+3\sigma_h$ is 6000 km^2, and covers about 2.5 times the area associated with $-3\sigma_h$, 2300 km^2 (Fig. 4.6C and D). This range is comparable to the difference between the highest and lowest areas in the historical record, and describe the expected extremes seen in a thousand-year period, if there was no climatic change.

4.4.2 Power spectral density

The power spectra of lake level for the models and the historical record are shown in Fig. 4.6B. The spectrum for the linear model is calculated using a standard formula for eq. (4.8) [e.g. Box et al., 2013], which applies to frequencies $0 \leq f \leq \frac{1}{2\Delta t}$:

$$\mathcal{P}(f) = \frac{\mathcal{P}_0(\frac{\Delta t}{\tau})^2}{1 - 2(1 - \frac{\Delta t}{\tau})\cos(2\pi f \Delta t) + (1 - \frac{\Delta t}{\tau})^2}, \tag{4.16}$$

where $\mathcal{P}(f)$ is the power spectral density, $\mathcal{P}_0 = 4\tau\sigma_h^2$, and σ_h is taken from the linearized model (i.e., eq. 4.15).

The area beneath the power spectrum is the variance of the time series, and so the similarity of the power spectra of the full and linear models is consistent with their values for σ_h also being similar. There are however some noteworthy differences between the models and the observations. While the spectral power at low frequencies is quite similar, the observations are more damped than the models at high frequencies.

The power spectrum is the Fourier transform of the autocorrelation function [e.g. Box et al., 2013]. Therefore the extra damping at high frequencies in observations above that predicted by eq. (4.16) is consistent with the observed autocorrelations at short lags being higher than predicted by a simple exponential function (Fig. 4.3). Similar behavior was found recently for the glaciers by Roe and Baker [2014].

For the GSL, these results suggests that neither eq. (4.3) nor eq. (4.8) are complete descriptions of the lake response. In particular, groundwater dynamics likely impacts lake-level variability at higher frequencies. Further development of the model might better emulate the observed autocorrelation/power spectrum structure. These differences notwithstanding, the results confirm the basic principle embodied in the models. For the historical record, persistence in lake level fluctuations is associated with the dynamic memory of the lake system, rather than persistence in climate.

4.4.3 Threshold crossing statistics

Often it is the extrema of lake level (i.e. a flood or extreme lowering) that have the highest impacts on water resources and are most evident in proxy records. A metric of particular importance then, is the likelihood that a given lake level is reached in a given period of time. Given interannual climate variability, the question is inherently a statistical one. For the full model, the statistics can be estimated from the long idealized simulations of lake level. For the linear model, the statistics can be derived analytically from the statistics of a Poisson distribution [e.g. Von Storch and Zwiers, 2001, Roe, 2011]. The probability of the lake level exceeding a given threshold, h_0, above or below the long-term average at least once in a given interval of time, $t_f - t_i$, is given by:

$$p(N(t_f - t_i) \geq 1) = 1 - exp\left[-\frac{t_f - t_i}{2\pi}\left(\frac{2}{\tau\Delta t}\right)^{\frac{1}{2}} e^{-\frac{1}{2}\left(\frac{h_0}{\sigma_h}\right)^2}\right]. \tag{4.17}$$

Eq. (4.17) shows that the longer the time interval $(t_f - t_i)$, the higher the probability of exceeding a given threshold. This probability depends on τ, but is especially sensitive to the ratio of h_0 and σ_h.

Fig. 4.6A shows results for time intervals of of 100, 500, and 1000 years. For the

full model we randomly sample these intervals 10^5 times from the long model integration, and collate the statistics of how often a give lake level is crossed. As an example, for the full model, in any 1000 yr period it is extremely likely (98%) to find the lake level exceeding 2m, and extremely unlikely (1%) to find the lake level exceeding 4m.

The threshold-crossing probability curves show that the full and linear models diverge at the extremes. For the linear model, the maxima and minima curves are symmetric about the mean lake level, as expected from the probability distribution function of the lake levels (Fig. 4.6A). However, for the full model, a large lake-level minimum is more likely than a lake-level maximum of the same magnitude. This is also apparent in Fig. 4.6A, where the full model's lake levels are consistently lower than those of the linear model, and in (Fig. 4.6B), which shows differences between the spectra of each model. Though the standard deviations of the models are quite close, the linear model overestimates the frequency of a lake-level maximum and underestimates the frequency of a lake-level minimum, relative to the full model.

Fig. 4.6B shows the full model's frequency-crossing distribution for the total excursion of a given time slice (i.e. the (maximum - minimum) values within $(t_f - t_i)$). This illustrates total expected spread in the the lake level on the order of 100, 500, or 1000 years. The GSL has a higher than 50% probability of varying more than 4 meters within a century; more than 6 meters every 500 years; and more than 7 meters every millennium. Interestingly, Karl and Young [1986] inspected the return times for precipitation records alone, and found that there was greater than 50% probability of having a wet spell as extreme as the 1986 floods in any hundred year period, with a return time of 120 years. The similarity between the high precipitation probability and flood probability is unsurprising, given how sensitive the lake is to changes in precipitation.

4.5 Alternative lake hypsometries

We have focused on the GSL because of its long lake-level history, relatively short response time, and detailed hypsometric information. However, the framework developed above can be used to characterize any closed-basin lake's response to variations in the climate. This response will be dependent on the lake's unique hypsometry and regional climate.

To understand the extent of geometric influence on the timescale and magnitude of lake-level variability, we create simple hypsometric profiles that are approximations to the bathymetry of three closed-basin lakes: the extensive and shallow GSL; the extensive and deep Lake Titicaca, on the border of Bolivia and Peru; and the areally small and deep Lake Bosumtwi in Ghana (Fig. 4.6A, B, and C). In the following calculations we *do not* try to simulate historical or projected future variations of these lakes, but aim to isolate the impact of different lake geometries on lake-level response. The simple functions used to describe the bathymetry allow $d\bar{A}_L/dh$ to vary smoothly, in turn, smoothing the lake-level response.

The GSL and Lake Titicaca's hypsometric curves are concave down, and can be idealized as an inverted rectangular pyramidal frustum:

$$A_L(h) = LW\left(\frac{h + z_0}{z_0 + z_1}\right)^2, \tag{4.18}$$

where, again, A_L is the lake area and h is the lake level. L and W are the length and width of the basin at some known elevation, z_1, above the bottom of the frustum, and z_0 is the vertical distance from the bottom of the frustum to the point that would complete a full pyramid.

Lake Bosumtwi's hypsometric curve is concave up, and is idealized as a tri-axial

half-ellipsoid:

$$A_L(h) = \pi LW \left(1 - \frac{(z_0 - h)^2}{z_0^2}\right), \tag{4.19}$$

where L, W and z_0 are the lengths of the semi-principal x, y, and z axes, and $h = 0$ at $z = z_0$. The values for each lake's parameters are given in Table 4.2, and are compared with the known hypsometric profiles in Fig. 4.6.

Estimates for $\bar{E}$ and $\bar{P}$ for lakes Titicaca and Bosumtwi are available from the literature (Table 4.2, Turner et al. [1996], Richerson et al. [1977]). For each idealized lake geometry, we set α so as to match the modern lake levels. By analogy with the GSL, we set $\gamma = 3\alpha$.

In order to focus solely on the impact of the different basin geometries on lake-level variability, we apply the same $E'(t)$ and $P'(t)$ to all three idealized lake geometries as were applied to the GSL (see section 4.4). We integrate the full lake model (eq. 4.3) with each of the idealized lake geometries, and use the linear model solutions to calculate τ, σ_h, and $\mathcal{P}(f)$ for each lake. All parameters are provided in Table 4.2.

A 2000-year slice of each lake's time series is shown in Fig. 4.6D. It is clear that the lakes respond to the same perturbations at different timescales and with different amplitudes. The analytic solutions to the linear model allow us to link the differences in lake response to each lake's parameter values.

4.5.1 Response time

The response time for each lake is calculated using eq. (4.9). The idealized GSL has the fastest response time, with a $\tau = 10$ years, because of its large $d\bar{A_L}/dh$. The shape of Lake Bosumtwi is very different, with a relatively small area of 48 km^2, but a modern

depth of 79 m. Its geometry means that if Lake Bosumtwi experiences a brief increase in P, the lake level will increase, but the lake's surface area only increases slightly. Hence, it takes many years for a steady $\bar{E}$ to remove the excess water and return the lake to its original level. Therefore, though the surface area of Lake Bosumtwi is much smaller than that of Lake Titicaca or the GSL, its small $d\bar{A_L}/dh$ gives the lake a long memory, with an e-folding time of 209 years. Lake Titicaca is much larger ($\bar{A_L} = 6700$ km^2) and deeper ($\bar{h} = 280$) than the GSL or Lake Bosumtwi. However, Lake Titicaca's ratio of $\bar{A_L} : d\bar{A_L}/dh$, and therefore its τ (= 201 yrs), is similar to that of Lake Bosumtwi.

The mean climatic differences ($\bar{P}, \bar{E}$) also affect τ, as does the ratio of $\bar{A_L}$ and A_B, through the α needed to maintain the modern lake level. These effects are, however, of secondary importance to the basin hypsometry. The hypsometry of the lake, then, is the main control over the response time of the lake, which, in turn, determines the integration of the climatic history in the lake-level record.

4.5.2 Standard deviations

For the idealized GSL geometry, σ_h= 1.2 m (1.1 m) for the full (linear) model, which is very similar to the values for the original model runs. Lake Bosumtwi's σ_h is comparable, with $\sigma_h = 1.7$ m for both models. The reason that σ_h is similar for Lake Bosumtwi and the GSL is because τ and basin geometry compensate one another (eq. 4.15): while τ is much larger for Bosumtwi than the GSL, the ratio of $A_B/\bar{A_L}$ is much smaller. Lake Titicaca, with a large values for both τ and $A_B/\bar{A_L}$, exhibits the largest values for σ_h – 4.0 m (4.1 m) for the full (linear) model.

4.5.3 Power spectrum

Fig. 4.6E shows the lake-level power spectra for each of the three lakes. The $\mathcal{P}(f)$s from eq. (4.16) are also shown. The GSL has more power at high frequencies than Lake Bosumtwi or Lake Titicaca, with their long response times. Lake Bosumtwi and Lake Titicaca, which have similar values for τ, have similar spectral shapes, though Titicaca has more power at all frequencies, simply because its variance is greater. The smaller τ and lower overall variance for GSL means that it asymptotes more rapidly and to a lower value of $\mathcal{P}(f)$ at low frequencies.

Mason et al. [1994] show that the high-frequency component of lake-level variability is proportional to $\bar{E} - \bar{P}$ and the ratio of $\bar{A_L}$ to A_B, while the low-frequency component is proportional to τ, $\bar{E} - \bar{P}$, and the ratio of $\bar{A_L}$ to A_B. Our findings corroborate this, since Titicaca and Bosumtwi, with their similar values for τ have spectra that diverge from the GSL's at low frequencies. Similarly, the spectra of the GSL and Titicaca are more similar at high frequencies, because their $\bar{E} - \bar{P}$, and the ratio of $\bar{A_L}$ to A_B are more comparable.

4.6 Discussion and summary

Lakes are sensitive recorders of climate, responding to both climate change and interannual climate variability that occurs even in a constant climate. Our particular focus in this study has been characterizing lake response to the latter.

Lakes have an intrinsic dynamical time scale, which is a function of their geometry, hydrology, and climatic setting. A physical interpretation is that this is a filling or evaporating timescale–the length of time it takes to replenish (or evaporate) an anomalous volume of water. It is, in an e-folding sense, the timescale over which the

lake integrates previous climate fluctuations to produce persistent lake fluctuations (e.g., eq. 4.8). The lake response also reflects a spatial integration of the climate, because the rivers that flow to the lake are fed by basin-wide precipitation. This understanding of the spatial and temporal integration of a lake can help to identify climate changes in paleo-records, or qualify an expected the frequency of floods and droughts in a record, even in the absence of climate change.

For the case of GSL, we showed there was negligible persistence in the climate variability over the historical record, and therefore that the observed persistent lake-level fluctuations are due to the lake's response time. A simple volumetric model was developed that provided a good simulation of the historical GSL lake level. A linearization of the model performed comparably well and provides some analytic expressions for lake-level sensitivity, variance, power spectrum, and statistics of lake-level threshold crossings. The linear model's lake-level distribution is normal, and so does not capture the negative skewness of the full model's lake-level PDF. The distributions in area for both models are non-normal.

While the lake models accurately capture the low-frequency power of the historical record of the GSL, they both underestimate the high-frequencies, suggesting that not everything in the lake dynamics is captured. A more detailed analysis of the auto-correlation structure using auto-regressive moving-average (ARMA) modeling might reveal higher-order terms in the lake dynamics. This approach was recently used by Roe and Baker [2014] to analyze glacier response.

The analytic expressions derived from the linear model can provide useful first-order approximations of the expected responses of the lake, and can help characterize the baseline level of detail that can be extracted from that lake's record. We have shown that the linear model can also be used to characterize the lake-level response of

lakes with different characteristic bathymetries. While the magnitude of the historical lake-level variance is captured by the models, some details are not, in particular the high-frequency response of both models. We attribute this discrepancy to an imperfect inflow parametrization, and the lack of a parametrized groundwater forcing. The linear model fails to capture the extreme large low-stands in lake level that the full model exhibits, but emulates the full model's power spectrum and standard deviation.

The main advantage of the linear model is that it provides analytic expressions for the basic metrics, in which the dependencies on geometry and climatic setting are transparent. For many purposes the linear model may be the best approach: uncertainties in climatic forcing and evapotranspiration are likely to be larger source of error in modeling lake response than the model itself. Thus, a more complicated model may not be justified for characterizing the response to interannual variations in climate.

To explore how the geometry of the lake and surrounding basin control the amplitude and timescale of the lake-level response, we repeated our modeling exercises on idealized bathymetries of the GSL, Lake Titicaca, and Lake Bosumtwi, isolating the effect of geometry. A remarkable range of time scales are implicated from ten years for the GSL to ~ 200 years for Titicaca and Bosumtwi. The differences can be attributed to the specific parameters that set τ and σ_h. The timescale is proportional to the lake's area, and is inversely proportional to its aridity and ${}^{dA_L}/_{dh}$. The amplitude of variations is a function of τ, but it is also modified by the ratio of the basin area to the lake area. Idealized geometries, such as the frustum and half-ellipsoid, and linear models are an efficient way of characterizing uncertainty analyses when working with lakes whose bathymetry is not well characterized, when analyzing many lakes, or for preliminary field-work plans.

We have demonstrated that large and persistent fluctuations in lake level and lake extent can be driven by the random year-to-year fluctuations in weather, that occur even in a constant climate. Estimates of this natural variability are important to make in order to establish the statistical significance of modern and paleo-lake fluctuations. The models developed here reveal the dependencies on lake geometry and climatic setting, are flexible enough to be applied generally, and can help inform the interpretation of the climate history reflected in lake records. These models and statistical tests allows for this work to be applied to many different lake settings. Their strength lies in their relative simplicity, and, therefore, in our ability to understand and characterize the specific relationships between parameters that drive lake level variability.

	Variable	Historical GSL Value
V_L	lake volume	20 km^3
A_b	catchment basin area	5.5×10^4 km^2
$\bar{A}_l$	mean lake area	4300 km^2
σ_{A_l}	s.d. lake area	840 km^2
$\bar{z}$	mean lake depth	10 m
$\bar{h}$	mean lake level	1280.4 m a.s.l.
σ_h	s.d. lake level	1.14 m
$\bar{P}$	mean precipitation rate	0.37 m yr^{-1}
σ_P	s.d. precipitation rate	0.08 m yr^{-1}
$\bar{E}$	mean evaporation rate	1.00 m yr^{-1}
σ_E	s.d. evaporation rate	0.10 m yr^{-1}
α	% of basin's precip. flowing to lake (mean)	0.13
γ	% of basin's precip. flowing to lake (variance)	0.40
τ	e-folding time scale	8 yr

Table 4.1: Parameters, historical values, and model outputs describing the GSL's lake-level and climatic history. See text for sources.

	GSL	**Bosumtwi**	**Titicaca**	
z	14	192	400	m
L	150	5	150	km
W	50	4.7	80	km
A_b	55,000	72	58,000	km^2
$\bar{A}_l$	4600	48	6700	km^2
$d\bar{A}_l/dh$	665	0.45	38	km^2 m^{-1}
$\bar{h}$	9	79	280	m
σ_h	1.1	1.7	4.0	m
$\bar{P}$	0.37	1.38	0.80	m yr^{-1}
σ_P	0.08	0.08	0.08	m yr^{-1}
$\bar{E}$	1.0	1.55	1.58	m yr^{-1}
σ_E	0.1	0.1	0.1	m yr^{-1}
α	0.16	0.25	0.13	–
γ	0.47	0.75	0.38	–
τ	10	209	201	yr

Table 4.2: Parameters, and model outputs for the simplified geometry experiments. Lake Bosumtwi's climate variables are from Turner et al. [1996], and Lake Titicaca's are from Richerson et al. [1977]. σ_P and σ_E for all three lakes are, by experimental design, equal to the GSL's: these numbers are inaccurate, and should not be used in other studies.

Figure 4.1: Great Salt Lake's setting and geometry. **A:** Map view of the GSL. Data from Baskin [2005, 2006]. Lake levels are contoured every meter. For visual clarity, the surrounding topography is contoured every 20 m from 1280 to 1300 m a.s.l., every 100 m from 1300 to 1500 m a.s.l., and every 300 m from 1500 to 3000 m a.s.l. **B:** GSL's hypsometric curve from Loving et al. [2000]. The present-day lake level is 1279 m a.s.l. which corresponds to a surface are of $\sim$3500 km^2, and is slightly below the historical mean lake level of 1280.4 m a.s.l.

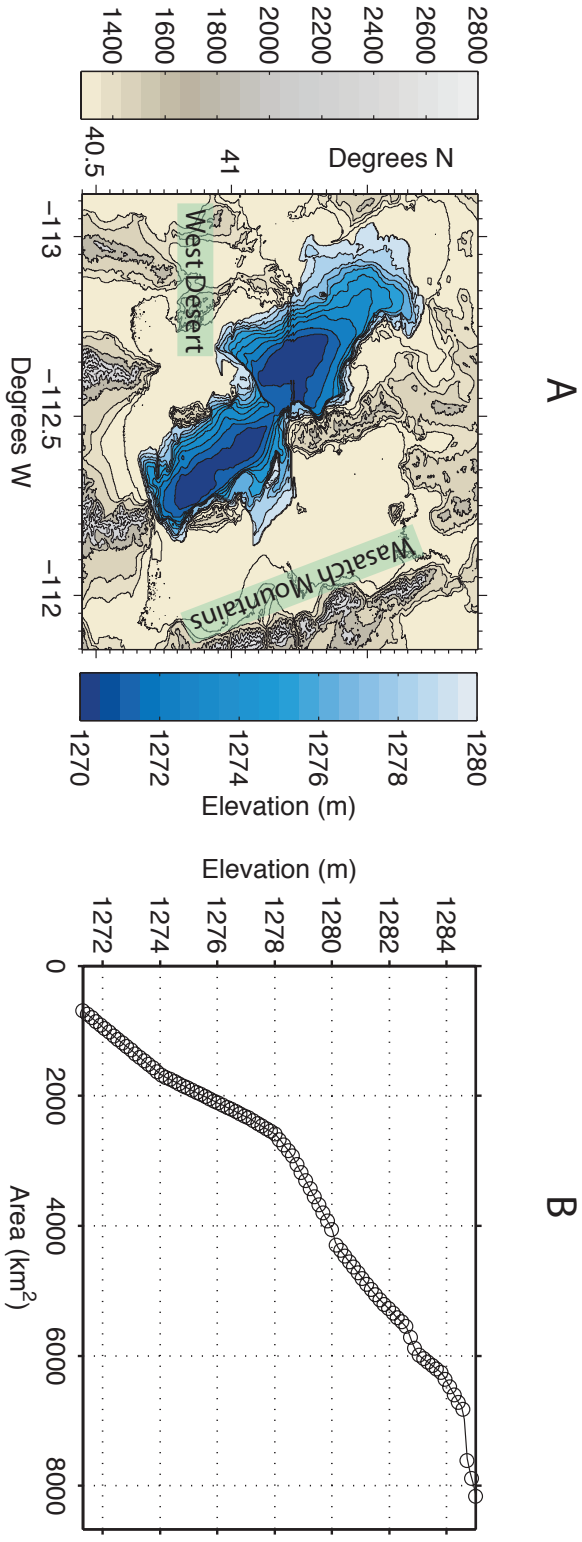
A
2800
2600
2400
2200
2000
1800
1600
1400
40.5
41
Degrees N
−113
−112.5
−112
Degrees W
West Desert
Wasatch Mountains
1270
1272
1274
1276
1278
1280
Elevation (m)
B
Elevation (m)
1272
1274
1276
1278
1280
1282
1284
0
2000
4000
6000
8000
Area (km^2)

Figure 4.2: GSL's lake level and climatological history. **A**: The historical record of the GSL, from USGS Water Resources, is shown in black. The grey and blue lines show the full and linear output from the modeled history, respectively. The models incorporate the precipitation and evaporation data from B and D. **B**: Annual regional precipitation record, from Matsuura and Willmott [2012]. Precipitation is summed over the water-year, from October to September. **C**: Mean regional summer (JJA) temperatures from Willmott et al. [2012]. **D**: Compilation of evaporation records from local pan measurements, from Western Regional Climate Center. The inset shows the approximate annual volume of water pumped from the lake in 1986-1988, divided by the lake's area, so that this rate of removal is comparable to the evaporation rate.

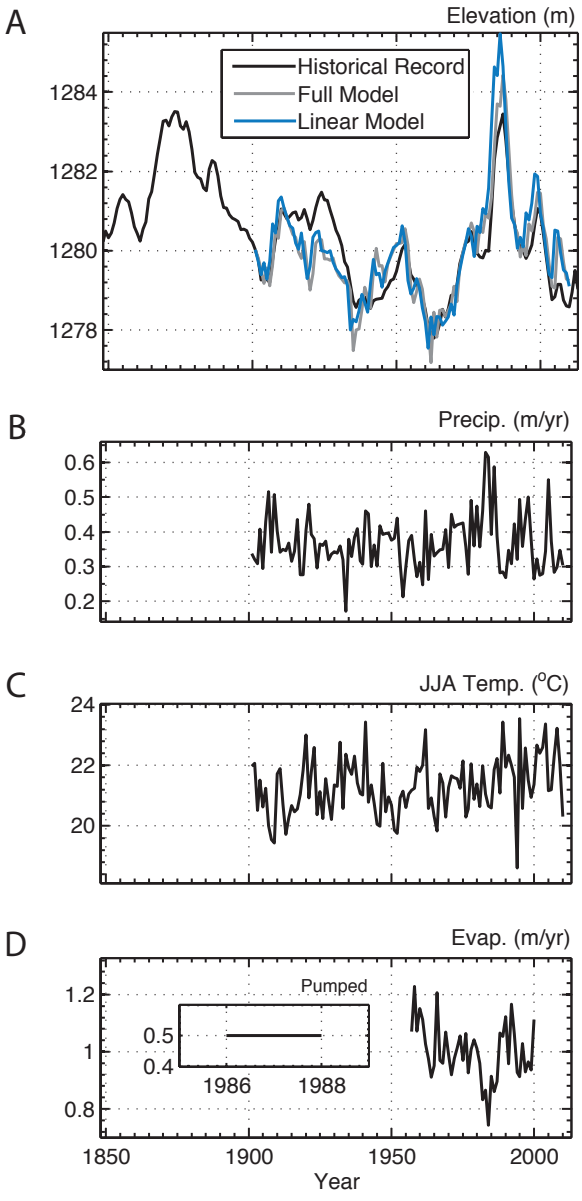
A
Elevation (m)
Historical Record
Full Model
Linear Model
1284
1282
1280
1278
B
Precip. (m/yr)
0.6
0.5
0.4
0.3
0.2
C
JJA Temp. (°C)
24
22
20
D
Evap. (m/yr)
Pumped
0.5
0.4
1986
1988
1.2
1
0.8
1850
1900
1950
2000
Year

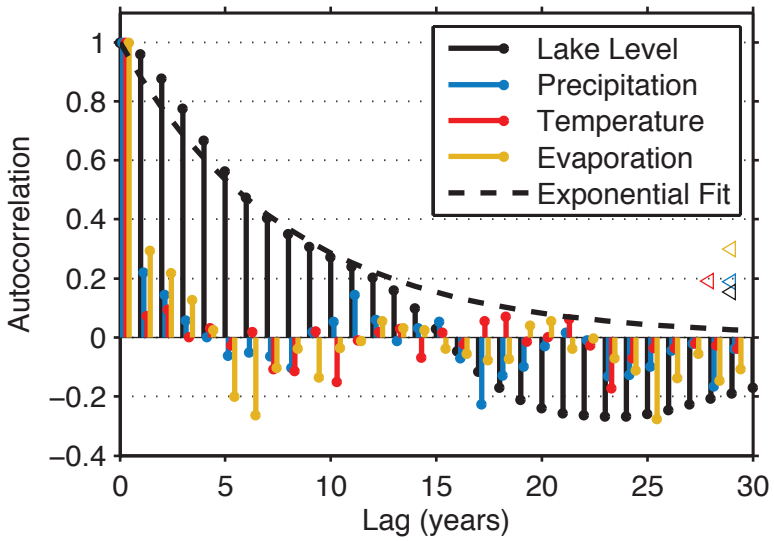

Figure 4.3: Autocorrelation function of the GSL's historical lake-level [USGS Water Resources], regional annual precipitation rate [Matsuura and Willmott, 2012], regional JJA temperature [Willmott et al., 2012], and evaporation rate [Western Regional Climate Center]. The arrows on the right side of the graph indicate the 2σ confidence level of a significant autocorrelation, which is a function of the length of the records. The lake has significant memory up to 13 years, with an e-folding timescale of 8 years. With the exception of precipitation, which exhibits a small autocorrelation of up to a year, the climate variables have no significant autocorrelation, indicating that they can be described as white noise processes. The dashed black line displays an exponential function with an e-folding decay time of 8 years.

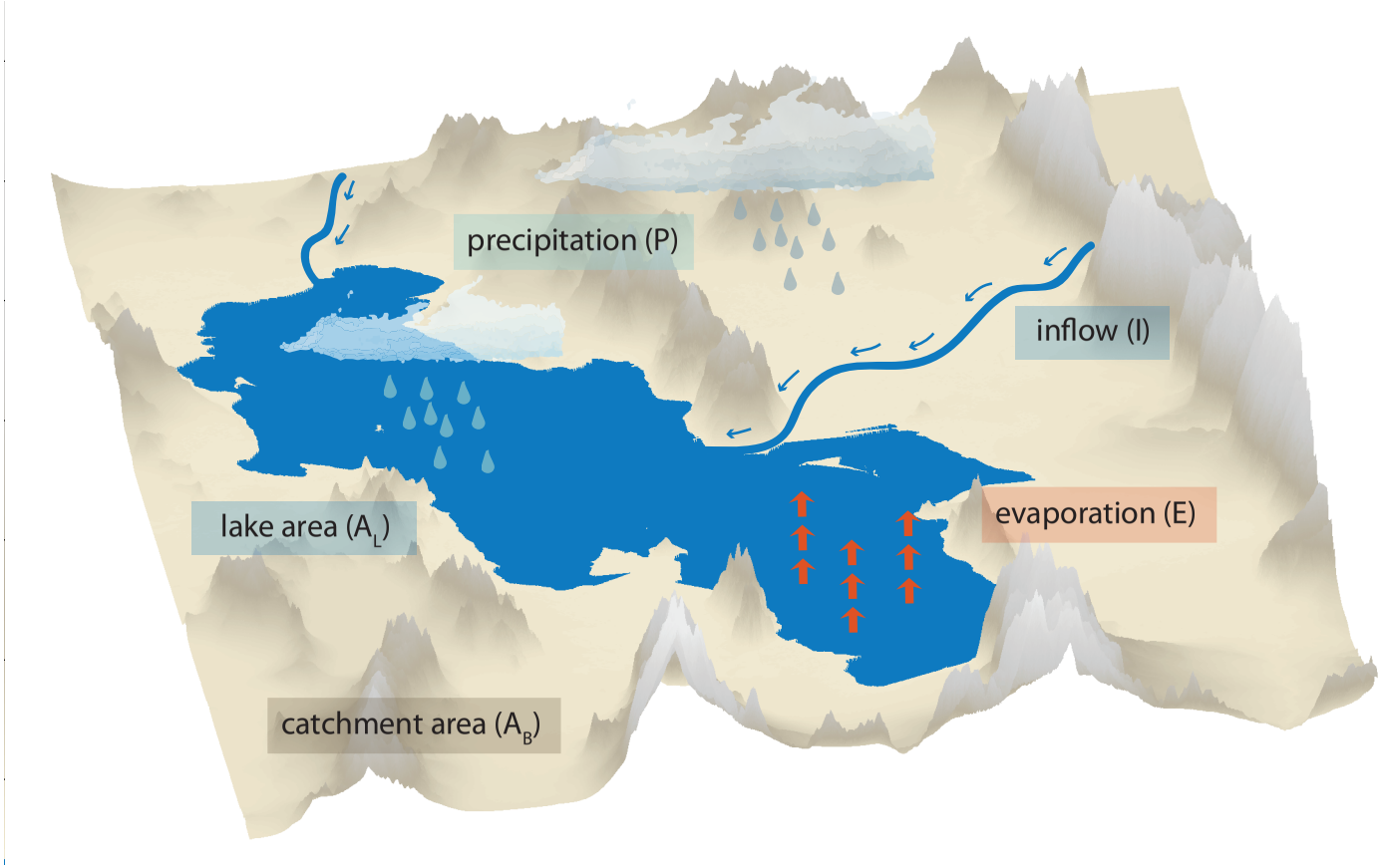

Figure 4.4: Schematic of inputs into the full and linear models. The lake gains volume from both direct precipitation into the lake and from river runoff, which we set as a fixed percentage of the precipitation that falls into the basin. All water loss is due to evaporation.

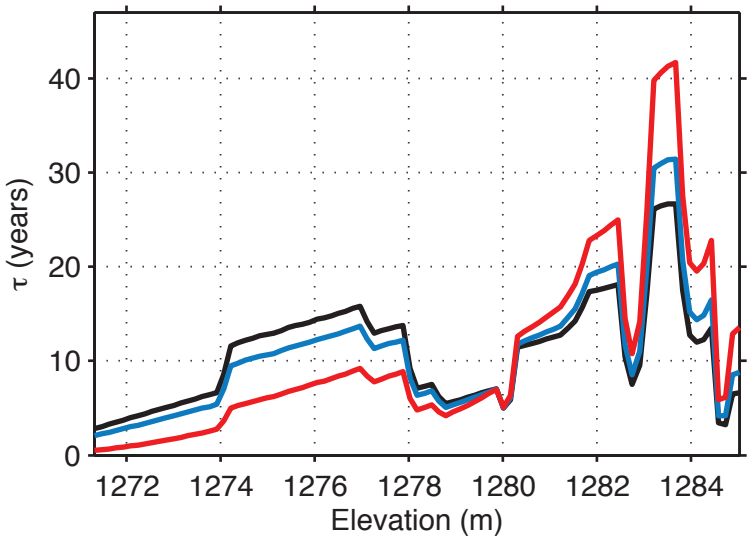

Figure 4.5: The e-folding timescale of the GSL, τ, calculated from Eq. 4.9, for different lake-level elevations. Each $\bar{h}$ corresponds to a specific $\bar{A}_L$ and $\frac{d\bar{A}_L}{dh}$. The black curve holds $\bar{E}$ and $\bar{P}$ constant, varying only $\bar{h}$ and its associated $\bar{A}_L$ and $\frac{d\bar{A}_L}{dh}$ to vary. However, from eq. (4.9), a change in the mean precipitation or evaporation affects τ directly, as a parameter in the equation, and indirectly, by modifying the mean area of the lake. The blue curve holds $\bar{E}$ constant, and associates an increase (decrease) in $\bar{P}$ with an increase (decrease) in lake level and lake area, providing a more physically consistent range of values for τ. Similarly, the red curve holds $\bar{P}$ constant, and associates an increase (decrease) in $\bar{E}$ with a decrease (increase) in lake level and lake area.

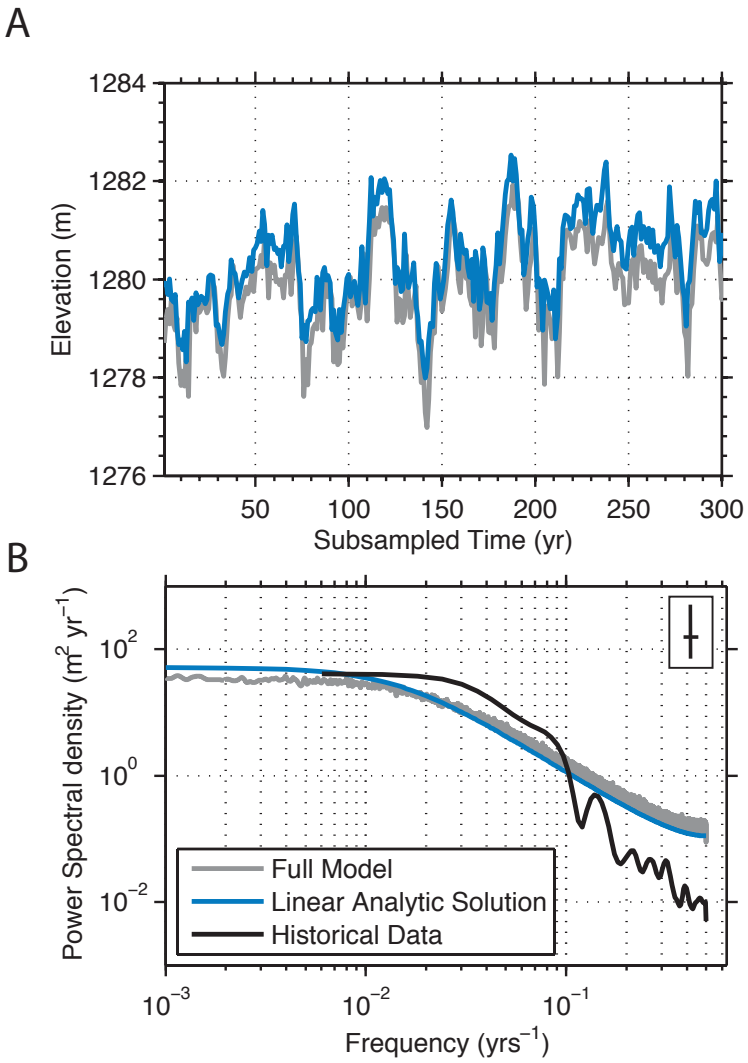

Figure 4.6: Long-term climate statistics. **A**: A 300-yr time slice of the full (grey) and linear (blue) lake-level model output, forced by stochastic variations in precipitation and evaporation. The two models are highly correlated ($r = 0.89$). **B**: The power spectra of the models and historical data (in black). The linear curve is calculated following Box et al. [2013]. The full model's spectrum was computed with a Hanning Window length of ten-thousand, with no overlap between the windows. The historical data's error bar is shown in the top right corner, with the horizontal line marking the intersection with the curve. Because full model was run for a million time steps, its error is negligible. The models capture variability well on timescales of decades or longer, but overestimate the variability at higher frequencies.

Figure 4.7: The distribution of lake level (**A**) and lake area (**B**) for the long-term forcing experiments. The linear model is outlined in black, and full model is represented with the bars that are filled in. Only the linear lake-level model output is normally distributed. **C** and **D**: The areas associated with $\pm 3\sigma_h$ for the full model run.

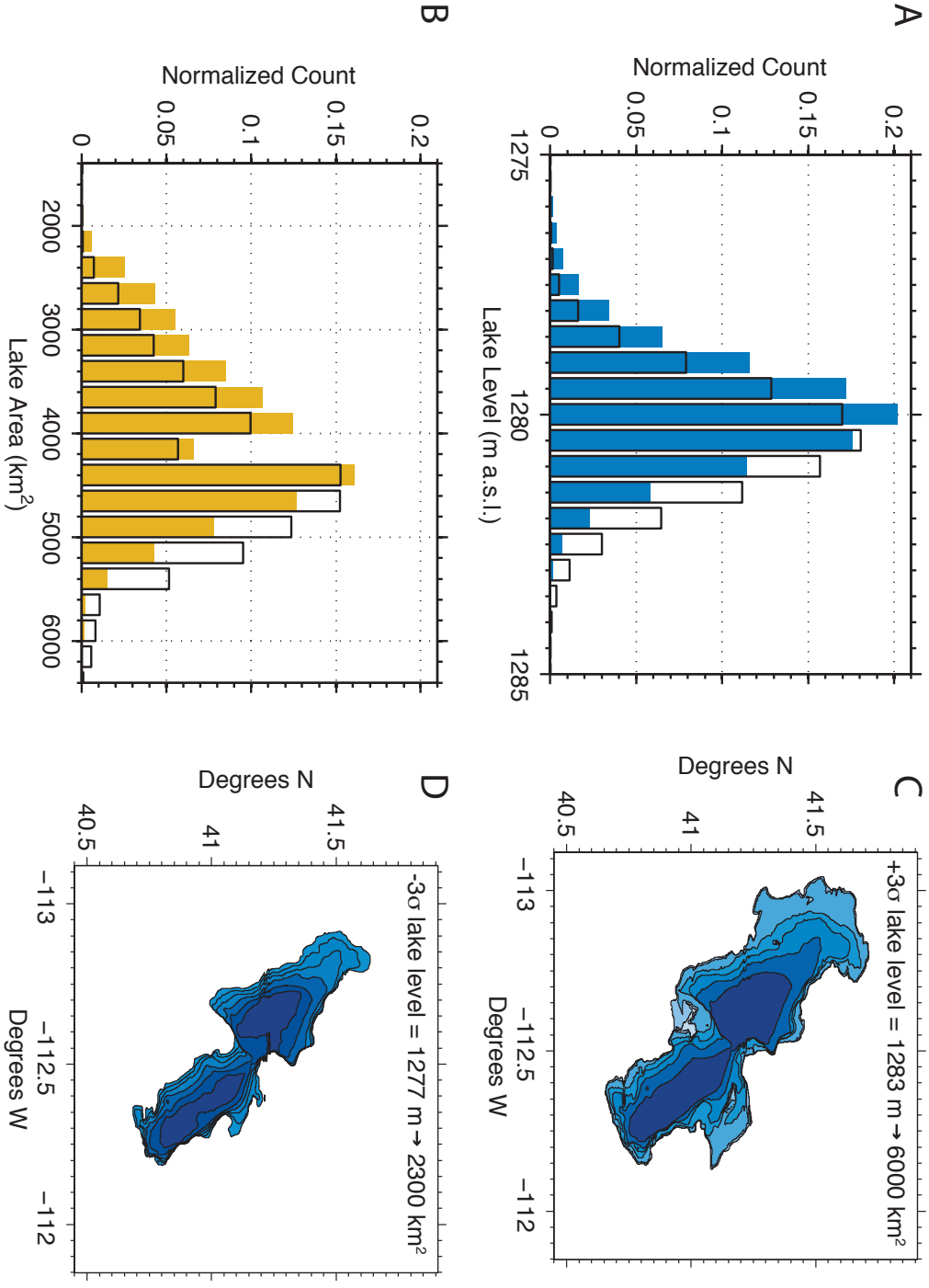
A
Normalized Count
0
0.05
0.1
0.15
0.2
1275
1280
1285
Lake Level (m a.s.l.)
B
Normalized Count
0
0.05
0.1
0.15
0.2
2000
3000
4000
5000
6000
Lake Area (km2)
C
+3σ lake level = 1283 m → 6000 km2
Degrees N
40.5
41
41.5
−113
−112.5
−112
Degrees W
D
-3σ lake level = 1277 m → 2300 km2
Degrees N
40.5
41
41.5
−113
−112.5
−112
Degrees W

Figure 4.8: The maximum and minimum lake-level excursions from the mean for random 1000, 500, and 100 year time-slices within the long-term model runs. The solid lines show the probability of a given excursion for the full model, while the dashed lines show the analytic solutions to the linear model. The dashed lines are symmetric about zero, while the solid lines' asymmetry reflects the effect of the lake's varying hypsometry. **B**: The total excursion probability in a given 1000, 500, and 100 year time-slices of the full model.

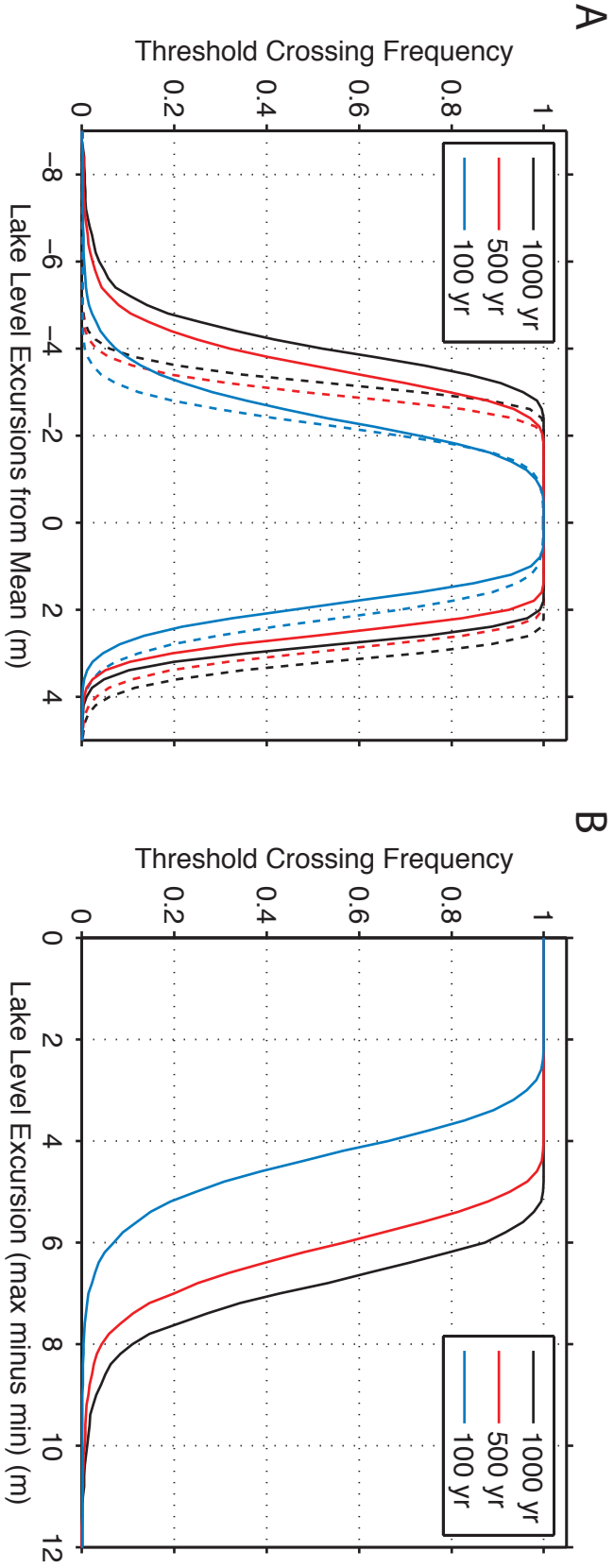
A
Threshold Crossing Frequency
0
0.2
0.4
0.6
0.8
1
−8
−6
−4
−2
0
2
4
Lake Level Excursions from Mean (m)
1000 yr
500 yr
100 yr
B
Threshold Crossing Frequency
0
0.2
0.4
0.6
0.8
1
0
2
4
6
8
10
12
Lake Level Excursion (max minus min) (m)
1000 yr
500 yr
100 yr

Figure 4.9: Alternative geometry experiments. The simplified geometries (shown in color) for the Great Salt Lake (**A**) Lake Titicaca (**B**), and Lake Bosumtwi (**C**), over their hypsometric curves (shown in black). The hypsometric curves are interpolated from Turner et al. [1996] (Bosumtwi) and Richerson et al. [1977] (Titicaca). The crosses mark the present-day lake levels for each of the lakes. Schematics of the frustum and half-ellipsoid shapes are shown to the left of each curve. **D**: A 2000-yr time slice from the long-term alternative lake model runs, showing the diverging behavior of the three lakes. **E**: The power spectra of the lakes. The full models are noisier, while the analytic solutions to the linear model are overlain above.

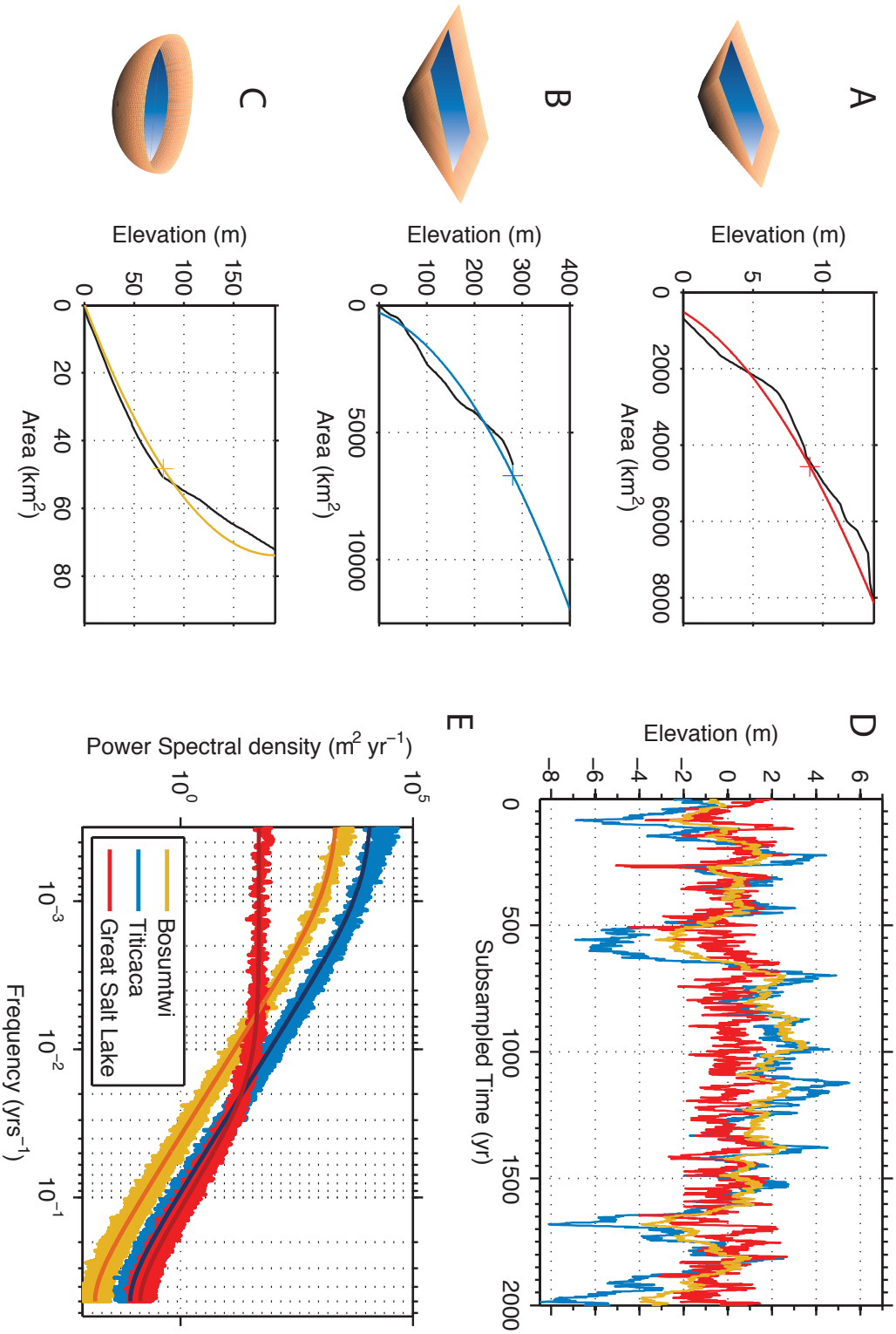
A
B
C
Elevation (m)
Area (km^2)
D
Elevation (m)
Subsampled Time (yr)
E
Power Spectral density (m^2 yr^{-1})
Frequency (yrs^{-1})
Bosumtwi
Titicaca
Great Salt Lake

Chapter 5

BASAL TOPOGRAPHIC CONTROLS ON THE LONG-TERM STABILITY OF THE WEST ANTARCTIC ICE SHEET

Chapter 5, in full, is currently being prepared for publication as "Basal topographic controls on the long-term stability of the West Antarctic Ice Sheet" authored by K. Huybers, G. H. Roe, and H. Conway. The dissertation author was the primary investigator and author of this paper.

5.1 Introduction

The total potential global sea-level contribution from the West Antarctic Ice Sheet (WAIS) is ∼4.3 m [Fretwell et al., 2013], and recent work suggests that Antarctica could contribute 0.15 to 0.62 m of sea-level rise in the next century [Solomon et al., 2007, Pfeffer et al., 2008, Joughin et al., 2010, Gladstone et al., 2012, Mouginot et al., 2014, Joughin et al., 2014]. However projections of the stability of the WAIS are hampered by the complexity of ice/ocean dynamics and uncertainty in the current and projected environmental changes [Joughin and Alley, 2011, Nowicki et al., 2013]. Here, we combine new observations of ice-thickness, basal topography, and surface velocity [Rignot et al., 2008, 2011, Fretwell et al., 2013] with advances in theoretical understanding of ice-sheet-shelf-ocean interactions [Schoof, 2007, Gagliardini et al., 2010, Drouet et al., 2012] to gain perspective on the stability of the WAIS, using a simple numerical model. Results show that differences in the basal relief beneath present-day ice streams will cause the Weddell, Amundsen, and Ross Sea sectors of Antarctica to respond with varying sensitivity to similar environmental perturbations.

In steady state, the flux of ice from the margins of the ice sheet is balanced by the accumulation rate integrated over the upstream catchment area. In reality, because the ice sheet is never truly in steady state, the mass balance of the ice sheet is mainly controlled by changes in the activity of fast-flowing outlet glaciers and ice streams. These outlet glaciers respond to changing conditions at the grounding line, the transition between the grounded ice sheet and the floating ice shelf. The grounding line, in turn, is highly sensitive to changes in sea-level and the melting/freezing of buttressing ice shelves [Payne et al., 2004, Joughin et al., 2010, Pritchard et al., 2012, Shepherd et al., 2012].

5.2 Model

Schoof [2007] provided an elegant theory for calculating the flux of ice across grounding lines. With several simplifying assumptions, the flux per unit width across a grounding line, $q(x_g)$, can be approximated by:

$$q(x_g) = \left[\frac{\bar{A}(\rho_i g)^{n+1}(1-\frac{\rho_i}{\rho_w})^n}{4^n C}\right]^{\frac{1}{m+1}} \theta^{\frac{n}{m+1}} H_g^{\frac{m+n+3}{m+1}} \tag{5.1}$$

where x is the distance along a flowline, $\rho_{i,w}$ are the densities of ice and sea water, respectively, g is the acceleration due to gravity, $\bar{A}$ is the depth-averaged temperature-dependent rheological parameter in Glen's flow law, and n is the corresponding exponent on the shear stress. C and m are parameters used to relate the basal shear stress and sliding speed: $\tau_b = C|u_b|^{m-1}u_b$. H_g is the ice-thickness at the grounding line. Values of θ, which parametrizes the effects of ice-shelf buttressing on the longitudinal stress gradients, vary between 0 (fully buttressed) and 1 (no buttressing). In reality, changes in buttressing depend on the evolution of the geometry of the surrounding ice shelf; caution is needed when applying the correction factor θ to parametrize the

evolution of buttressing.

Model parameters representing ice flow and sliding models are not well constrained, but values of $n = 3$, and $\bar{A} = 10^{-25}$ s^{-1} Pa^{-3} (appropriate for depth-averaged temperatures of -20°C) are reasonable for ice streams [Cuffey and Paterson, 2010]. Reported values for C vary by more than an order of magnitude, ranging from $\sim 6 \times 10^5$ Pa s$^{1/3}$ m$^{-1/3}$ for the fast-flowing Siple Coast ice streams to 10^7 Pa s$^{1/3}$ m$^{-1/3}$ (where $m = 1/3$) for basally resisted ice streams [Cuffey and Paterson, 2010]. Values for the sliding parameter, m, range from 1/3 for ice that is resisted laterally to 4 for basally-resisted ice. For this range of m, the exponent on H_g varies from 2 to 4.75. Thus, in terms of fractional changes, $q(x_g)$ is much more sensitive to H_g than to either buttressing (θ, exponent of 0.6 to 2.25) or flow and sliding parameters (A and C, exponent of 0.2 to 0.75).

For simplicity, hereafter we adopt a value of $m = 1/3$ for the entire model domain; higher values of m increase the importance of H_g relative to other variables, making 1/3 a conservative choice for sensitivity tests. Eq. (5.1) has been used for several modeling experiments [Pollard and DeConto, 2009, Docquier et al., 2011], and is broadly supported by comparisons to numerical models with idealized geometries [Pattyn et al., 2012]. The power-law dependence on H_g in Eq. (5.1) has a similar exponent to earlier theoretical work [Lingle, 1984].

Assuming hydrostatic equilibrium at the grounding line, the dominant term H_g is:

$$H_g = -z_b \frac{\rho_w}{\rho_i} \tag{5.2}$$

where z_b is the bed elevation above sea level. Thus Eqs. (5.1) and (5.2) suggest that $q(x_g) \sim z_b^{2\,to\,5}$ The acute sensitivity of the flux to changes of z_b emphasizes the importance of basal topography in the vicinity of the grounding line as a first order control on discharge from the ice sheet. Although the importance of basal topography (in particular for marine ice-sheets where the bed deepens inland) has been widely recognized [e.g. Weertman, 1974, Lingle, 1984, Schoof, 2007, Cofaigh et al., 2008, Pollard and DeConto, 2009] here for the first time we characterize the orographic sensitivity of the major outlet glaciers and ice streams in the Weddell, Ross and Amundsen Sea sectors to changes of accumulation rate, sea level, and buttressing.

Ice flow upstream from the grounding line is described using a dynamic 1.5-D flowband model (Eq. D.1 in Appendix D); the grounding line position adjusts to perturbations so that $q(x_g)$ matches the integrated upstream flux. We first consider the sensitivity of Foundation Ice Stream (FIS) in the Weddell Sea sector to changes in accumulation rate, sea level, and buttressing at the grounding line then generalize the results to other outlet glaciers and ice streams.

The upper catchment of FIS is located in East Antarctica, but the ice stream flows through West Antarctica and discharges into the Filchner-Ronne Ice Shelf (Fig. 5.5). Like many of the ice streams in the Weddell Sea sector, the grounding line of the FIS lies in a deep (up to 1900 m below sea level) trench, which extends around the embayment and shoals gently out to the edge of the continental shelf [Ross et al., 2012, Fretwell et al., 2013]. Basal relief just inland of the FIS grounding line rises 1400 m over 150 km (Fig. 5.2). Values for the sliding law C (8×10^6 Pa $s^{1/3}$ $m^{-1/3}$) and $\theta = 0.2$ were chosen to match the modern surface elevation profile and grounding line position, respectively. Tuning θ in this way assumes that the ice stream is now in equilibrium, which is consistent with our recent results from cosmogenic exposure-age dating that indicate the ice stream has not thinned over the past 4,000 yr (Balco, G.,

pers. communication). Figure 5.2 shows that the mismatch between the modeled and observed present-day profile and the grounding-line position is small. Discrepancies are most likely due to spatial variations in bed conditions and ice-flow parameters.

5.3 Results: Foundation Ice Stream

In all experiments, $\bar{A}$, C, and m were kept constant. Results are for steady-state conditions; we do not show transient states. Elevations throughout the text are referenced to the modern sea level, and are not corrected for isostatic adjustments or local gravitational effects [Gomez et al., 2010]. We caution that the calculations are not intended as projections, and it should be recognized that parametrizations of deformation and sliding are uncertain and full thermo-mechanical details are not included. Rather, our results are a quantitative demonstration of the physical principles embodied in Eqs. (5.1), (5.2), (D.1), and (D.2).

The location of the FIS grounding line within an asymmetrical trough is key to its current stability with respect to retreat: relatively small changes in the grounding-line position can accommodate large changes in ice flux. While the modern FIS geometry suggests it is stable to retreat, we note that the long reverse slope seaward of the present-day grounding line cannot sustain a stable grounding-line position, implying that the FIS is relatively unstable to advances, and that during glacial periods the grounding line could readily push well beyond its present location, advancing to the edge of the continental shelf. This is corroborated by marine-geological evidence [Hillenbrand et al., 2012], and other modeling efforts [Whitehouse et al., 2012, Stolldorf et al., 2012], and by glacial geologic data from the Williams Hills 50 km upstream from the grounding line, which show the a local ice stream thickening of was 500 m during the Last Glacial Maximum (LGM) (Balco, G., *pers. communication*).

5.3.1 Retreats

First, we consider forcings that would cause the grounding line of the FIS to retreat. A sea-level increase of 100 m, which approximates the difference in sea-level from the present to the LGM, though presently unrealistically large, requires only a 5 km grounding line retreat to restore balance (Fig. 5.2, dashed red line). The steep basal topography inland of the grounding line can accommodate this change over relatively short horizontal scales, and is accompanied by very little change in ice thickness.

Halving the upstream accumulation rate is balanced by a grounding-line retreat of only $\sim$ 18 km (Fig. 5.2, yellow line). In contrast to sea-level rise, the reduced accumulation causes considerable interior thinning that averages 180 m over the domain of the grounded ice.

The complete removal of buttressing by setting $\theta = 1$ in Eq. (5.1) causes the largest change of all parameters considered. The grounding line retreats $\sim$300 km before re-stabilizing near the edge of the trench, and the interior thins, reducing the volume of ice by 28% (Fig. 5.2, dark grey line). Smaller changes in buttressing have less of an effect – setting $\theta = 0.5$ causes the grounding line to retreat by only 75 km, with an ice-volume loss of approximately 5% (Fig. 5.2, dashed grey line).

5.3.2 Advances

Because the FIS's grounding line presently lies in the deepest part of its domain, an increase in the flux cannot be accommodated by an advance in the grounding line to shallowing topography. Lowering the sea level by only 23 m (well above the LGM sea-level) or increasing the accumulation uniformly by 6% results in the modeled grounding line advancing to the edge of the continental shelf. Although not in any

way a projection – the interactions are far too uncertain – these calculations highlight how complex grounding-line dynamics might produce counter-intuitive consequences to warming. They serve as a quantitative demonstration of the physical principle embodied in Eq. (5.1): that a large change in forcing is necessary to induce a retreat from the trench in which the present-day grounding line resides, but a relatively small forcing is needed to advance the grounding line on a long, reverse-slope bed.

5.4 Discussion

Many of the other ice streams that flow into the Ronne-Filchner Ice Shelf are also grounded within the deep asymmetrical trench that rings the Weddell embayment. The Support-Force, Evans, Recovery, and Rutford ice streams all have beds that rise steeply inland immediately behind the present-day position of the grounding line (Fig. 5.5 and 5.3B, F, H, I), implying that they are also are strongly stable to plausible future sea-level rise or decreases in shelf buttressing. Moreover, with the exception of the Recovery Ice Stream, the bed generally shoals toward the continental shelf, indicating the potential for expansion of the ice sheet when sea level lowered during glacial climates.

The grounding lines of Bailey, Institute, Slessor, and Möller Ice Streams (Fig. 5.5 and 5.3 C, D, E, and J) lie just beyond the regions main trench. For these ice streams, a relatively small external forcing may cause an initial grounding retreat on the order of $\sim$100 km, but stability would be re-acquired in the deep trenches. Note that the Slessor ice stream is currently grounded on a reverse slope; this potentially unstable position implies a more complex role for buttressing than is represented by Eq. (5.1). One possibility is lateral communication between adjacent ice streams through thickness changes on lightly grounded ice plains inferred by Hulbe and Fahnestock [2007].

In contrast, basal topography beneath the ice streams in the Ross Sea sector is muted (Fig. 5.5 and 5.4 A–E). Over regional scales (a few hundred kilometers), the ice streams are grounded on gentle reverse slopes that extend in both directions from the current grounding line. The large-scale basal topography suggests that both advances and retreats would be determined by the complex interplay of basal topography, external forcing factors, and influence from adjacent ice streams, mediated by ice-shelf buttressing and competition for upstream catchment area. Further, thermomechanical feedbacks that control basal sliding of the Ross ice streams [Raymond, 1996] may lead to stagnation and reactivation of flow over century scales [Hulbe and Fahnestock, 2007] and even switches of flow direction [Conway et al., 2002], adding complexity to projections of future behaviors. In addition, even small-scale sea mounts and lateral buttressing from inter-stream ridges along the Siple Coast will influence grounding-line advance and retreat [Gagliardini et al., 2010, Drouet et al., 2012].

The Amundsen Sea sector is currently well out of balance (-64 Gt yr^{-1}, Rignot et al. [2008]). Further, the current grounding lines of Thwaites and Pine Island Glaciers are positioned at the edge of an over-deepening that extends below sea level more than 400km inland (Fig. 5.5 and 5.4F, G). If the current rates of melting and disintegration of surrounding ice shelves continues [Pritchard et al., 2012], the glaciers could retreat episodically past bedrock bumps more than 300 km inland.

5.5 Conclusions

Making quantitative projections of the future of the WAIS or understanding in detail the cause of its past changes is an enormously difficult challenge, depending as it does on modeling numerous subtle and complex interactions. It is yet to be established that such projections are a tractable goal, even in principle. However, recent theory and data sets imply that differences in large-scale basal topography will cause the

Weddell, Amundsen, and Ross Sea sectors of Antarctica to respond differently to the same environmental forcing. The acute functional sensitivity of grounding-line flux to basal topography ($q(x_g) \sim z_b^{2\,to\,5}$), implies that even small topographic ridges can provide a local anchor for the grounding line, even if the larger-scale topography is a reverse slope Schoof [2007]. Our evaluation reaffirms that the greatest concerns for WAIS retreat are locations of reverse slopes, muted basal topography, and limited lateral support. While predictive skill from numerical models is yet to be ascertained, the physical principles embodied in Eq. (5.1) and the geometrical constraints available from modern data sets form a basis for selecting and prioritizing the locations of the intensive campaigns to observe modern trends and reconstruct past history that offer the surest path to progress.

Figure 5.1: Major West Antarctic ice stream catchment areas, outlined in black (data from Joughin, I., *pers. communication*). A characteristic flowline for each catchment area [from Byrd Polar Research Center] is overlain on Antarctica's bed elevation [Fretwell et al., 2013]. The flowline routing beyond the present-day ice shelf extent is drawn as a continuation of the flowline. Brown colors indicate elevations above the present-day sea-level, and blue colors indicate elevations below sea-level. The transition from a solid to pixelated area marks the edge of the continental shelf.

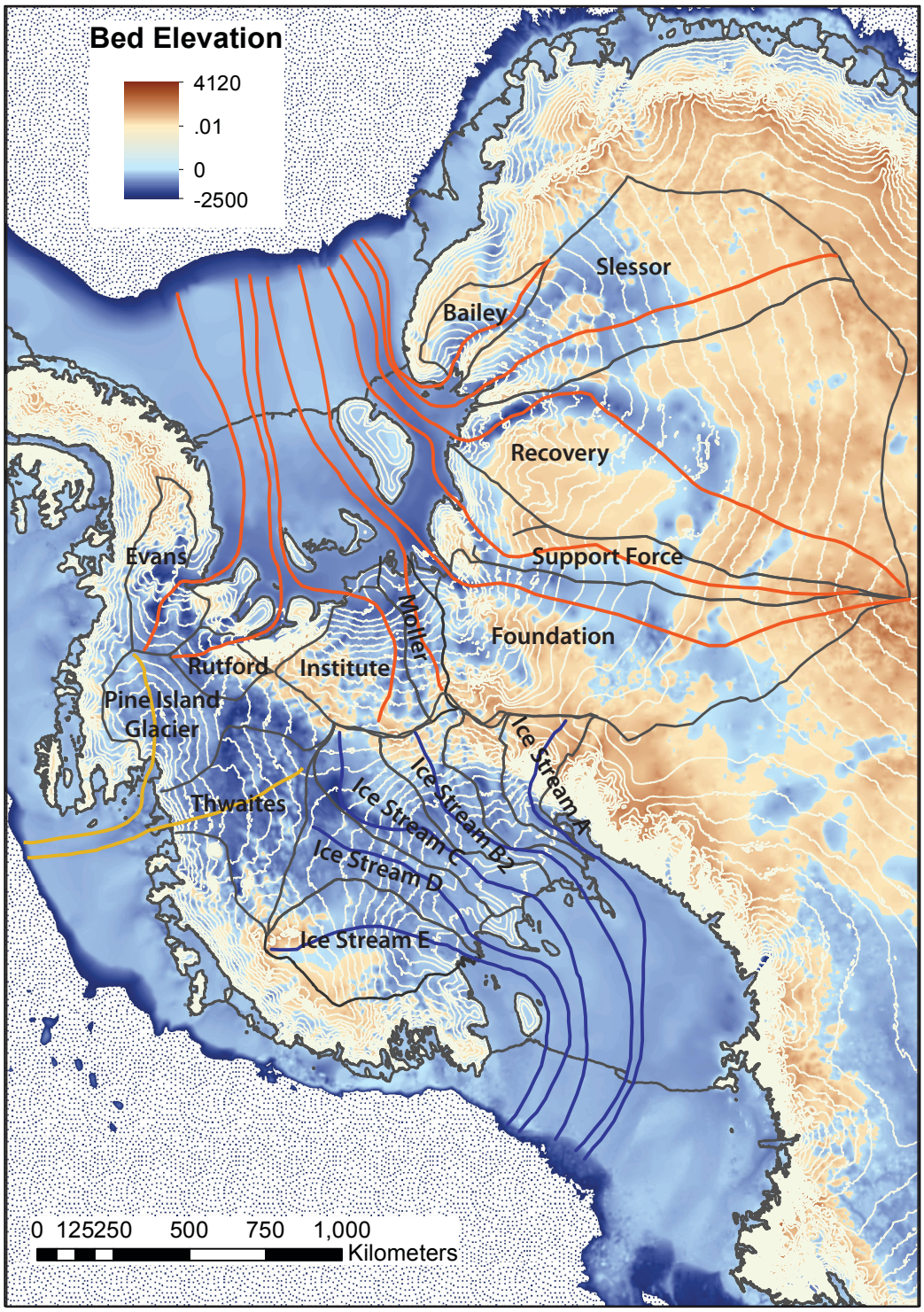
Bed Elevation
4120
.01
0
-2500
Slessor
Bailey
Recovery
Support Force
Foundation
Evans
Rutford
Institute
Möller
Pine Island Glacier
Thwaites
Ice Stream A
Ice Stream B2
Ice Stream C
Ice Stream D
Ice Stream E
0 125250 500 750 1,000
Kilometers

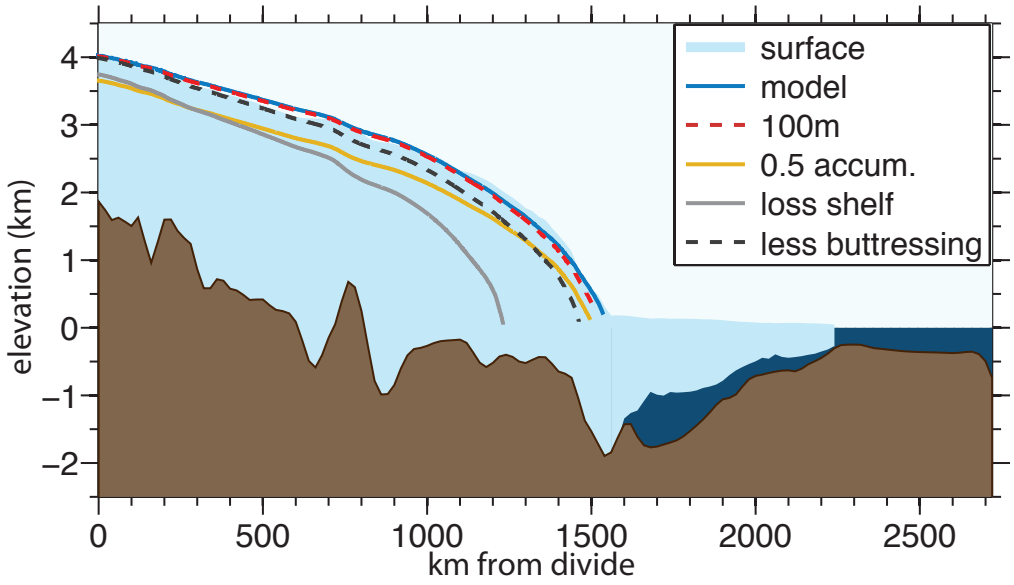

Figure 5.2: Foundation Ice Stream profile and modelling results. The FIS flowline from Fig. 5.5 is interpolated onto the BEDMAP2 surface elevation, bed elevation, and thickness data [Fretwell et al., 2013], with the profile shown in solid colors. The bed topography has been smoothed for visual clarity, but was kept at a 1-km grid-spacing for the model runs. The blue curve shows the initial steady-state model profile ($C = 8 \times 10^6$ Pa $s^{1/3}$ $m^{-1/3}$, $\theta = 0.2$). The other curves show the FIS's new steady-state profile, under different environmental constraints: if sea-level is raised by 100 m (red dashed curve); half of the present-day accumulation (yellow curve): no ice shelf buttressing (solid grey curve); and $\theta = 0.5$ (dashed grey curve).

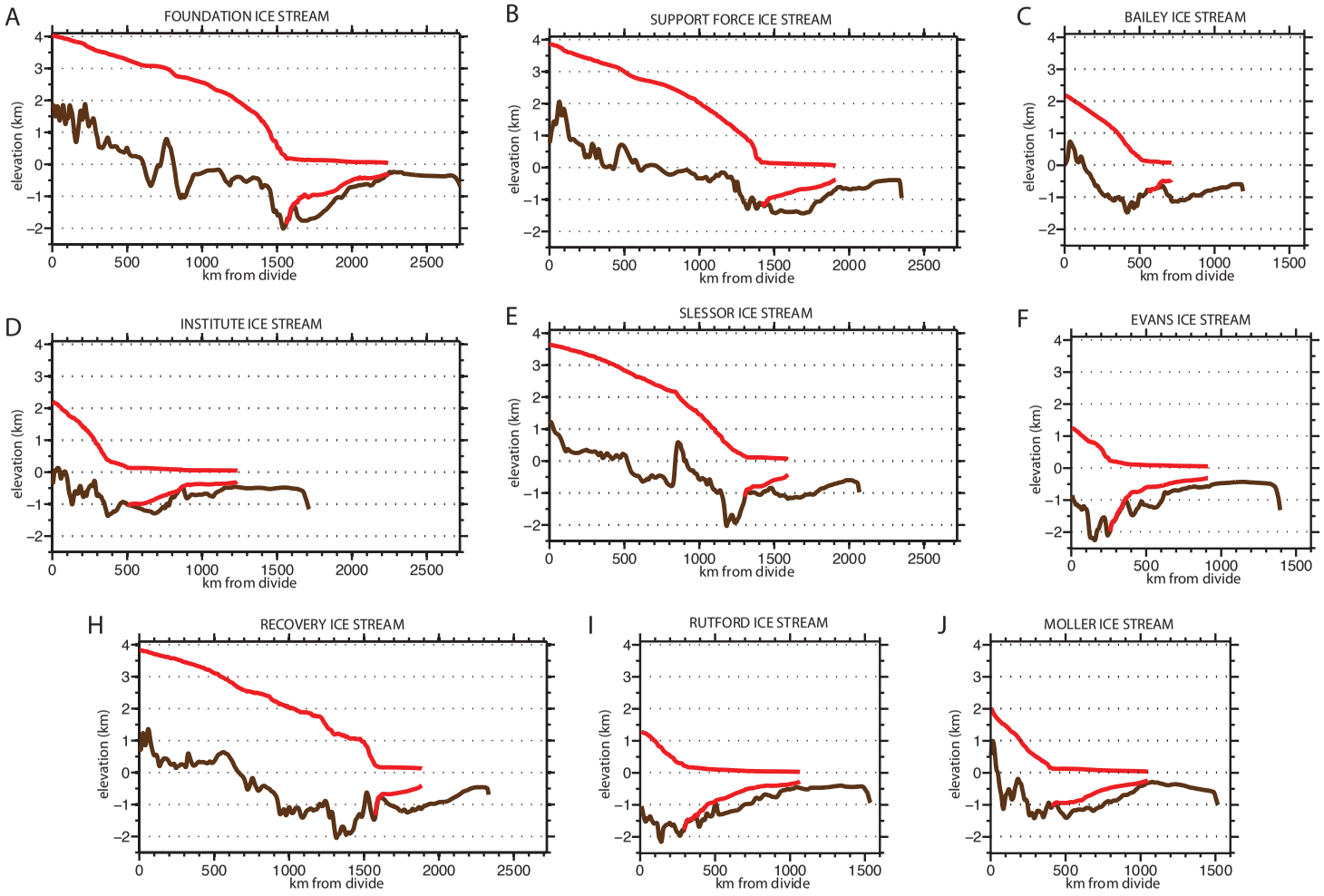

Figure 5.3: Weddell-Sea sector ice stream and bed profiles, from Fig. 5.5, interpolated onto the BEDMAP2 surface elevation, bed elevation, and thickness data [Fretwell et al., 2013].

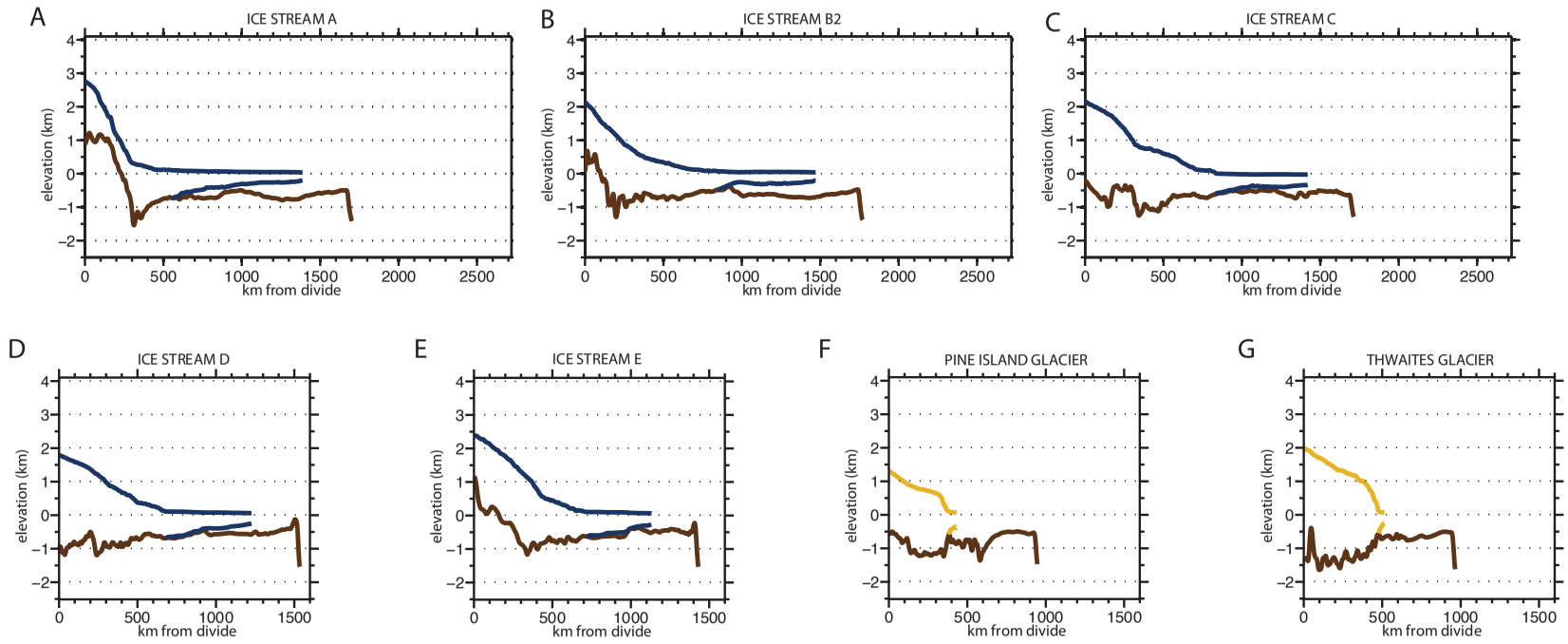

Figure 5.4: Ross-Sea sector (blue) and Amundsen-Sea (yellow) sector ice stream and bed profiles, from Fig. 5.5, interpolated onto the BEDMAP2 surface elevation, bed elevation, and thickness data [Fretwell et al., 2013].

Chapter 6
CONCLUSIONS

I have shown that appropriately formulated simple models can capture the essential climate-response characteristics of geophysical systems, and as a result, are powerful tools for understanding how these systems record the climate that they experience. Though more comprehensive models may more skillfully recreate the paleo-record, and, presumably, predict future geophysical behavior more accurately, my approach allows for a transparent and complete understanding of the behaviors of the modeled systems. My work explores how glaciers, lakes, and ice streams respond to climatic and environmental variations and changes, and was defined by the following five questions:

1. *What climatic variables, represented by the climate proxy, are well preserved by the geophysical system?*

   Glaciers record variations in both accumulation, in the form of snowfall, and temperature, through ice melt. Lakes can record variations in both precipitation and evaporation. Analytic expressions were derived for both glaciers and lakes, to estimate the relative sensitivity to each of the climate variables that drive their variations. Ice-stream profiles are sensitive to sea level, accumulation, and buttressing provided by ice shelves. The topography of the underlying bedrock determines the how these environmental states are expressed in the ice-stream profile.

2. *On what timescale is climatic information well preserved?*

   The timescale of glacier-length and lake-level variations ranges from years to centuries. Roe and O'Neal [2009] derived a characteristic memory for glaciers, and Chapter 4 shows a similar derivation for the memory of a closed-basin lake. The transient ice-stream responses to environmental forcings were not considered in this work. However, it is clear that the memory of each system is at least partly determined by the orography or bathymetry that the glacier, lake, or ice stream rests upon.

3. *Over what spatial scale does the proxy represent relevant information?*

   The correlation in regional glacier advance and retreat is a function of correlation in regional precipitation and temperature – this was expressly addressed in Chapters 2 and 3. Similar work could be done for regional lake-level variability. My work in Chapter 5 shows how changes in the mean environment can give rise to dramatically different characteristic profiles for ice streams.

4. *How can one distinguish a climatic signal from noise in the proxy record?*

   For glaciers, my work showing idealized expected regional glacier-length correlations can be used to set a baseline expected for regional coherence in the proxy signal. A regional glacier signal that is more coherent than these baseline expectations would indicate a true regional change in either precipitation, temperature, or both. For lakes, I used statistical analysis to estimate the variability of lake levels in response to climate variability alone. I characterize Foundation

Ice Stream's mean response to different environmental states, providing limits to expected large-scale profile changes. Similar studies can be done with any ice stream or outlet glacier.

5. *What physics and parameters is the system most sensitive to?*

The primary sensitivity of each system is addressed in its respective chapter. Again, my idealized modeling approach allows for many experimental designs, making it relatively simple to examine the response to changes in the physics and parameters of the system, in comparison to the responses to environmental or climate forcings.

By capturing the general behavior of the system's response to climate change, these models provide context and insight into the interpretation of specific proxy records. Further, these models can be adapted to other lake, glacier, or ice-stream systems, affording a simple first-order insight into their response to climatic or environmental change. I pose the questions above in the service of framing the interpretation of paleo-climate records, as well as gaining a better understanding of the present and projected future behaviors of glaciers, lakes, and ice sheets.

BIBLIOGRAPHY

H. D. Abarbanel and U. Lall. Nonlinear dynamics of the Great Salt Lake: system identification and prediction. *Climate Dynamics*, 12(4):287–297, 1996.

H. D. Abarbanel, U. Lall, Y.-I. Moon, M. E. Mann, and T. Sangoyomi. Nonlinear dynamics and the Great Salt Lake: A predictable indicator of regional climate. *Energy*, 21(7):655–665, 1996.

A. M. Anders, G. H. Roe, D. R. Durran, and J. R. Minder. Small-scale spatial gradients in climatological precipitation on the Olympic Peninsula. *Journal of Hydrometeorology*, 8(5), 2007.

J. B. Anderson, S. S. Shipp, A. L. Lowe, J. S. Wellner, and A. B. Mosola. The Antarctic Ice Sheet during the Last Glacial Maximum and its subsequent retreat history: a review. *Quaternary Science Reviews*, 21(13):49 – 70, 2002. ISSN 0277-3791. doi: http://dx.doi.org/10.1016/S0277-3791(01)00083-X. URL `http://www.sciencedirect.com/science/article/pii/S027737910100083X`.

R. S. Anderson, P. Molnar, and M. A. Kessler. Features of glacial valley profiles simply explained. *Journal of Geophysical Research: Earth Surface (2003–2012)*, 111(F1), 2006.

T. Arnow. Water-level and water-quality changes in Great Salt Lake, Utah, 1843-1985. *US Geological Survey Circular*, 913, 1985.

T. Arnow and D. W. Stephens. Hydrologic characteristics of the Great Salt Lake, Utah, 1847-1986. *US Geological Survey Water-Supply Paper*, 2332, 1990.

G. Balco, J. O. Stone, N. A. Lifton, and T. J. Dunai. A complete and easily accessible means of calculating surface exposure ages or erosion rates from ^{10}Be and ^{26}Al measurements. *Quaternary Geochronology*, 3(3):174–195, 2008.

R. L. Baskin. Calculation of area and volume for the south part of Great Salt Lake, Utah. *US Geological Survey Open-File Report*, 20051327, 2005.

R. L. Baskin. Calculation of area and volume for the nouth part of Great Salt Lake, Utah. *US Geological Survey Open-File Report*, 20061359, 2006.

C. Bitz and D. Battisti. Interannual to decadal variability in climate and the glacier mass balance in Washington, western Canada, and Alaska. *Journal of Climate*, 12 (11), 1999.

G. E. Box, G. M. Jenkins, and G. C. Reinsel. *Time series analysis: forecasting and control*. John Wiley & Sons, 4th edition, 2013.

R. J. Braithwaite and Y. Zhang. Sensitivity of mass balance of five Swiss glaciers to temperature changes assessed by tuning a degree-day model. *Journal of Glaciology*, 46(152):7–14, 2000.

C. S. Bretherton, M. Widmann, V. P. Dymnikov, J. M. Wallace, and I. Blade. The effective number of spatial degrees of freedom of a time-varying field. *Journal of Climate*, 12(7), 1999.

Byrd Polar Research Center. Radarsat Antarctic mapping project, 1997. URL `www-bprc.mps.ohio-state.edu`.

T. Chinn, S. Winkler, M. Salinger, and N. Haakensen. Recent glacier advances in Norway and New Zealand: a comparison of their glaciological and meteorological causes. *Geografiska Annaler: Series A, Physical Geography*, 87(1):141–157, 2005.

P. U. Clark, A. S. Dyke, J. D. Shakun, A. E. Carlson, J. Clark, B. Wohlfarth, J. X. Mitrovica, S. W. Hostetler, and A. M. McCabe. The last glacial maximum. *Science*, 325(5941):710–714, 2009.

C. Ó. Cofaigh, J. A. Dowdeswell, J. Evans, and R. D. Larter. Geological constraints on Antarctic palaeo-ice-stream retreat. *Earth Surface Processes and Landforms*, 33 (4):513–525, 2008.

B. A. Colle, C. F. Mass, and K. J. Westrick. MM5 precipitation verification over the Pacific Northwest during the 1997-99 cool seasons. *Weather & Forecasting*, 15(6), 2000.

H. Conway, G. Catania, C. Raymond, A. Gades, T. Scambos, and H. Engelhardt. Switch of flow direction in an Antarctic ice stream. *Nature*, 419(6906):465–467, 2002.

K. M. Cuffey and W. S. B. Paterson. *The Physics of Glaciers*. Elsevier Science, 2010. ISBN 9780080919126. URL `http://books.google.com/books?id=FwQjngEACAAJ`.

D. Docquier, L. Perichon, and F. Pattyn. Representing grounding line dynamics in numerical ice sheet models: recent advances and outlook. *Surveys in Geophysics*, 32(4-5):417–435, 2011.

A. Drouet, D. Docquier, G. Durand, R. Hindmarsh, F. Pattyn, O. Gagliardini, and T. Zwinger. Grounding line transient response in marine ice sheet models. *The Cryosphere Discussions*, 6:3903–3935, 2012.

C. Frankignoul and K. Hasselmann. Stochastic climate models, part II: Application to sea-surface temperature anomalies and thermocline variability. *Tellus*, 29(4): 289–305, 1977.

P. Fretwell, H. D. Pritchard, D. G. Vaughan, J. Bamber, N. Barrand, R. Bell, C. Bianchi, R. Bingham, D. Blankenship, G. Casassa, et al. Bedmap2: improved ice bed, surface and thickness datasets for Antarctica. *Cryosphere*, 7(1), 2013.

O. Gagliardini, G. Durand, T. Zwinger, R. Hindmarsh, and E. Le Meur. Coupling of ice-shelf melting and buttressing is a key process in ice-sheets dynamics. *Geophysical Research Letters*, 37(14), 2010.

R. M. Gladstone, V. Lee, J. Rougier, A. J. Payne, H. Hellmer, A. Le Brocq, A. Shepherd, T. L. Edwards, J. Gregory, and S. L. Cornford. Calibrated prediction of Pine Island Glacier retreat during the 21st and 22nd centuries with a coupled flowline model. *Earth and Planetary Science Letters*, 333:191–199, 2012.

N. Gomez, J. X. Mitrovica, P. Huybers, and P. U. Clark. Sea level as a stabilizing factor for marine-ice-sheet grounding lines. *Nature Geoscience*, 3(12):850–853, 2010.

G. A. Grell, J. Dudhia, D. R. Stauffer, et al. A description of the fifth-generation Penn State/NCAR mesoscale model (MM5). *Mesoscale and Microscale Meteorology Division, National Center for Atmospheric Research*, 1994.

A. F. Hamlet, P. W. Mote, M. P. Clark, and D. P. Lettenmaier. Effects of temperature and precipitation variability on snowpack trends in the western United States. *Journal of Climate*, 18(21), 2005.

J. T. Harper. The dynamic response of glacier termini to climatic variation during the period 1940-1990 on Mount Baker, Washington, USA. Master's thesis, Western Washington University, 1992.

J. T. Harper. Glacier terminus fluctuations on Mount Baker, Washington, USA, 1940-1990, and climatic variations. *Arctic and Alpine Research*, pages 332–340, 1993.

A. Harrison. Fluctuations of Coleman Glacier, Mt Baker, Washington, USA. *Journal of Glaciology*, 9:393–396, 1970.

W. Harrison. How do glaciers respond to climate? Perspectives from the simplest models. *Journal of Glaciology*, 59(217):949–960, 2013.

W. Harrison, D. Elsberg, K. Echelmeyer, and R. Krimmel. On the characterization of glacier response by a single time-scale. *Journal of Glaciology*, 47(159):659–664, 2001.

K. Hasselmann. Stochastic climate models part I: Theory. *Tellus*, 28(6):473–485, 1976.

C.-D. Hillenbrand, M. Melles, G. Kuhn, and R. D. Larter. Marine geological constraints for the grounding-line position of the Antarctic Ice Sheet on the southern Weddell Sea shelf at the Last Glacial Maximum. *Quaternary Science Reviews*, 32: 25–47, 2012.

S. M. Hodge, D. C. Trabant, R. M. Krimmel, T. A. Heinrichs, R. S. March, and E. G. Josberger. Climate variations and changes in mass of three glaciers in western North America. *Journal of Climate*, 11(9), 1998.

C. Hulbe and M. Fahnestock. Century-scale discharge stagnation and reactivation of the Ross ice streams, West Antarctica. *Journal of Geophysical Research: Earth Surface (2003–2012)*, 112(F3), 2007.

K. Hutter. *Theoretical glaciology: material science of ice and the mechanics of glaciers and ice sheets*. Reidel, 1983.

K. Hutter, F. Legerer, and U. Spring. First-order stresses and deformations in glaciers and ice sheets. *Journal of Glaciology*, 27:227–270, 1981.

K. Huybers and G. H. Roe. Spatial patterns of glaciers in response to spatial patterns in regional climate. *Journal of Climate*, 22(17), 2009.

P. Huybrechts and J. de Wolde. The dynamic response of the Greenland and Antarctic ice sheets to multiple-century climatic warming. *Journal of Climate*, 12(8), 1999.

T. Jóhannesson, C. Raymond, and E. Waddington. Time-scale for adjustment of glaciers to changes in mass balance. *Journal of Glaciology*, 35(121):355–369, 1989.

I. Joughin and R. B. Alley. Stability of the West Antarctic ice sheet in a warming world. *Nature Geoscience*, 4(8):506–513, 2011.

I. Joughin and J. L. Bamber. Thickening of the ice stream catchments feeding the Filchner-Ronne Ice Shelf, Antarctica. *Geophysical Research Letters*, 32(17), 2005.

I. Joughin, B. E. Smith, and D. M. Holland. Sensitivity of 21st century sea level to ocean-induced thinning of Pine Island Glacier, Antarctica. *Geophysical Research Letters*, 37(20), 2010.

I. Joughin, B. E. Smith, and B. Medley. Marine ice sheet collapse potentially under way for the Thwaites Glacierbasin, West Antarctica. *Science*, 344(6185):735–738, 2014. doi: 10.1126/science.1249055.

T. R. Karl and P. J. Young. Recent heavy precipitation in the vicinity of the Great Salt Lake: Just how unusual? *Journal of Climate and Applied Meteorology*, 25(3): 353–363, 1986.

M. A. Kessler, R. S. Anderson, and G. M. Stock. Modeling topographic and climatic control of east-west asymmetry in Sierra Nevada glacier length during the Last Glacial Maximum. *Journal of Geophysical Research: Earth Surface (2003–2012)*, 111(F2), 2006.

G. Kite. Use of time series analysis to detect climatic change. *Journal of Hydrology*, 111(1):259–279, 1989.

M. Kuhle. Topography as a fundamental element of glacial systems. *GeoJournal*, 17 (4):545–568, 1988.

U. Lall and M. Mann. The Great Salt Lake: A barometer of low-frequency climatic variability. *Water Resources Research*, 31(10):2503–2515, 1995.

U. Lall, T. Sangoyomi, and H. D. Abarbanel. Nonlinear dynamics of the Great Salt Lake: Nonparametric short-term forecasting. *Water Resources Research*, 32(4): 975–985, 1996.

W. B. Langbein. The salinity and hydrology of closed lakes. *US Geological Survey Professional Paper*, 412, 1961.

A. M. Le Brocq, A. J. Payne, and A. Vieli. An improved Antarctic dataset for high resolution numerical ice sheet models (ALBMAP v1). *Earth System Science Data Discussions*, 3(1):195–230, 2010.

D. R. Legates and C. J. Willmott. Mean seasonal and spatial variability in gauge-corrected, global precipitation. *International Journal of Climatology*, 10(2):111–127, 1990a.

D. R. Legates and C. J. Willmott. Mean seasonal and spatial variability in global surface air temperature. *Theoretical and Applied Climatology*, 41(1-2):11–21, 1990b.

G. Leysinger-Vieli and G. Gudmundsson. On estimating length fluctuations of glaciers caused by changes in climatic forcing. *Journal of Geophysical Research: Earth Surface (2003–2012)*, 109(F1), 2004.

C. S. Lingle. A numerical model of interactions between a polar ice stream and

the ocean: Application to ice stream E, West Antarctica. *Journal of Geophysical Research: Oceans (1978–2012)*, 89(C3):3523–3549, 1984.

B. L. Loving, K. M. Waddell, and C. W. Miller. Water and salt balance of Great Salt Lake, Utah, and simulation of water and salt movement through the causeway, 1987-98. *US Geological Survey Water-Resources Investigations Report*, 00-4221, 2000.

D. R. MacAyeal. Irregular oscillations of the West Antarctic ice sheet. *Nature*, 359 (6390):29–32, 1992.

M. E. Mann, U. Lall, and B. Saltzman. Decadal-to-centennial-scale climate variability: Insights into the rise and fall of the Great Salt Lake. *Geophysical Research Letters*, 22(8):937–940, 1995.

N. J. Mantua and S. R. Hare. The Pacific Decadal Oscillation. *Journal of Oceanography*, 58(1):35–44, 2002.

N. J. Mantua, S. R. Hare, Y. Zhang, J. M. Wallace, and R. C. Francis. A Pacific interdecadal climate oscillation with impacts on salmon production. *Bulletin of the American Meteorological Society*, 78(6):1069–1079, 1997.

I. Mason, M. Guzkowska, C. Rapley, and F. Street-Perrott. The response of lake levels and areas to climatic change. *Climatic Change*, 27(2):161–197, 1994.

C. F. Mass, M. Albright, D. Ovens, R. Steed, M. MacIver, E. Grimit, T. Eckel, B. Lamb, J. Vaughan, K. Westrick, et al. Regional environmental prediction over the Pacific Northwest. *Bulletin of the American Meteorological Society*, 84(10), 2003.

K. Matsuura and C. Willmott. Terrestrial precipitation: 1900-2010 gridded monthly time series v 3.01, 2012. URL `http://www.esrl.noaa.gov/psd/`.

J. R. Minder, D. R. Durran, G. H. Roe, and A. M. Anders. The climatology of small-scale orographic precipitation over the Olympic Mountains: Patterns and processes. *Quarterly Journal of the Royal Meteorological Society*, 134(633):817–839, 2008.

I. N. Mohammed and D. G. Tarboton. On the interaction between bathymetry and climate in the system dynamics and preferred levels of the Great Salt Lake. *Water Resources Research*, 47(2), 2011.

I. N. Mohammed and D. G. Tarboton. An examination of the sensitivity of the Great Salt Lake to changes in inputs. *Water Resources Research*, 48(11), 2012.

T. Mölg and D. R. Hardy. Ablation and associated energy balance of a horizontal glacier surface on Kilimanjaro. *Journal of Geophysical Research: Atmospheres (1984–2012)*, 109(D16), 2004.

Y. Moon, U. Lall, H.-H. Kwon, et al. Non-parametric short-term forecasts of the Great Salt Lake using atmospheric indices. *International Journal of Climatology*, 28(3):361–370, 2008.

F. I. Morton. Practical estimates of lake evaporation. *Journal of Climate and Applied Meteorology*, 25(3):371–387, 1986.

J. Mouginot, E. Rignot, and B. Scheuchl. Sustained increase in ice discharge from the Amundsen Sea Embayment, West Antarctica, from 1973 to 2013. *Geophysical Research Letters*, 41(5):1576–1584, 2014.

A. Nesje. Briksdalsbreen in western Norway: AD 1900-2004 frontal fluctuations as a combined effect of variations in winter precipitation and summer temperature. *The Holocene*, 15(8):1245–1252, 2005.

S. Nowicki, R. A. Bindschadler, A. Abe-Ouchi, A. Aschwanden, E. Bueler, H. Choi, J. Fastook, G. Granzow, R. Greve, G. Gutowski, et al. Insights into spatial sensitivities of ice mass response to environmental change from the SeaRISE ice sheet

modeling project II: Greenland. *Journal of Geophysical Research: Earth Surface*, 118(2):1025–1044, 2013.

J. Nye. The response of glaciers and ice-sheets to seasonal and climatic changes. *Proceedings of the Royal Society of London. Series A. Mathematical and Physical Sciences*, 256(1287):559–584, 1960.

J. Nye. The influence of climatic variations on glaciers. *International Association of Scientific Hydrology, General Assembly Helsinki*, pages 397–404, 1961.

J. Nye. The response of a glacier to changes in the rate of nourishment and wastage. *Proceedings of the Royal Society of London. Series A. Mathematical and Physical Sciences*, 275(1360):87–112, 1963.

J. Oerlemans. Holocene glacier fluctuations: is the current rate of retreat exceptional? *Annals of Glaciology*, 31(1):39–44, 2000.

J. Oerlemans. *Glaciers and climate change*. CRC Press, 2001.

J. Oerlemans. Extracting a climate signal from 169 glacier records. *Science*, 308 (5722):675–677, 2005.

J. Oerlemans. Linear modelling of glacier length fluctuations. *Geografiska Annaler: Series A, Physical Geography*, 94(2):183–194, 2012.

J. Oerlemans, B. Anderson, A. Hubbard, P. Huybrechts, T. Johannesson, W. Knap, M. Schmeits, A. Stroeven, R. Van de Wal, J. Wallinga, et al. Modelling the response of glaciers to climate warming. *Climate dynamics*, 14(4):267–274, 1998.

A. Ohmura, P. Kasser, and M. Funk. Climate at the equilibrium line of glaciers. *Journal of Glaciology*, 38(130):397–411, 1992.

M. A. ONeal. *Late Little Ice Age glacier fluctuations in the Cascade Range of Washington and northern Oregon*. PhD thesis, University of Washington, 2005.

S. Patankar. *Numerical Heat Transfer and Fluid Flow*. Series in computational methods in mechanics and thermal sciences. Taylor & Francis, 1980. ISBN 9780891165224.

W. Paterson. *The physics of glaciers*. Butterworth-Heinemann, 1994.

F. Pattyn, C. Schoof, L. Perichon, R. Hindmarsh, E. Bueler, B. d. Fleurian, G. Durand, O. Gagliardini, R. Gladstone, D. Goldberg, et al. Results of the marine ice sheet model intercomparison project, MISMIP. *The Cryosphere Discussions*, 6(1): 267–308, 2012.

A. J. Payne, A. Vieli, A. P. Shepherd, D. J. Wingham, and E. Rignot. Recent dramatic thinning of largest West Antarctic ice stream triggered by oceans. *Geophysical Research Letters*, 31(23), 2004.

M. S. Pelto and C. Hedlund. Terminus behavior and response time of North Cascade glaciers, Washington, USA. *Journal of Glaciology*, 47(158):497–506, 2001.

M. S. Pelto and J. Riedel. Spatial and temporal variations in annual balance of North Cascade glaciers, Washington 1984–2000. *Hydrological Processes*, 15(18):3461–3472, 2001.

W. T. Pfeffer, J. Harper, and S. O'Neel. Kinematic constraints on glacier contributions to 21st-century sea-level rise. *Science*, 321(5894):1340–1343, 2008.

D. Pollard and R. M. DeConto. Modelling West Antarctic ice sheet growth and collapse through the past five million years. *Nature*, 458(7236):329–332, 2009.

S. C. Porter. Present and past glaciation threshold in the Cascade Range, Washington, USA: topographic and climatic controls and paleoclimatic implications. *Journal of Glaciology*, 18:101–116, 1977.

A. Post. *Inventory of glaciers in the North Cascades, Washington*. US Government Printing Office, 1971.

H. Pritchard, S. Ligtenberg, H. Fricker, D. Vaughan, M. Van den Broeke, and L. Padman. Antarctic ice-sheet loss driven by basal melting of ice shelves. *Nature*, 484 (7395):502–505, 2012.

J. Putkonen and M. O'Neal. Degradation of unconsolidated Quaternary landforms in the western North America. *Geomorphology*, 75(3):408–419, 2006.

C. Raymond. Shear margins in glaciers and ice sheets. *Journal of Glaciology*, 42(140): 90–102, 1996.

B. Reichert, L. Bengtsson, and J. Oerlemans. Recent glacier retreat exceeds internal variability. *Journal of Climate*, 15(21), 2002.

J. A. Renwick and J. M. Wallace. Relationships between North Pacific wintertime blocking, El Niño, and the PNA pattern. *Monthly Weather Review*, 124(9):2071–2076, 1996.

P. J. Richerson, C. Widmer, T. Kittel, et al. Limnology of Lake Titicaca (Peru-Bolivia), a large, high altitude tropical lake. In *Institute of Ecology Publication*, volume 14. Institute of Ecology, 1977.

E. Rignot, J. L. Bamber, M. R. Van Den Broeke, C. Davis, Y. Li, W. J. Van De Berg, and E. Van Meijgaard. Recent Antarctic ice mass loss from radar interferometry and regional climate modelling. *Nature Geoscience*, 1(2):106–110, 2008.

E. Rignot, J. Mouginot, and B. Scheuchl. Ice flow of the Antarctic ice sheet. *Science*, 333(6048):1427–1430, 2011.

G. Roe. Feedbacks, timescales, and seeing red. *Annual Review of Earth and Planetary Sciences*, 37:93–115, 2009.

G. H. Roe. What do glaciers tell us about climate variability and climate change? *Journal of Glaciology*, 57(203):567–578, 2011.

G. H. Roe and M. B. Baker. Glacier response to climate perturbations: an accurate linear geometric model. *in press*, 2014.

G. H. Roe and M. A. O'Neal. The response of glaciers to intrinsic climate variability: observations and models of late-Holocene variations in the Pacific Northwest. *Journal of Glaciology*, 55(193):839–854, 2009.

V. Romanovsky, T. Sazonova, V. Balobaev, N. Shender, and D. Sergueev. Past and recent changes in air and permafrost temperatures in eastern Siberia. *Global and Planetary Change*, 56(3):399–413, 2007.

N. Ross, R. G. Bingham, H. F. Corr, F. Ferraccioli, T. A. Jordan, A. Le Brocq, D. M. Rippin, D. Young, D. D. Blankenship, and M. J. Siegert. Steep reverse bed slope at the grounding line of the Weddell Sea sector in West Antarctica. *Nature Geoscience*, 5(6):393–396, 2012.

S. Rupper and G. Roe. Glacier changes and regional climate: A mass and energy balance approach. *Journal of Climate*, 21(20), 2008.

S. B. Rupper. *Glacier sensitivity and regional climate: Past and present*. PhD thesis, University of Washington, 2007.

T. B. Sangoyomi, U. Lall, and H. D. Abarbanel. Nonlinear dynamics of the Great Salt Lake: dimension estimation. *Water Resources Research*, 32(1):149–159, 1996.

J. J. Sapiano, W. t. Harrison, and K. Echelmeyer. Elevation, volume and terminus changes of nine glaciers in North America. *Journal of Glaciology*, 44(146):119–135, 1998.

C. Schoof. Ice sheet grounding line dynamics: Steady states, stability, and hysteresis. *Journal of Geophysical Research: Earth Surface (2003–2012)*, 112(F3), 2007.

A. Shepherd, E. R. Ivins, A. Geruo, V. R. Barletta, M. J. Bentley, S. Bettadpur, K. H. Briggs, D. H. Bromwich, R. Forsberg, N. Galin, et al. A reconciled estimate of ice-sheet mass balance. *Science*, 338(6111):1183–1189, 2012.

R. Sidjak. Glacier mapping of the Illecillewaet icefield, British Columbia, Canada, using Landsat TM and digital elevation data. *International Journal of Remote Sensing*, 20(2):273–284, 1999.

S. Solomon, I. P. on Climate Change, and I. P. on Climate Change. Working Group I. *Climate Change 2007 - The Physical Science Basis: Working Group I Contribution to the Fourth Assessment Report of the IPCC*. Assessment report (Intergovernmental Panel on Climate Change).: Working Group. Cambridge University Press, 2007. ISBN 9780521705967. URL `http://books.google.com/books?id=8-m8nXB8GB4C`.

T. Stolldorf, H.-W. Schenke, and J. B. Anderson. LGM ice sheet extent in the Weddell Sea: evidence for diachronous behavior of Antarctic ice sheets. *Quaternary Science Reviews*, 48:20–31, 2012.

F. Street-Perrott and S. P. Harrison. Lake levels and climate reconstruction. *Paleoclimate Analysis and Modeling*, pages 291–340, 1985.

W. V. Tangborn, A. G. Fountain, and W. G. Sikonia. Effect of area distribution with altitude on glacier mass balance–a comparison on North and South Klawatti glaciers, Washington State, USA. *Annals of Glaciology*, 14:278–282, 1990.

P. A. Thomas, D. J. Easterbrook, and P. U. Clark. Early Holocene glaciation on Mount Baker, Washington State, USA. *Quaternary Science Reviews*, 19(11):1043–1046, 2000.

B. F. Turner, L. Gardner, and W. Sharp. The hydrology of Lake Bosumtwi, a climate-sensitive lake in Ghana, West Africa. *Journal of Hydrology*, 183(3):243–261, 1996.

USGS Water Resources. Great Salt Lake at State Park Saltair Beach Boat Harbor, Utah, November 2013. URL `http://waterdata.usgs.gov/ut/nwis/uv?`

H. Von Storch and F. W. Zwiers. *Statistical analysis in climate research*. Cambridge University Press, 2001.

K. M. Waddell and J. Barton. *Estimated inflow and evaporation for Great Salt Lake, Utah, 1931-76, with revised model for evaluating the effects of dikes on the water and salt balance of the lake*. Division of Water Resources, Utah Department of Natural Resources, 1980.

J. Wallace, E. Rasmusson, T. Mitchell, V. Kousky, E. Sarachik, and H. v. Storch. On the structure and evolution of ENSO-related climate variability in the tropical Pacific: Lessons from TOGA. *Journal of Geophysical Research: Oceans (1978–2012)*, 103(C7):14241–14259, 1998.

J. M. Wallace and D. S. Gutzler. Teleconnections in the geopotential height field during the Northern Hemisphere winter. *Monthly Weather Review*, 109(4):784–812, 1981.

S.-Y. Wang, R. R. Gillies, J. Jin, and L. E. Hipps. Coherence between the Great Salt Lake level and the Pacific Quasi-Decadal Oscillation. *Journal of Climate*, 23(8): 2161–2177, 2010.

S. Weber and J. Oerlemans. Holocene glacier variability: three case studies using an intermediate-complexity climate model. *The Holocene*, 13(3):353–363, 2003.

J. Weertman. Stability of the junction of an ice sheet and an ice shelf. *Journal of Glaciology*, 13:3–11, 1974.

Western Regional Climate Center. Evaporation stations. URL http://www.wrcc.dri.edu/htmlfiles/westevap.final.html. Time series accessed throgh personal communication, 01-10-14.

P. L. Whitehouse, M. J. Bentley, and A. M. Le Brocq. A deglacial model for Antarctica: geological constraints and glaciological modelling as a basis for a new model of Antarctic glacial isostatic adjustment. *Quaternary Science Reviews*, 32:1–24, 2012.

C. Willmott, K. Matsuura, and D. Legates. Terrestrial air temperature: 1900-2010 gridded monthly time series v 3.01, 2012. URL http://www.esrl.noaa.gov/psd/.

Y. Zhang, J. M. Wallace, and D. S. Battisti. ENSO-like interdecadal variability: 1900-93. *Journal of Climate*, 10(5):1004–1020, 1997.

Appendix A

INTERPRETING TEMPORAL VARIABILITY

This appendix describes how climate forcing expressed in proxy records. It will contextualize why the proxy-climate relationship is difficult to interpret.

The relationship between a proxy record and the climate history is complicated by the dynamical response of the proxy itself. If the proxy has inertia, it is influenced not only by the climate at a given time but also by its memory of previous climate states. The characteristic memory of the system implies that a proxy records some information about the climate *before* deposition as well as the climate *at the time* of deposition. If the memory of the system is long, the previous climate will strongly affect the proxy signal.

The simplest general representation of a dynamical system with memory is a linear first-order differential equation of the form:

$$\frac{dy}{dt} + \frac{y}{\tau} = f(t), \tag{A.1}$$

where y is the proxy variable, τ is the characteristic timescale (or memory), and $f(t)$ is the climatic forcing. Eq. (A.1) can also represent the linearization of a more complicated nonlinear dynamical system, if the proxy fluctuations are small. Beyond the domain of strict linearity, Eq. (A.1) provides important insights into a proxy's response to climate.

There are two complementary and entirely equivalent interpretations of the solution of Eq. (A.1) :

- the proxy record *integrates* the time series of the climate forcing *or*
- the proxy record *filters* the power spectrum of the climate forcing.

Each interpretation of the solution to Eq. (A.1) is described below.

Geophysical systems integrate the climate time series

If τ is constant and the forcing is not dependant on the state of the system[1] the general solution to Eq. (A.1) is:

$$y(t) = y_0 e^{-t/\tau} + \int_0^t e^{(t'-t)/\tau} f(t') dt', \tag{A.2}$$

where y_0 is $y(t = 0)$ and t' is a dummy variable. The response variable, $y(t)$, is a function of the integral of the forcing function, $f(t)$ along a time line from 0 to t. As time progresses, the most recent forcings are weighted exponentially more. If τ is large compared to t, $e^{(t'-t)/\tau}$ is relatively large, and the system remembers past forcings for a longer time. Conversely, if τ is small, $e^{(t'-t)/\tau}$ is a smaller value, and the past forcings have a lesser effect on the present time step.

Geophysical systems filter the climate spectrum

Eq. (A.1) can be written in terms of the Fourier transforms of $y(t)$ and $f(t)$:

- $y(t) \Longrightarrow \int_{-\infty}^{\infty} \tilde{Y}(\omega) e^{-i\omega t} d\omega$ and
- $f(t) \Longrightarrow \int_{-\infty}^{\infty} \tilde{F}(\omega) e^{-i\omega t} d\omega$

[1] though the equation can be solved numerically, even if τ or $f(t)$ are dependant on $y(t)$

Substituting these into Eq. (A.1), yields the following equation:

$$\int_{-\infty}^{\infty}(-i\omega+\frac{1}{\tau})\tilde{Y}(\omega)e^{-i\omega t}d\omega=\int_{-\infty}^{\infty}\tilde{F}(\omega)e^{-i\omega t}d\omega, \tag{A.3}$$

The integrands on both sides of Eq. (A.3) must be equal. Therefore,

$$\tilde{Y}(\omega)=\frac{1}{-i\omega+{}^{1}\!/_{\tau}}\tilde{F}(\omega). \tag{A.4}$$

The $(-i\omega+\frac{1}{\tau})$ term is referred to as the transfer function, and maps the forcing function, $\tilde{F}(\omega)$, to the response function, $\tilde{Y}(\omega)$. For $\omega\tau >> 1$ the response is in quadrature with the forcing and is damped in proportion to the frequency of the forcing. Higher frequencies will be under-represented in the response function. For $\omega\tau << 1$, the response is in near equilibrium with the forcing, and for a given size of $F(\omega)$ a larger τ implies a larger response. The larger τ is, the weaker the restoring tendency (i.e. the second term on the left-hand side of Eq. (A.1)), and so the larger the equilibrium response. All frequencies will be well represented by the response function.

The spectral power is given by multiplying both sides of Eq. (A.3) by their complex conjugates, and taking the resulting square of the real component of the Fourier transformation:

$$\tilde{Y}(\omega)\tilde{Y}^{*}(\omega)=(-i\omega+\frac{1}{\tau})(i\omega+\frac{1}{\tau})\tilde{F}(\omega)\tilde{F}^{*}(\omega), \tag{A.5}$$

where a * denotes the complex conjugate. The factor in parentheses on the right-hand side of Eq. (A.5) is a spectral filter that is independent of frequency for $\omega\tau << 1$, but falls off as ${}^{1}\!/_{\omega^{2}}$ for $\omega\tau >> 1$.

Appendix B

AUTOCORRELATION: DETERMINING THE DEGREES OF FREEDOM

The autocorrelation of a glacier significantly constrains the number of degrees of freedom (d.o.f) available to qualify the significance of an observed r_L. The greater the time scale, the more a glacier is influenced by its previous states, so fewer statistically independent observations are obtainable in a given interval of time. This glacier memory increases the likelihood that, simply by chance, high correlations will be observed between glaciers. To determine the proper confidence intervals, the correct number of d.o.f. for a given length of time must be calculated. To do so we must also derive an equation for ρ_L.

The autocorrelation of the length is described by finding the covariance between the lengths from one time step to the next:

$$\langle L_{t+1}L_T\rangle = \gamma^2\langle L_tL_{t-1}\rangle+\alpha^2\langle T_tT_{t-1}\rangle+\beta^2\langle P_TP_{t-1}\rangle+\gamma\alpha\langle L_tT_{t-1}+\langle L_{t-1}T_t\rangle+\gamma\beta\langle L_TP_{t-1}+L_{t-1}P_t\rangle \tag{B.1}$$

Multiplying eq. (2.1) by T_{t-1} and again neglecting the cross terms between T and P,

$$\langle L_tT_{t-1}\rangle = \gamma\langle L_{t-1}T_{t-1}\rangle + \alpha\langle T_{t-1}^2\rangle. \tag{B.2}$$

Utilizing eq. (2.8) yet again, to replace $\langle L_{t-1}T_{t-1}\rangle$, the length at any given time is related to T at that point at the previous time step:

$$\langle L_t T_{t-1}\rangle = \frac{\gamma\alpha\rho_T\sigma_T^2}{1-\gamma\rho_T} + \alpha\sigma_T^2 \tag{B.3}$$

Because T at time t can be related to temperature at time $t-1$ via its autocorrelation ρ_T^2 at that point, plus a random component, we write

$$\langle L_{t-1}T_t\rangle = \frac{\alpha\rho_T^2\sigma_T^2}{1-\gamma\rho_T} \tag{B.4}$$

Using this same derivation for $\langle L_t P_{t-1} + L_{t-1}P_T\rangle$, we enter eqs. (B.3) and (B.4) into eq. (B.2). Our equation describing the autocorrelation of the length of the glacier is written as

$$\rho_L = \frac{1}{\sigma_L^2(1-\gamma^2)}\left[\alpha^2\rho_T\sigma_T^2\left(1+\frac{\gamma^2}{1-\gamma\rho_T}\frac{\gamma}{\rho_T}\frac{\gamma\rho_T}{1-\gamma\rho_T}\right)+\beta^2\rho_P\sigma_P^2\left(1+\frac{\gamma^2}{1-\gamma\rho_P}\frac{\gamma}{\rho_P}\frac{\gamma\rho_P}{1-\gamma\rho_P}\right)\right]. \tag{B.5}$$

If the autocorrelations in the climate $\rho_{T,P}$ are zero, (A5) will simplify dramatically.

This autocorrelation allows us to determine the input into the Bretherton et al. [1999] formula for determining the correct number of d.o.f. in a time series, given some level of autocorrelation. The autocorrelation of the glacial system requires a much longer record in order to determine a significant correlation than its forcings,

which have a much shorter memory.

Therefore, we increase the numbers of d.o.f. by assuming that the 1950 - 1990 detrended values for temperature and precipitation are representative of the range of variation over longer periods of time. This is a reasonable assumption as the brevity of the detrended T and P data yields a conservative estimate of the climate variations.

Appendix C

STANDARD DEVIATIONS IN LAKE LEVEL

Discretizing eq. (4.8) in to time increments, Δt, and setting $P' = 0$, gives

$$h'_t = h'_{t-\Delta t}\left(1 - \frac{\Delta t}{\tau}\right) E'_t. \tag{C.1}$$

We set $E'_t = \sigma_E \nu_t$, where ν_t is a normally distributed, stochastic white noise process. The variance of h'_t is the expected value of h'^2_t , and is given by

$$\langle h'^2_t \rangle = \left(1 - \frac{\Delta t}{\tau}\right)^2 \langle h'^2_{t-1} \rangle + 2\left(1 - \frac{\Delta t}{\tau}\right) \sigma_E \Delta t \langle h'_{t-1} \nu_t \rangle + \sigma_E^2 \Delta t^2 \langle \nu_t^2 \rangle. \tag{C.2}$$

The following relationships hold: $\langle \nu_t h'_t \rangle = 0$, $\langle h'^2_t \rangle = \langle h'^2_{t-1} \rangle$, and $\langle \nu_t^2 \rangle = 1$. Upon substitution, and taking the limit of $\Delta t << \tau$ we obtain:

$$\langle h'^2_t \rangle = \frac{\sigma_E^2 \Delta t^2}{2\Delta t/\tau}, \tag{C.3}$$

Therefore,

$$\sigma_{hE} = \sigma_E \left(\frac{\Delta t \tau}{2}\right). \tag{C.4}$$

Similarly for lake-level variability due to $P'(t)$ alone:

$$\sigma_{hP} = \left[1 - \gamma + \frac{\gamma A_B}{\bar{A}_L}\right] \sigma_P \left(\frac{\Delta t \tau}{2}\right). \tag{C.5}$$

Provided that P' and E' are not correlated the variances can be combined as:

$$\sigma_h = \sqrt{\sigma_{hE}^2 + \sigma_{hP}^2} \tag{C.6}$$

Appendix D

ICE STREAM MODEL METHODS

We construct a 1.5-dimension, finite-differences numerical flowline model using standard shallow-ice equations [Oerlemans, 2001], accounting for deformation and sliding within a width-varying ice stream. The continuity equation, which ensures that ice volume is conserved, can be written as a diffusion equation:

$$\frac{\partial H}{\partial t} = \frac{-1}{w}\frac{\partial}{\partial x}\left(\Gamma\frac{\partial h}{\partial x}\right) + \dot{b}(x,t), \tag{D.1}$$

where $H(x,t)$ is the ice thickness, w is the width of the catchment at each distance down the flowline, h is the surface elevation ($H + z_b$) and $\dot{b}(x,t)$is the accumulation rate profile along the flowline. The diffusivity parameter, Γ is defined by:

$$\Gamma(x) = w\left[-\frac{2\bar{A}}{n+2}\left(\frac{dh}{dx}\right)^2 H^5(\rho g)^3 - C^{-1/m}(\rho g)^{1/m}\left(\frac{dh}{dx}\right)^{(1-m)/m} H^{(1+m)/m}\right], \tag{D.2}$$

The shallow-ice equations are appropriate to represent deformation of ice in the interior, which is the purpose here. At the divide ($x = 0$), the flux is zero. Equilibrium is attained when the ice-flux equals $q(x_g)$ (i.e., Eq. 5.1), at a point that also satisfies the grounding line condition (Eq. 5.2). For variable z_b there may be multiple equilibria [Schoof, 2007]. The profile of the floating ice shelf is not modeled. Our work expands upon that of Docquier et al. [2011], Schoof [2007], Pattyn et al. [2012] by replacing an idealized basal geometry with a realistic bed topography.

This shallow-ice flowline model cannot represent the ices complete stress and strain fields, and, as such, it is not as comprehensive as three-dimensional ice-flow models. However, the spatial heterogeneity of physical factors such as softness and basal sliding, as well as an incomplete understanding of ice dynamics and ice-ocean interactions make it difficult to gauge the predictive power of more comprehensive models. Numerical modeling of a single flowline within an ice stream is more computationally tractable and has been effectively used in previous research to build understanding of the relative importance of the various factors that control marine-based ice sheet stability.

The flowline model integrates the observed present-day accumulation [Le Brocq et al., 2010] over an ice streams catchment area, determined from the surface topography [Joughin and Bamber, 2005]. One characteristic flowline from the RADARSAT-1 Antarctic Mapping Project data set [Byrd Polar Research Center] is chosen for each ice-stream catchment area. The flowlines are linearly interpolated at 1km resolution onto the Bedmap2 [Fretwell et al., 2013] basal and surface topography. Model results are presented at this resolution, though results were qualitatively unchanged for coarser grids (up to 20km was checked). The model responses are also similar for alternative FIS flowline paths. The grounding line positions are modified from the Bedmap2 estimate to incorporate Rignot et al. [2011] estimations alone. Description of data errors can be found in the original papers.

VITA

Kat Huybers was raised outside of Los Angeles, in Moorpark, California. She majored in Mathematics and minored in Philosophy at the University of San Francisco, where she received her Bachelors of Science in 2003. From 2003 to 2004, Kat worked in Massachusetts as a junior-high algebra teacher, a vegetable farmer, and a barista. She began her graduate studies in Earth and Space Sciences at the University of Washington in 2004, and received a Masters degree in Geophysics in 2007. In March - April of 2006, she assisted UW researchers on a project at Summit Station, Greenland, and fell in love with polar field work. From 2007 through 2009, Kat worked as a seasonal science technician at Summit Station. She returned to graduate school in January of 2010, and had the good fortune to work two Antarctic field seasons. She received her PhD in June of 2014. Kat lives in Seattle's Central District, and is grateful for the her commute through Interlaken Park, the Sunday crossword puzzle, the Seattle Inner City Outings program, and her Tuesday night dinner club.